Collot, J.-Y., Greene, H. G., Stokking, L. B., et al., 1992
Proceedings of the Ocean Drilling Program, Initial Reports, Vol. 134

7. SITE 827[1]

Shipboard Scientific Party[2]

HOLE 827A

Date occupied: 20 October 1990

Date departed: 22 October 1990

Time on hole: 1 day, 8 hr, 15 min

Position: 15°17.741′S, 166°21.116′E

Bottom felt (rig floor; m; drill-pipe measurement): 2814.2

Distance between rig floor and sea level (m): 10.80

Water depth (drill-pipe measurement from sea level, m): 2803.4

Total depth (rig floor; m): 2924.80

Penetration (m): 110.60

Number of cores (including cores with no recovery): 15

Total length of cored section (m): 110.60

Total core recovered (m): 100.76

Core recovery (%): 91

Oldest sediment cored:
Depth below seafloor (m): 110.60
Nature: volcanic silt
Age: Pleistocene
Measured velocity (km/s): 1.942

HOLE 827B

Date occupied: 22 October 1990

Date departed: 25 October 1990

Time on hole: 3 days, 6 hr

Position: 15°17.746′S, 166°21.112′E

Bottom felt (rig floor; m; drill-pipe measurement): 2814.2

Distance between rig floor and sea level (m): 10.80

Water depth (drill-pipe measurement from sea level, m): 2803.4

Total depth (rig floor; m): 3214.60

Penetration (m): 400.40

Number of cores (including cores with no recovery): 31

Total length of cored section (m): 289.80

Total core recovered (m): 119.04

Core recovery (%): 41

Oldest sediment cored:
Depth below seafloor (m): 400.40
Nature: partially lithified, matrix-supported sed-lithic conglomerate.
Age: unknown. Sample barren (nannofossil ooze with foraminifers and ash located at 252 m dated as late Pliocene).
Measured velocity (km/s): 1.990

Principal results: Site 827 (proposed Site DEZ-2) is located within the collision zone of the d'Entrecasteaux Zone (DEZ), along the forearc slope of the New Hebrides Island Arc, 35 km west of the western shore of Espiritu Santo Island. A short geophysical survey was undertaken to locate a flat, sedimented area suitable for spudding; the site was finally selected within a fairly small, flat yet hummocky surfaced plateau 4 km east of the trace of the subduction zone, an area that appears to have dammed and ponded sediment being transported downslope from the island. Here the North d'Entrecasteaux Ridge (NDR) is impinging upon the arc slope and has formed a tectonic front of lobate morphology that is composed of sheared and fractured accreted (?) and arc-derived material. This collision has produced an unstable slope prone to mass wasting and shearing from arcward-dipping thrust faults. Site 827 is located upon a thrust sheet or slump block that has been severely deformed by the active convergent tectonic processes. The site was chosen to penetrate the lower forearc slope where rocks of the overriding plate are thin in anticipation of drilling through the décollement and rock units of the underlying NDR. Our intent was to define the lithology, composition, age, and mechanical properties of rocks drilled to determine the degree and rate of material transfer from one plate to another, the timing of collision, the present-day stress field, and the composition and role of fluid circulation in the collision process.

We cored 110.6 m and recovered 100.76 m of sediment in Hole 827A for a 91% core recovery, and cored 400.4 m to recover 119.04 m of sediment and rock in Hole 827B for a 41% core recovery. Four lithostratigraphic units have been described: Unit I (0–86 mbsf) consists of Pleistocene volcanic silt interbedded with normally graded, sandy volcanic silt beds (turbidites). This unit is subdivided into three subunits based on the concentrations of turbidite layers. Subunit IA (0–40 mbsf) is a volcanic siltstone with a few distinct turbidite layers whereas Subunit IB (40–66 mbsf) is a volcanic siltstone with many turbidite layers and Subunit IC (66–86 mbsf) is a volcanic siltstone with less concentrated turbidite layers than found in Subunit IB. Unit II (86–141 mbsf) is a sequence of upper Pliocene to Pleistocene (?) volcanic silt and siltstones with varying components of clay and sand. Unit III (141–252.6 mbsf) contains upper Pliocene to middle Pleistocene (?) highly bioturbated, partially lithified calcareous volcanic siltstone with intervals of sed-lithic conglomerate. Unit III can be divided into three subunits consisting of an upper 59 m of tectonically disturbed, highly bioturbated, sandy to clayey volcanic siltstone (Subunit IIIA, 141–200 mbsf), an intermediate 18 m of sed-lithic conglomerate/breccia (Subunit IIIB, 200–218 mbsf), and a lower 34 m of volcanic siltstone and foraminiferal and nannofossil ooze interbedded with ash and a highly sheared, variegated lustrous zone that appears rich in chlorite or some other micaceous mineral (Subunit IIIC, 218–252.6 mbsf). Unit IV (252.6–400.4 mbsf) comprises only clasts ranging in size from pebbles to the maximum diameter that can fit into the core barrel. These clasts consist of very well-lithified volcanic siltstone and sandstone, lithified breccias, or coarse sandstone containing a preponderance of igneous rock fragments and crystals. These clasts are mixed into a highly sheared and fractured matrix; the rock as a whole is called a partially lithified, matrix-supported sed-lithic conglomerate.

Initial interpretations of the core suggest that Unit I, which consists almost entirely of graded beds of volcanic silt and sandy silt containing both Pleistocene microfossils and reworked Mi-

[1] Collot, J.-Y., Greene, H. G., Stokking, L. B., et al., 1992. *Proc. ODP, Init. Repts.*, 134: College Station, TX (Ocean Drilling Program).

[2] Shipboard Scientific Party is as given in the list of participants preceding the contents.

ocene microfossils, was most likely derived from Espiritu Santo Island and transported to the site by turbidity currents. This unit contains plant debris fragments and coincides with a stratigraphic interval where benthic foraminifers suggest low oxygen conditions, as would be expected in an environment where rapid burial by turbidity currents suppresses burrowing organisms that would otherwise consume and oxidize the organic matter. Unit II is similar in lithology, but of late Pliocene to Pleistocene (?) age and devoid of graded bedding, and is interpreted as a hemipelagic deposit. The coarse-grained and debris-like sediments of Unit III probably were deposited in a high-energy, deep-water (middle bathyal zone) environment close to a volcanic island source; this unit was then severely sheared and fractured by the collision of the NDR. Unit IV is difficult to interpret because of the poor recovery; however, the depositional environment for such material must be proximal to the source because the material is very poorly sorted and the clasts are angular to sub-rounded.

Foraminifers and nannofossils were the best source of age information. The sedimentary samples recovered were predominantly of Pleistocene to late Pliocene (?) in age, with reworked late Miocene fauna. Paleomagnetic results from Hole 827A indicate that the cored samples were well within the Brunhes; cores from Hole 827B were too disturbed for paleomagnetic analysis.

Analyses of fluids from whole-round samples of the core indicate that chlorinity and salinity increase with depth to values 10% to 15% higher than seawater concentrations at 250 mbsf. Both potassium and sodium decrease to 40% to 50% of seawater values at 250 mbsf. Calcium concentrations increase strongly with depth to 250 mbsf, but display a very slight minimum at about 75 mbsf. Overall concentrations of nutrients are low and silica concentrations are variable. Sulfate reduction is complete by 50 mbsf, but sulfate concentrations subsequently increase with depth to values equal to about 30% of seawater. Methane concentrations are near zero except for a strong, sharp maximum at about 75 mbsf. A significant finding is that the methane peak is probably not a result of organic matter diagenesis because (1) it appears too large relative to increases in the nutrients and (2) it is located below the maxima in nutrient concentrations. This peak suggests that there may be "exotic" fluids in that zone. This fluid appears to have lower chlorinity, lower salinity, higher sodium and potassium concentrations, and lower magnesium concentrations. The calcium concentrations in this zone are controlled more by the steep depth gradients and thus exhibit no maxima or minima. This level also marks the first appearance of sulfate below the sulfate reduction zones. Low chlorinity concentrations, high methane concentrations, and sulfate below the zone of complete sulfate reduction are attributes of fluids in the Barbados and Nankai décollement zones.

Physical properties correlate well with the lithostratigraphic units. In lithostratigraphic Unit I (0–86 mbsf) the water content and porosity of the sediments decrease rapidly from a water content of 55% a few meters below the seafloor to below 40% at 40 mbsf. Bulk densities and velocities also agree, showing lithostratigraphic Unit II (86–141 mbsf) to be a denser, less porous unit in which sonic velocities increase significantly to more than 1920 m/s, before dropping rapidly in Unit III (141–252.6 mbsf), as water content and porosity increase to 60% or more. Two zones of major tectonic deformation occur in Unit III between 180–200 mbsf and 230–250 mbsf. Porosity and water content show distinct increases in the thrust planes of these zones, indicating that faults may be serving as dewatering conduits for fluids. In the hard rock breccia of Unit IV (252.6–400.4 mbsf), index properties and sonic velocity data are scattered. Due to hole collapse, logging was not undertaken.

BACKGROUND AND OBJECTIVES

Site 827 is the first of a series of drill sites (827–831) within the collision front of the d'Entrecasteaux Zone (DEZ) and the central New Hebrides Island Arc. It lies 35 km west of the western shore of Espiritu Santo Island, at the toe of the arc slope where the North d'Entrecasteaux Ridge (NDR) impinges upon the arc (Fig. 1).

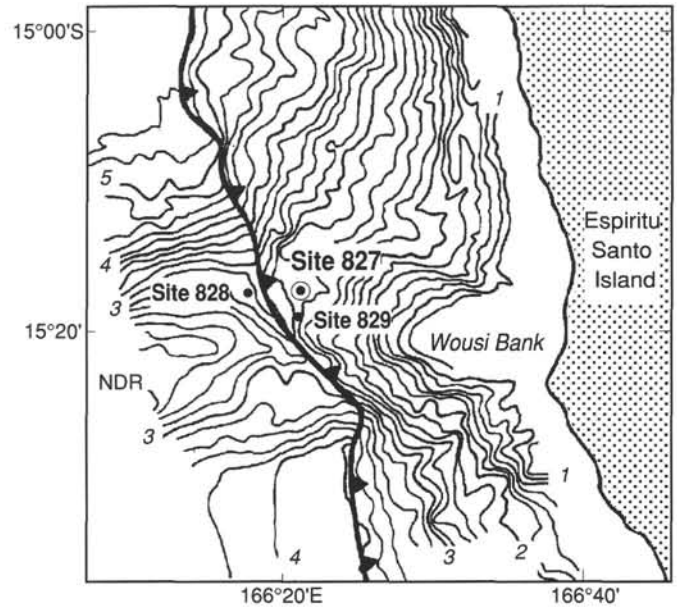

Figure 1. Location of Leg 134 drilling sites in the collision zone between the North d'Entrecasteaux Ridge (NDR) and the New Hebrides Island Arc (modified after Collot et al., 1989). Bathymetry in kilometers; contour interval is 200 m.

Near Sites 827 and 829, Seabeam bathymetry (Fig. 2) reveals a tectonic front that has a lobate morphology and shows a few sinuous trench-parallel lineaments that are interpreted as morphologic evidence for arcward-dipping thrust faults (Collot and Fisher, 1991). Above the tectonic front, the arc slope shows a terrace-like feature at a depth of 2850–2900 m below sea level (mbsl) that is bounded to the north by a steep north-facing scarp. The coincidence between these features and both a flat terrace and a break in slope of the NDR northern flank indicates that the NDR controls their formation. Site 827 is located on the terrace-like feature, 4 km east of the seafloor trace of the subduction zone, at a depth of 2,824 mbsl; this feature shows a hummocky surface morphology that is indicative of mass wasting.

Nautile dives conducted near this site (Collot et al., 1989) suggest that in this area the arc slope consists mainly of Pliocene to Holocene deep-water sediment with reworked Oligocene and middle and upper Miocene sediment. An Eocene age was assigned to reworked clasts (Collot et al., unpubl. data).[3] These sediments include tuffaceous limestone, calcareous and tuffaceous mud, mudstone and siltstone, feldspathic graywacke, and volcanic breccia. Most of these rocks were shown to be highly fractured and sheared.

Multichannel seismic reflection data indicate that low-frequency reflections from the top of the NDR can be traced from the tectonic front beneath the lower arc slope and therefore represent the interplate décollement (Fisher et al., 1986; Fisher et al., 1991). Above the décollement, strata are poorly reflective and dip slightly trenchward. Rocks above the

[3] Collot, J.-Y., Lallemand, S., Pelletier, B., Eissen, J.-P., Glaçon, G., Fisher, M. A., Greene, H. G., Boulin, J., Daniel, J., and Monzier, M. Geology of the d'Entrecasteaux–New Hebrides island arc collision: results from a deep-sea submersible survey (submitted to *Tectonophysics*).

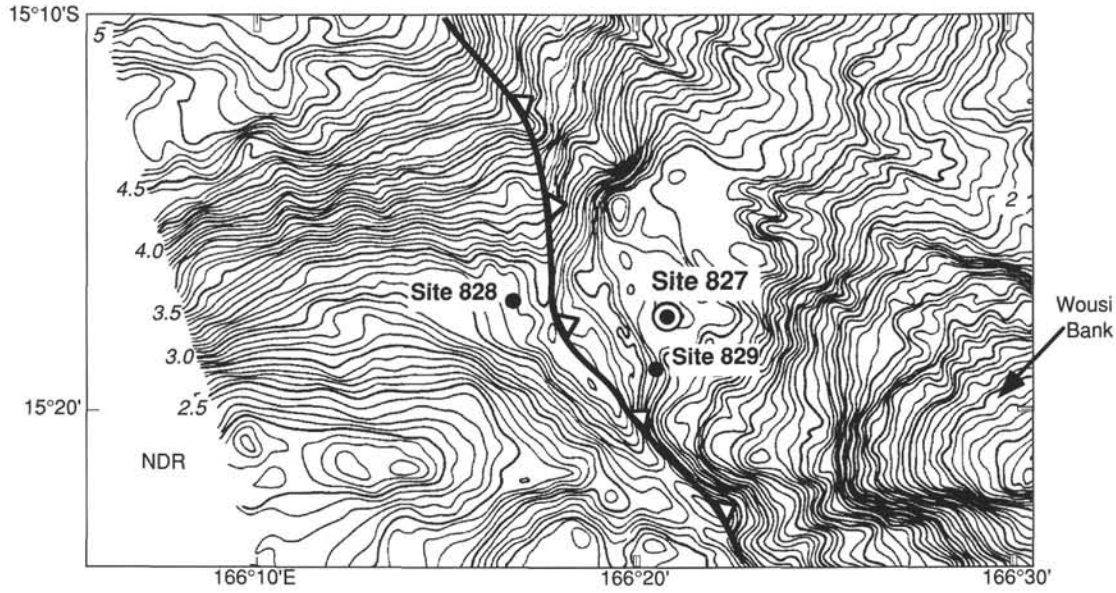

Figure 2. Detailed Seabeam bathymetry of the collision zone between the North d'Entrecasteaux Ridge (NDR) and the New Hebrides Island Arc (modified after Collot and Fisher, 1991). Bathymetry in kilometers, contour interval is 50 m.

décollement and close to the tectonic front can be subdivided into two layers based on seismic velocity measurements: a superficial layer with velocities between 2.0–2.1 km/s and a deeper layer with velocities between 3.3–3.4 km/s (Fisher et al., 1991). The high velocity layer was not expected and previously remained unexplained.

In anticipation of drilling through the décollement and rock units of the underlying plate and NDR, Site 827 was chosen to penetrate the lower forearc slope where rocks of the overriding plate are thin. In this area the NDR is being subducted and lies fairly close to the seafloor.

The specific objectives for drilling the lower part of the forearc slope were to study the following aspects of the NDR–New Hebrides Island Arc collision processes:

1. The lithology, composition, age, and mechanical properties of the rocks of both the forearc and the underlying ridge.
2. The possible accretion of material from the colliding ridge onto the overriding plate.
3. The present-day stress field, as well as the uplift and subsidence history of the forearc in the context of collision.
4. The timing of the collision.
5. The composition of fluids and the role of fluid circulation in the collision process.

The first and second objectives were investigated through lithologic, petrologic, geochemical, and physical properties studies of rocks and clasts recovered from this site. The influence of arc-ridge collision on the differing lithologies of a forearc is still poorly known. The nature and composition of the ridge was tentatively determined at Site 828. Rocks that form the forearc slope could be uplifted remnants of an accretionary wedge that predates collision, or could have been accreted from rocks that form the ridge crest. A further possibility is that the forearc slope consists of island-arc basement rocks overlain by volcaniclastic rocks eroded from the nearby islands. The *Nautile* dives revealed the calcareous and volcaniclastic nature of the rocks exposed at the seafloor in this collision zone. The attitude and the nature of these rocks suggest that they were derived from the arc. However, the composition of the deep part of the wedge is still unknown. To determine whether rocks were accreted from the ridge to the overriding lithosphere or underplated beneath the toe of the wedge, we compared the lithology, composition, and ages of rocks recovered at Sites 827 and 828.

Objectives 3 and 4 were addressed by detailed sedimentological observations of the cores, logging studies, and paleontological estimates of paleobathymetry. The type of sediment and style of deposition on the forearc slope is postulated to have changed with time as the arc-ridge collision zone migrated north along the trench and approached its present-day location at latitude 15°20′S. The style of sedimentation may also have been influenced by collisions between forearc slope and other oceanic features, such as a hypothetical eastern extension of the West Torres Plateau, or by sea level changes. We anticipate that (1) while the NDR-arc collision was occurring further south of its present-day location, the sediments of the forearc slope were deposited under deep-water conditions and marine sediment was deposited on Espiritu Santo Island; (2) when the first impact of the collision occurred at the present-day collision zone, both the forearc slope and Espiritu Santo Island started to deform and uplift, and the sedimentation on the forearc became more subject to slump and turbidite deposition; (3) when collision became more severe, Espiritu Santo Island reached sea level and emerged; sediments shed from the island toward the forearc slope became coarser. Phases of uplift and subsidence of the outer forearc and Espiritu Santo Island may have alternated in this collision zone because of the possible irregular morphology of the subducting ridge.

Our fifth objective, to determine the composition and role of the fluids in the collision and subduction of the NDR, has been addressed by drilling the lower arc slope of the collision zone. Circulation of fluids along the décollement and thrust planes, as well as seeps at accretionary wedges, have been clearly demonstrated along well-sedimented accretionary margins (Gieskes et al., 1990b; Ritger et al., 1987). However, circulation of fluids that escape from the subducting plate through wedges is not well documented in nonaccretionary convergent plate margins or along arc-ridge

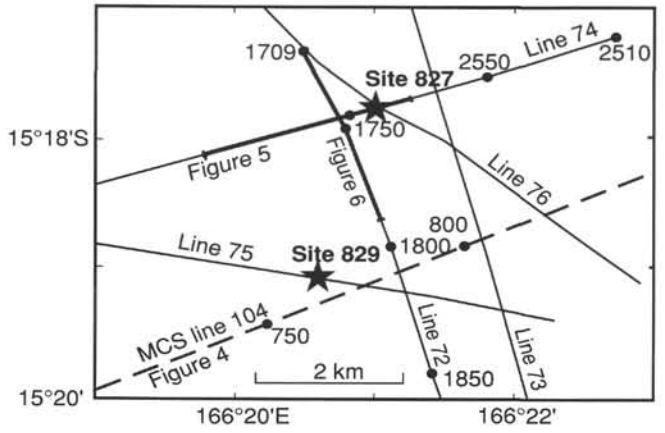

Figure 3. Trackline map showing the locations of Site 827, single-channel seismic lines 72 and 74, and multichannel seismic line 104 (USGS, *L5*-84-SP).

collision zones. We intend to document these processes and study how ridge collision affects the fluid circulation in the forearc and facilitates or prevents the hydration of island-arc crust.

SEISMIC STRATIGRAPHY

Multichannel Seismic Data

Multichannel seismic reflection data collected between 1982 and 1987 by the U.S. Geological Survey, ORSTOM, and IPGS (Institut de Physique du Globe de Strasbourg) show that, in general, rocks under the slope of the New Hebrides Island Arc return discontinuous, primarily seaward-dipping reflections. Exceptions to this rule include landward-dipping reflections that are apparently from thrust faults and locally strong subhorizontal reflections that presumably stem from the interplate décollement. The seaward dip of many reflections is unlike the arcward dip evident from other active margins and we propose that the reflections reveal mass-wasting deposits that resulted from the collision between the arc and the North d'Entrecasteaux Ridge.

Multichannel data from near Site 827 show that a reflection from the top of the colliding north ridge can be traced beneath the arc's lower slope (Figs. 3 and 4). The continuity of this reflection indicates that the ridge is being subducted without major ridge deformation. Under the arc slope this reflection may be from the subducted top of the ridge sediment or from the contact between this sediment and the underlying igneous basement. We interpret this reflection to be from the interplate décollement. Reflections from the lower slope rocks are incoherent, but most dip subparallel to the sea bottom. The events in Figure 4 that appear to downlap sigmoidally near the plate boundary onto the ridge top are artifacts of data processing that resulted from the poor handling of steep seafloor dips by migration programs. The poor acoustic image of rocks just east of the drill site suggests that considerable disruption of forearc strata has attended insertion of the north ridge. Conspicuously absent are large "bow-wave" structures that, in concept, form as slope rocks are displaced by the ridge's volume.

Single-Channel Seismic Data

Single-channel seismic reflection data were collected over Site 827, using two 80-in.^{3} water guns for the source and a streamer that has a 100-m-long active section. These data were processed aboard the ship using SIOSEIS software running on a Masscomp computer. The main processing steps included predictive deconvolution, bandpass filtering, and automatic gain control (AGC).

Seismic lines 72 and 74 (Figs. 3, 5, and 6) cross near Site 827. Line 72 shows a strong reflection at a traveltime of about

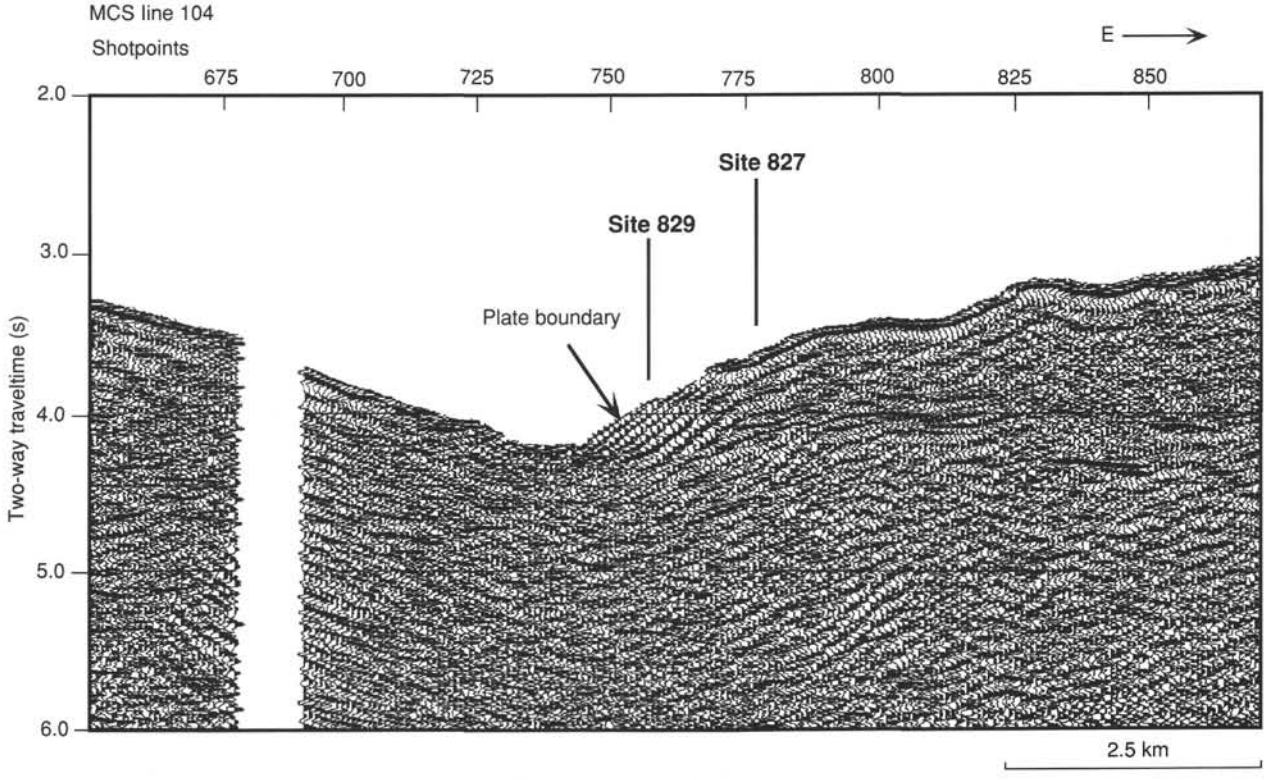

Figure 4. Part of multichannel seismic line 104 (USGS, L5-84-SP), which crosses the arc slope near Site 827.

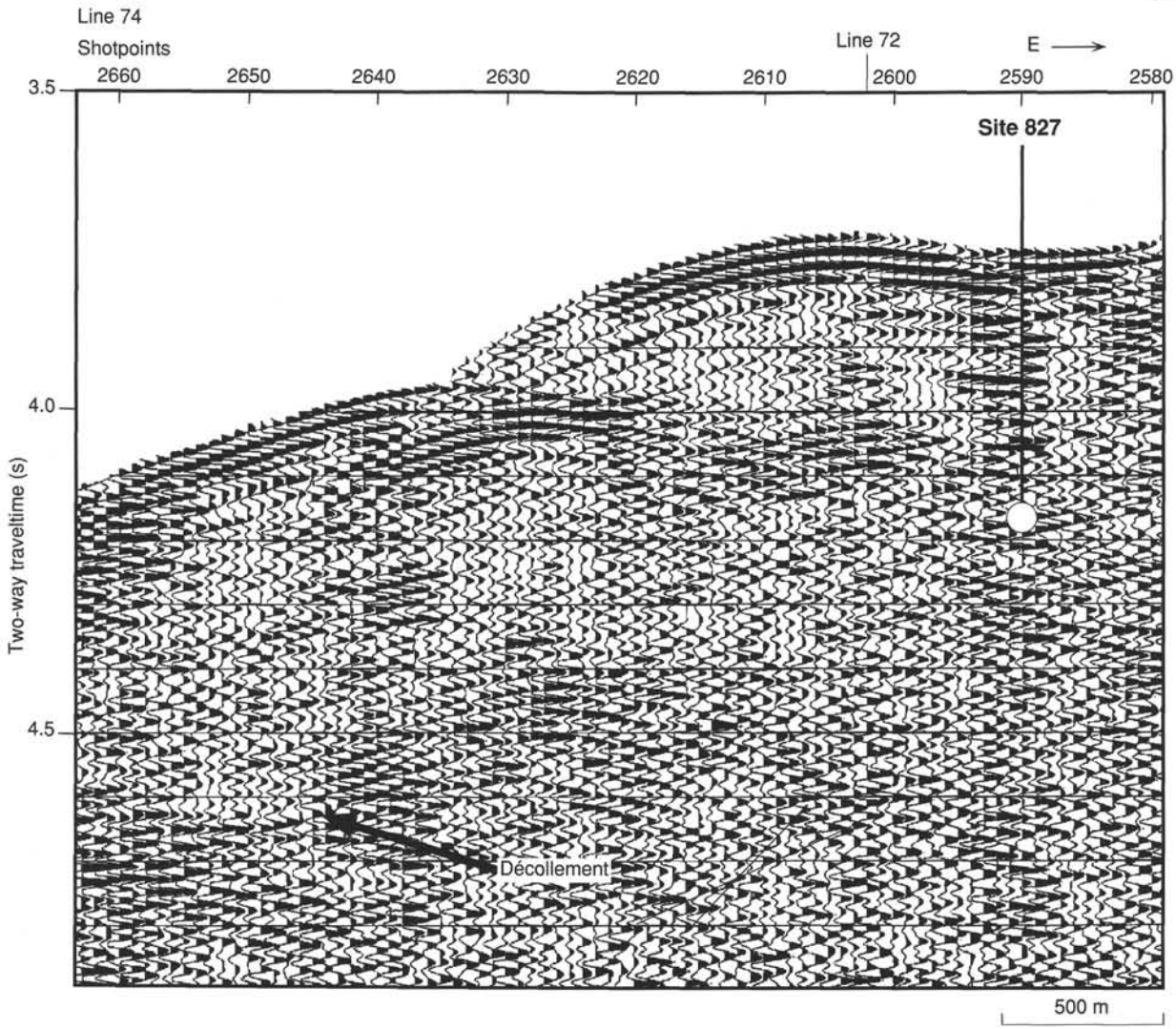

Figure 5. Part of single-channel seismic line 74 which crosses Site 827. The white bar shown below this site at about 4.05 s represents the top of the conglomerate. The white ball represents the approximate traveltime to the total depth of Hole 827B (400.4 mbsf).

4.5 s below the drill site that can be traced on other seismic lines to correlate with either the top of the ridge sediment or the top of the igneous basement. In either case this reflection is interpreted to correlate with the interplate décollement. The sub-bottom traveltime to this reflection below the drill site is about 0.8 s.

Line 72 does not actually cross the drill site but shows a better image of the décollement than does line 74, which does cross the site. The difference in reflection images of these two lines results from the anisotropic acoustic response from rocks under the lower forearc slope. This anisotropy had already been noticed in multichannel seismic data, and its main characteristic is that lines collected parallel to the arc slope show clearer geologic images than do lines collected perpendicular to the slope. Apparently, slope structures are more acoustically coherent along strike than across the structural grain. The imaging anisotropy holds as well for single-channel seismic reflection data presented here, in that the décollement is invisible below the site along line 74 (Fig. 5, whereas this feature is clearly imaged along line 72 (Fig. 6) and is marginally well imaged along line 76 (not shown).

The strong reflection that is presumed to be from the interplate décollement was one of the primary targets of the drilling at this site, and preliminary velocity data ("Physical Properties" section, this chapter) indicate that the sub-bottom depth of this feature is between 800 and 1000 m. These velocity data were measured on siltstone, which makes up only the upper 200 m or so of the core. We used other velocity data, obtained while processing multichannel seismic data, to fill in the gap in velocity information from below 200 m. Owing to deep water, these velocities, and consequently depth estimates made from them, can be in error by as much as 10%–20%. We assumed that the velocity in rocks below 200 m lies between 2500 m/s and 3000 m/s. Because the bottom of the hole is at 400.4 mbsf, a rock thickness between 400 and 600 m remained to be penetrated to reach the reflector.

Holes 827A and 827B show that a conglomerate underlies the siltstone beginning at 252 mbsf, which corresponds to a sub-bottom traveltime of 0.3 s. No obvious, strong reflections occur on any of the seismic sections at this traveltime directly below the drill site. However, along line 74, a reflection at the 0.3-s traveltime ends just west of this site. This reflection extends to the seafloor where the reflector outcrops at the foot of one of the numerous sharp seafloor scarps that are evident in Seabeam bathymetric data. In as much as such scarps may result from thrust faulting, one

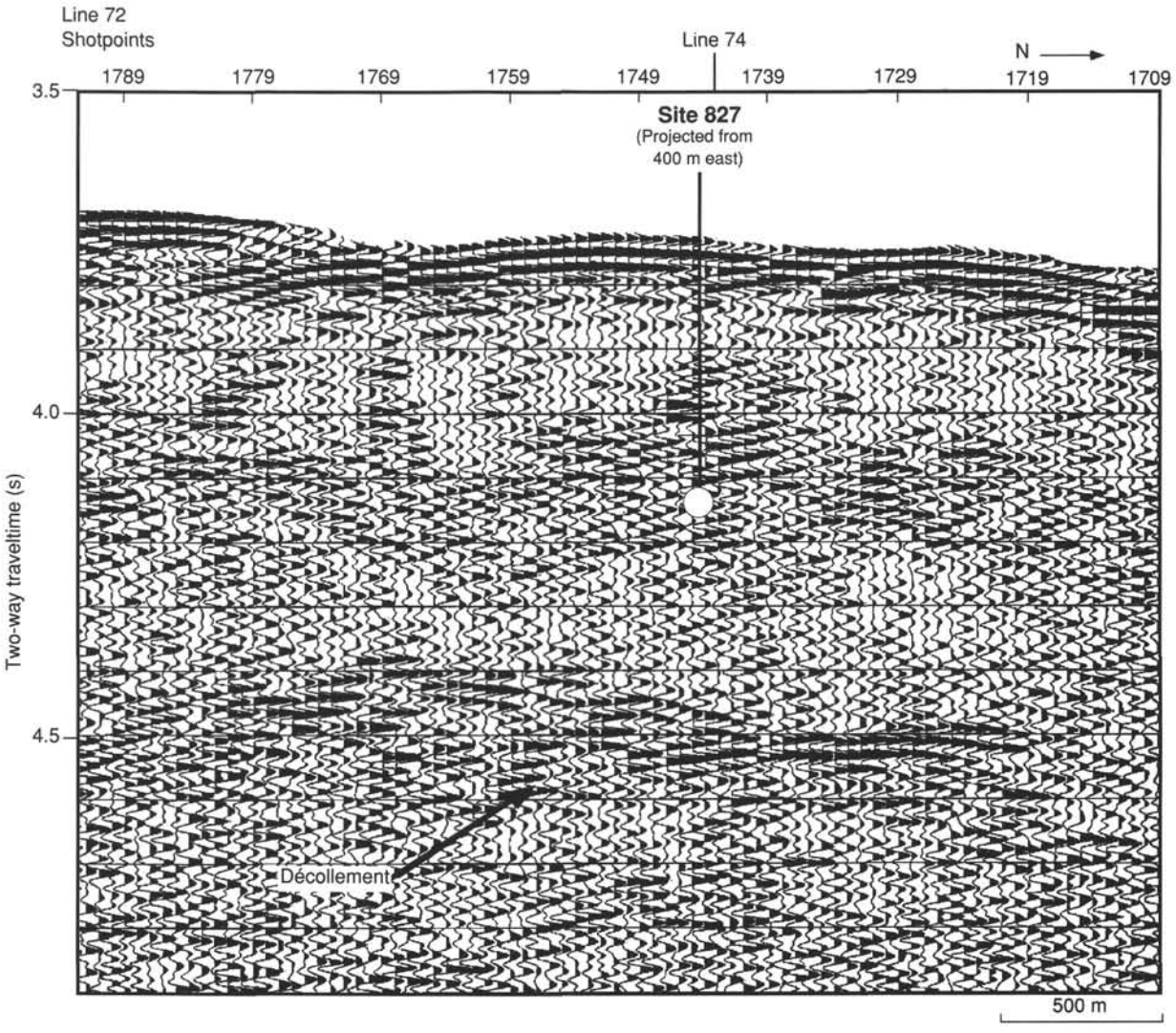

Figure 6. Part of single-channel seismic line 72 which crosses just west of Site 827. The white bar shown below this site at about 4.05 s represents the top of the conglomerate. The white ball represents the approximate traveltime to the total depth of Hole 827B.

possibility is that this reflection images a fault and that the conglomerate underlies this fault. No confirmation for such a fault can be obtained from the cores because of low core recovery.

Along line 72, a horizontal band of highly discontinuous, disorganized reflections begins above but near the conglomerate top. The onset of this band, however, results at least partly from the 0.3-s AGC operator used in data processing. This operator overcompensates for the strength of the seafloor reflection by clamping down on the amplitude of reflections from rocks just under the seafloor. Locating the top of this reflection zone by varying the length of the AGC operator was useless because of a high signal-to-noise ratio. Thus, the depth to the top of this zone of chaotic reflections is not known but the zone does appear to have a base at about 4.2 s, or about 80 m below the bottom of this drill hole.

OPERATIONS

Leg 134 began with the first mooring line at the Port of Townsville, Queensland, Australia at 2000 hr Universal Time Coordinated (UTC), 10 October 1990. Fuel for the vessel was not available in Townsville, so the port call was shortened. On 14 October at 0200 UTC, the *JOIDES Resolution* left Townsville and sailed 430 nautical miles (nmi) southeast to refuel at Gladstone. The ship arrived at 1715 UTC on 15 October, picked up fuel, and at 2030 UTC on 16 October sailed for Vanuatu.

A fairly extensive preliminary survey was carried out in the initial operating area and positioning beacons were dropped on proposed sites DEZ-1 and DEZ-2 before the vessel took station on the latter. A fairly flat, yet hummocky area was selected for Site 827 because it appeared to have a thick sediment cover.

Hole 827A

Seafloor depth was established at 2814.2 mbsl on the basis of an advanced piston core (APC) taken at 0410 UTC on 21 October. After two additional APC cores, the volcanic silt became too stiff for full penetration of the APC. Coring then proceeded by the advance-by-recovery method. Ten additional cores were taken with good results before core recovery became insufficient. The extended core barrel (XCB) system was used to recover two XCB cores, after which low penetration rate (ROP) and a temporary electrical breakdown of the coring winch prompted the decision to trip the drill string for the rotary core barrel (RCB) bottom-hole assembly (BHA).

Table 1. Coring summary for Holes 827A and 827B.

Core	Date (1990)	Time (UTC)	Depth (mbsf)	Length cored (m)	Length recovered (m)	Recovery (%)	Age
134-827A-							
1H	21 October	0450	0.0–9.8	9.8	9.76	99.6	Pleistocene
2H	21 October	0520	9.8–19.3	9.5	9.73	102.0	Pleistocene
3H	21 October	0600	19.3–28.8	9.5	9.73	102.0	Pleistocene
4H	21 October	0910	28.8–36.5	7.7	7.82	101.0	Pleistocene
5H	21 October	0955	36.5–44.9	8.4	8.39	99.9	Pleistocene
6H	21 October	1030	44.9–52.8	7.9	7.92	100.0	Pleistocene
7H	21 October	1110	52.8–61.0	8.2	8.24	100.0	Pleistocene
8H	21 October	1345	61.0–67.0	6.0	5.95	99.1	Pleistocene
9H	21 October	1440	67.0–72.5	5.5	5.47	99.4	Pleistocene
10H	21 October	1530	72.5–77.6	5.1	5.13	100.0	Pleistocene
11H	21 October	1800	77.6–83.2	5.6	5.67	101.0	Pleistocene
12H	21 October	1900	83.2–87.8	4.6	4.60	100.0	Pleistocene
13H	21 October	2000	87.8–91.5	3.7	3.73	101.0	Pleistocene
14X	21 October	2215	91.5–101.0	9.5	1.55	16.3	Pleistocene
15X	22 October	0500	101.0–110.6	9.6	7.07	73.6	
Coring totals				110.6	100.76	91.1	
134-827B-							
1R	22 October	1720	110.6–117.6	7.0	6.17	88.1	Pleistocene
2R	22 October	1810	117.6–127.2	9.6	8.31	86.5	Pleistocene
3R	22 October	1905	127.2–136.9	9.7	9.45	97.4	Pliocene
4R	22 October	2000	136.9–146.5	9.6	9.49	98.8	Pliocene
5R	22 October	2050	146.5–156.2	9.7	6.44	66.4	Pliocene
6R	22 October	2130	156.2–165.8	9.6	7.88	82.1	Pliocene
7R	22 October	2230	165.8–175.4	9.6	7.75	80.7	Pliocene
8R	22 October	2310	175.4–185.1	9.7	9.71	100.0	Pliocene
9R	23 October	0000	185.1–194.7	9.6	7.88	82.1	Pliocene
10R	23 October	0245	194.7–204.4	9.7	8.23	84.8	Pliocene
11R	23 October	0350	204.4–214.0	9.6	4.07	42.4	Pliocene
12R	23 October	0520	214.0–223.7	9.7	4.28	44.1	Pliocene
13R	23 October	0650	223.7–233.3	9.6	9.56	99.6	Pliocene
14R	23 October	0820	233.3–243.0	9.7	3.88	40.0	Pliocene
15R	23 October	0935	243.0–252.6	9.6	8.37	87.2	Pliocene
16R	23 October	1215	252.6–262.3	9.7	0.41	4.2	Pliocene
17R	23 October	1425	262.3–272.0	9.7	0.26	2.7	
18R	23 October	1630	272.0–281.7	9.7	0.39	4.0	
19R	23 October	1835	281.7–291.3	9.6	0.25	2.6	
20R	23 October	2100	291.3–301.0	9.7	0.12	1.2	
21R	23 October	2300	301.0–310.6	9.6	0.13	1.4	
22R	24 October	0130	310.6–320.3	9.7	1.81	18.6	
23R	24 October	0350	320.3–329.5	9.2	0.23	2.5	
24R	24 October	0550	329.5–339.0	9.5	0.12	1.3	
25R	24 October	0950	339.0–345.7	6.7	0.51	7.6	
26R	24 October	1300	345.7–355.3	9.6	0.42	4.4	
27R	24 October	1600	355.3–365.0	9.7	0.51	5.3	
28R	24 October	2000	365.0–374.5	9.5	0.40	4.2	
29R	24 October	2210	374.5–384.2	9.7	0.17	1.8	
30R	25 October	0045	384.2–393.9	9.7	1.77	18.2	
31R	25 October	0500	393.9–400.4	6.5	0.07	1.1	
Coring totals				289.8	119.04	41.1	

Total penetration was 110.6 mbsf. Overall core recovery was 91% (Table 1). Three successful bottom-hole temperature measurements were made with the instrumented probe (WSTP).

Hole 827B

The second hole was drilled to the total depth of Hole 827A (110.6 mbsf) before continuous RCB coring began. Core recovery was very good in volcanic silt to about 252 mbsf. Recovery and ROP then dropped drastically in an unconsolidated conglomerate that contained clasts up to boulder size. Hole conditions deteriorated progressively with depth and operations were halted prior to reaching basement for the safety of the drill string.

The total penetration was 400.4 mbsf. Recovery averaged 41%, nearly all of which was from the upper lithostratigraphic unit (Table 1). Two additional WSTP temperature measurements were made.

LITHOSTRATIGRAPHY

Sedimentary Units

Holes 827A and 827B penetrated 400.4 m of sedimentary rocks. Seismic reflection data indicate at least several hundred meters of additional sediments exist below the drilled interval (see "Seismic Stratigraphy" section, this chapter). The majority of the sediments are composed of either crystal grains or lithic fragments of volcanic origin. Breccia and conglomerate composed dominantly of clasts of volcanic sandstone or siltstone are described as "sed-lithic."

The cores begin in undifferentiated Pleistocene sediments and penetrate sediments at least as old as late Pliocene. Reworked early Pliocene and Miocene microfossils occur throughout the section (see "Biostratigraphy" section, this chapter). These microfossils may have been originally deposited with the volcaniclastic rocks that were subsequently

Table 2. Lithostratigraphic units, Site 827.

Unit	Subunit	Depth (mbsf)	Thickness (m)	Age
I		0–86	86	Pleistocene
	IA	0–40	40	Pleistocene
	IB	40–66	26	Pleistocene
	IC	66–86	20	Pleistocene
II		86–141	55	late Pliocene to Pleistocene
III		141–252.6	111	late Pliocene to middle Pleistocene
	IIIA	141–200	59	late Pliocene or middle Pleistocene
	IIIB	200–218	18	late Pliocene
	IIIC	218–252.6	34.6	late Pliocene
IV		252.6–400.4	147.6	Indeterminate (barren)

eroded to produce the sediment at Site 827. Some of the clasts in the Pliocene/Pleistocene breccias and sandstones contain Eocene microfossils. Below 262 mbsf, too little matrix sediment was recovered to allow paleontological age determination.

The cored section is divided into four main lithostratigraphic units (Table 2 and Fig. 7), primarily on the basis of sedimentary texture and structures identified in visual core descriptions, grain size, and mineralogy estimates from smear slides and total carbonate measured by coulometric analyses (Figs. 8 and 9). We also considered physical properties and biostratigraphic data and found that information consistent with, or partially supportive of, our lithostratigraphic unit divisions.

There are some discrepancies between names assigned to lithologies on the barrel sheets and mineral composition indicated by coulometric analyses (Fig. 8). We used preliminary core descriptions in sediment classification, and the designation of a lithostratigraphic unit as "calcareous" was based on smear-slide estimates of the proportion of total carbonate. Where those, admittedly subjective, analyses indicated at least 25% total carbonate, we followed the classification scheme (see "Explanatory Notes Chapter," this volume) and designated the sediments "calcareous." Despite the fact that chemical analyses of total carbonate in some cases indicate considerably less carbonate than the smear-slide estimates, we retained our initial classifications when we compiled the barrel sheets. We did this because the estimates indicate relative amounts of carbonate and other materials, even if they are not fully consistent with percent carbonate determined by coulometric analyses. Moreover, the coulometric and smear-slide samples are not from the same core intervals; therefore, identical results should not be expected.

Lithostratigraphic Units

Unit I

Depth: 0–86 mbsf
Interval: Section 134-827A-1H-1, 0 cm, to Section 134-827A-12H-2, 90 cm
Thickness: 86 m
Age: Pleistocene

Unit I is composed of a Pleistocene section of dark gray (5Y 3/1–4/1) to dark greenish gray (10Y 3/1–4/1), unlithified volcanic silt with interbeds of very dark gray (5Y 3/1), normally graded, volcanic silty sand. Unit I is subdivided into three subunits on the basis of the frequency and thickness of graded beds (Fig. 10). Much of the silt is included in the top parts of the fining-upward sand beds, particularly in Subunits IA and IB. Because the subunits significantly differ only in the number and thickness of graded beds, grain mineralogy and texture is described only for Subunit IA.

Subunit IA

Depth: 0–40 mbsf
Interval: Section 134-827A-1H-1, 0 cm, to Section 134-827A-5H-2, 150 cm
Thickness: 40 m
Age: Pleistocene

Subunit IA consists of volcanic silt and volcanic silty sand comprising a sequence of graded beds with distinct, very dark gray basal units of volcanic silty sand, often with scoured bases. These sands fine upward to the greenish gray volcanic silts that comprise most of the unit. The silt beds in Unit IA are probably, for the most part, the finer-grained upper parts of the graded volcanic sandy silt beds. Assuming this to be the case, the graded beds range in thickness from 3 to 15 cm with a mean of 7.5 cm. There are on average about 20 of the sandy-based units per section (or 13 per meter) in this subunit (Fig. 10).

The sands and silts are similar in composition, predominantly consisting of plagioclase, quartz, carbonate grains, pyroxenes, and opaque minerals such as magnetite and hematite, with a small clay component (Figs. 8 and 9). Ten percent of the sediment is composed of silt-sized calcite crystals of unknown origin, foraminifers, and nannofossils (Fig. 8). Foraminifers are particularly abundant in the sand-sized sediments.

Subunit IB

Depth: 40–66 mbsf
Interval: Section 134-827A-5H-2, 150 cm, to Section 134-827A-8H-4, 50 cm
Thickness: 26 m
Age: Pleistocene

Subunit IB, like Subunit IA, is primarily composed of volcanic silt with interbeds of normally graded, volcanic silty sand, which range in thickness from 1 to 8 cm (Fig. 11). Thickness and frequency of graded beds differ in Subunits IB and IA: Subunit IB has about 30 beds per meter, yielding an average thickness of about 3.3 cm, compared with the approximately 13 beds per meter and 7.5 cm average thickness in Subunit IA (Fig. 10).

Subunit IC

Depth: 66–86 mbsf
Interval: Section 134-827A-8H-4, 50 cm, to Section 134-827A-12H-2, 90 cm
Thickness: 20 m
Age: Pleistocene

Subunit IC is primarily composed of volcanic sandy to clayey silt with normally graded interbeds featuring basal silty sands with scoured bases. Average distance between sandy interbeds increases from the 3.3 cm of Subunit IB to about 13 cm, and ranges up to 70 cm. The most significant feature of this subunit is the appearance of thick (up to 70 cm), bioturbated layers of volcanic clayey silt, which contrasts with the silts and sandy silts that separate the closely spaced sandy beds in this as well as the other subunits. The clayey silts are often mottled in appearance, indicating bioturbation, with occasional trace fossils. At 70.3–70.8 mbsf, the volcanic clayey silt shows convoluted bedding characteristic of sediment slumping.

Unit II

Depth: 86–141 mbsf
Interval: Section 134-827A-12H-2, 90 cm, to Section 134-827B-4R-3, 90 cm
Thickness: 55 m
Age: late Pliocene to Pleistocene

Unit II consists of dark to very dark greenish gray (10Y 4/1–3/1) volcanic silt and partially lithified volcanic siltstone with

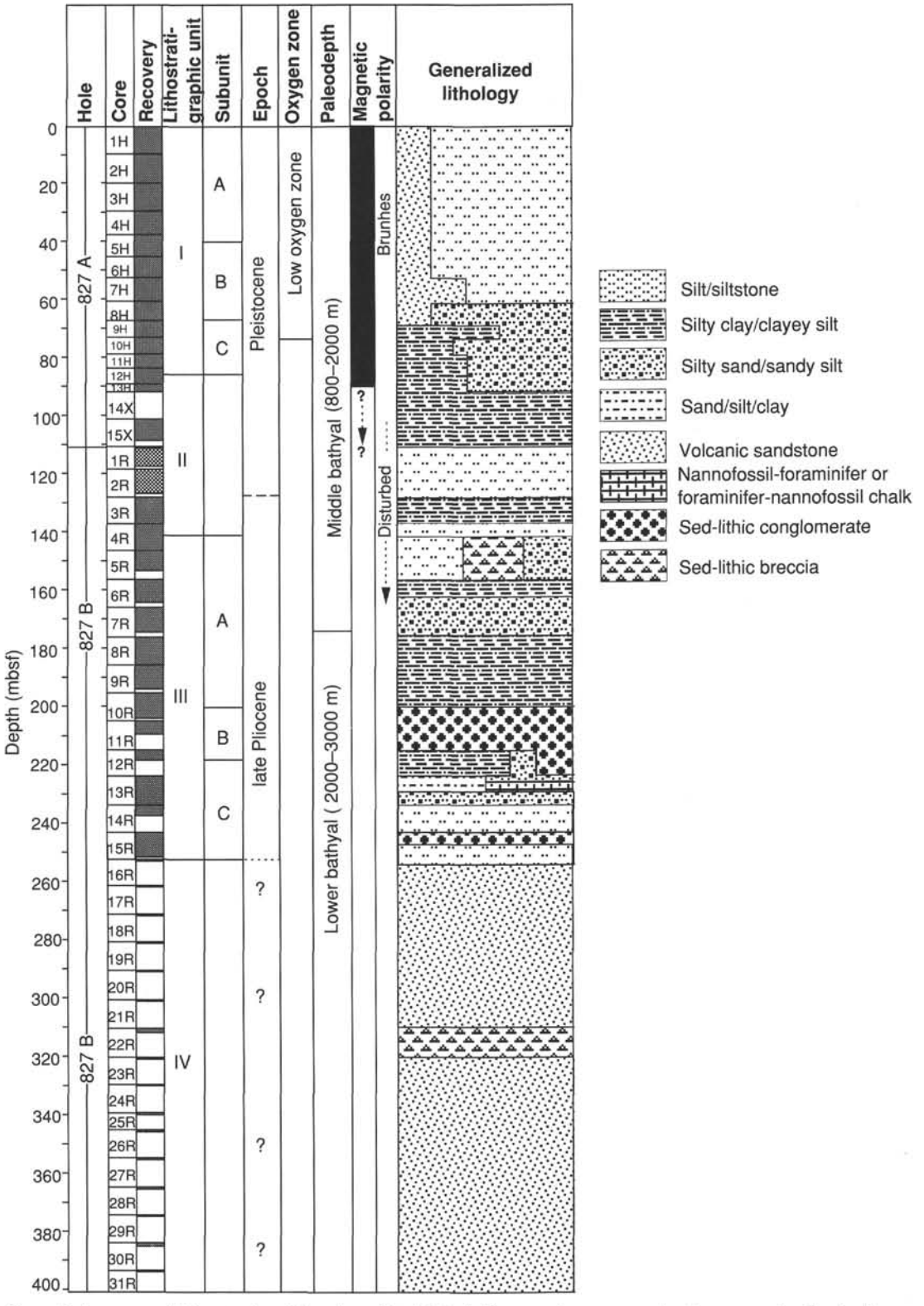

Figure 7. Summary of lithostratigraphic units at Site 827 including sample recovery, depth, ages, and paleodepth estimates from benthic foraminifers.

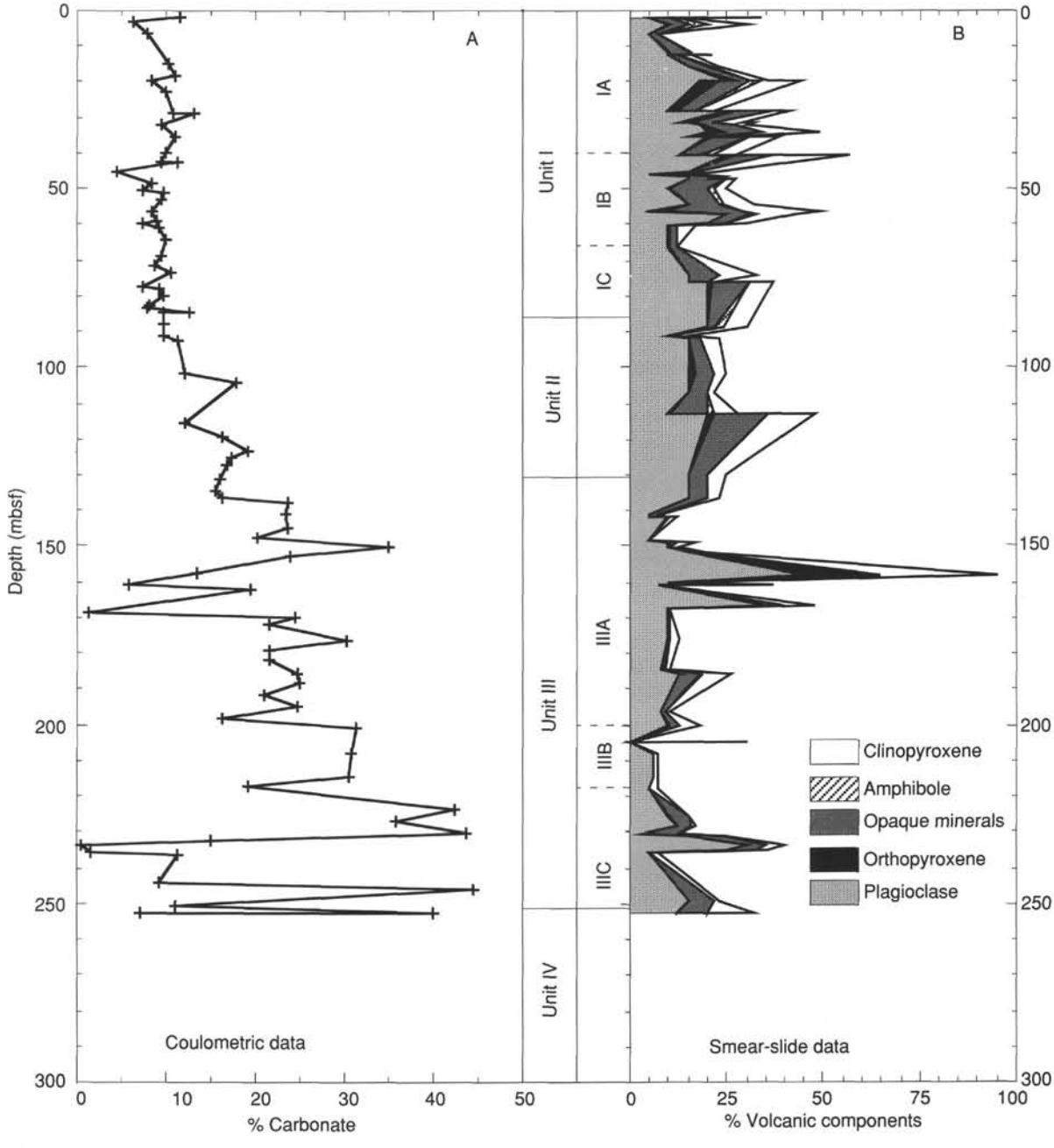

Figure 8. Mineralogical data downcore at Site 827. The peak in volcanogenic mineral grains in Subunit IIIA results from inclusion of data from a sed-lithic interval. There are no data from Unit IV because the recovery rate was extremely low. Carbonate percentages indicate a general increase with depth. The occurrence of noncarbonate minerals throughout the sequence documents a proximal volcanic source, most likely the Miocene volcaniclastic rocks of the Western Belt of central Vanuatu.

varying proportions of volcanic clay and sand (Fig. 9). Total carbonate content increases with depth in the unit, from approximately 10% in the unlithified silt at the top of the unit (86–110 mbsf), to 15%–20% in the partially lithified siltstone (110–141 mbsf; Fig. 8). As in Unit I, the sediments predominantly consist of quartz, volcanogenic feldspar, and calcareous grains, with minor amounts of clinopyroxene, olivine, chlorite, amphibole, chlorite, and opaque minerals (e.g., hematite, magnetite), and a small clay component (Fig. 8). Unit II is distinguished from Unit I by the absence of normally graded sandy interbeds, and the increasing presence of mottled and bioturbated beds. There is no evidence of systematic variations in grain size.

Unit III

Depth: 141–252.6 mbsf
Interval: Section 134-827B-4R-3, 90 cm, to Section 134-827B-15R-CC, 15 cm
Thickness: 111 m
Age: late Pliocene or middle Pleistocene

Unit III primarily consists of highly bioturbated, very dark greenish gray (10Y 3/1–4/1) to dark gray (5Y 3/1), partially lithified calcareous volcanic siltstone. Some sections contain intervals of sed-lithic conglomerate and breccia primarily consisting of sand-to-cobble-sized clasts of lithified volcanic siltstone and sandstone, with less abundant clasts of limestone and volcanic rock.

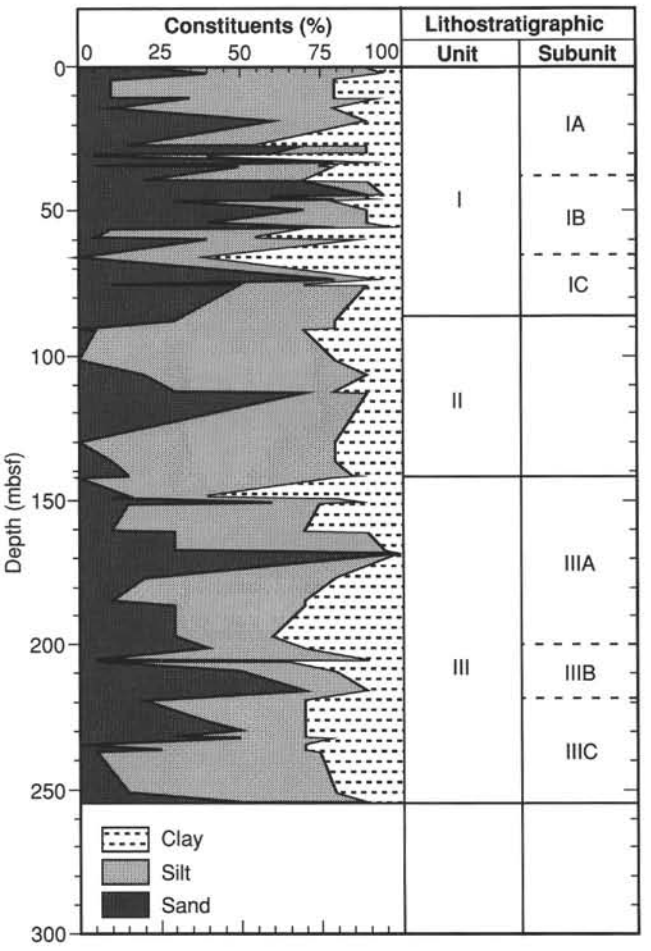

Figure 9. Variations in proportions of sand-, silt-, and clay-sized sediments in the upper 252 m at Site 827 based on smear-slide descriptions. The highest proportion of sand occurs in Unit I because of the large number of graded beds that have sand-sized bases.

Unit III differs from Units I and II because it has significant amounts of material larger than sand-sized grains; its carbonate content (20%–25%; Fig. 8) is also higher than the units above. Some intervals between 204 and 233 mbsf are rich in pelagic calcareous microfossils, with proportions ranging up to 70% foraminifers and nannofossils. The division between Units II and III is based upon an increase in lithification from Unit II to Unit III, which is reflected in the highly brecciated and tectonically sheared condition of the material below 141 mbsf.

Subunit IIIA

Depth: 141–200 mbsf
Interval: Section 134-827B-4R-3, 90 cm, to Section 134-827B-10R-4, 120 cm
Thickness: 59 m
Age: late Pliocene or middle Pleistocene

Subunit IIIA primarily consists of highly bioturbated, very dark greenish gray (10Y 3/1–4/1) to dark gray (5Y 3/1), sandy to clayey, volcanic siltstone. It is characterized by variable amounts of carbonate (<35%) and volcanogenic minerals (generally <25%; Fig. 8). Subunit IIIA is also characterized by 10-cm-thick intervals of sed-lithic conglomerate containing rounded to angular clasts of volcanic siltstones and sandstones, ranging in size from coarse sand to pebbles. Clasts are light colored, with a composition similar to or less calcareous

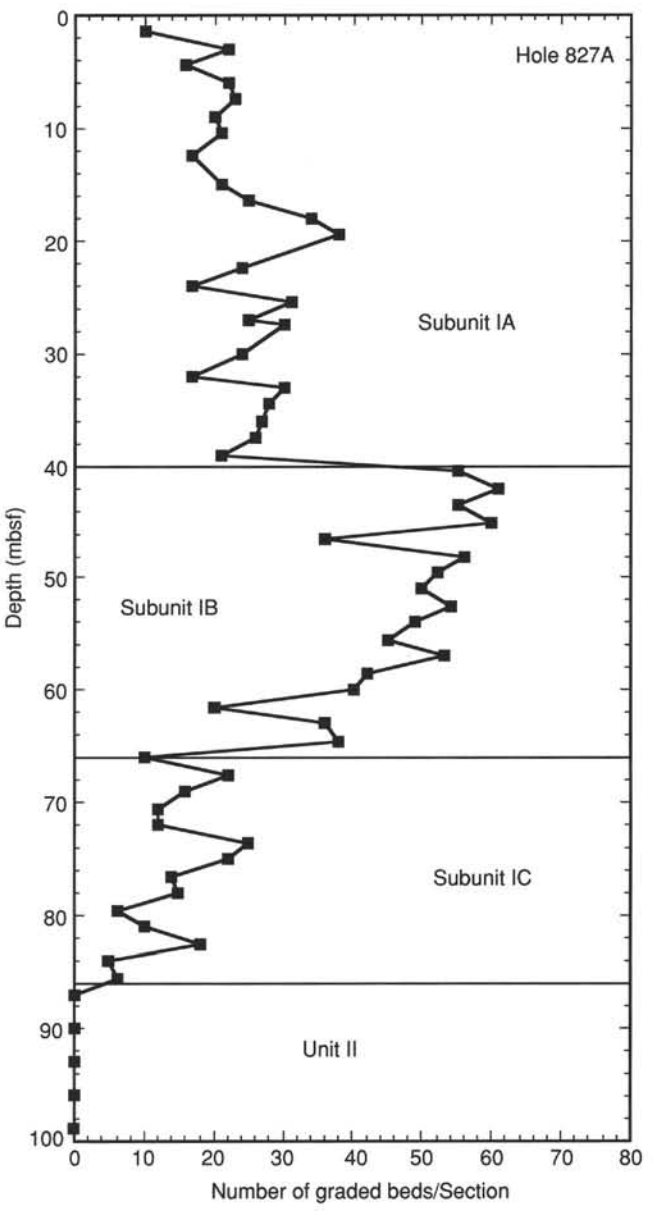

Figure 10. The number of graded beds per section (1.5 m) of core ranges from less than 10 to more than 60. All of the graded beds are restricted to Unit I, which provides a significant boundary between Units I and II.

than that of the matrix; one clast examined consisted of 95% volcanogenic minerals (Fig. 8).

Much of the unit is highly sheared and fractured, and numerous examples of sand- and gravel-sized material appear as fingers and stringers in the siltstone. Such features probably result from wet-sediment deformation and may be clastic dikes.

Subunit IIIB

Depth: 200–218 mbsf
Interval: Section 134-827B-10R-4, 120 cm, to Section 134-827B-12R-3, 90 cm
Thickness: 18 m
Age: late Pliocene or Pleistocene

Subunit IIIB primarily consists of grain- to matrix-supported sed-lithic conglomerate and breccia, with minor calcareous siltstone. Conglomerate clasts range in size from 0.5 to 5

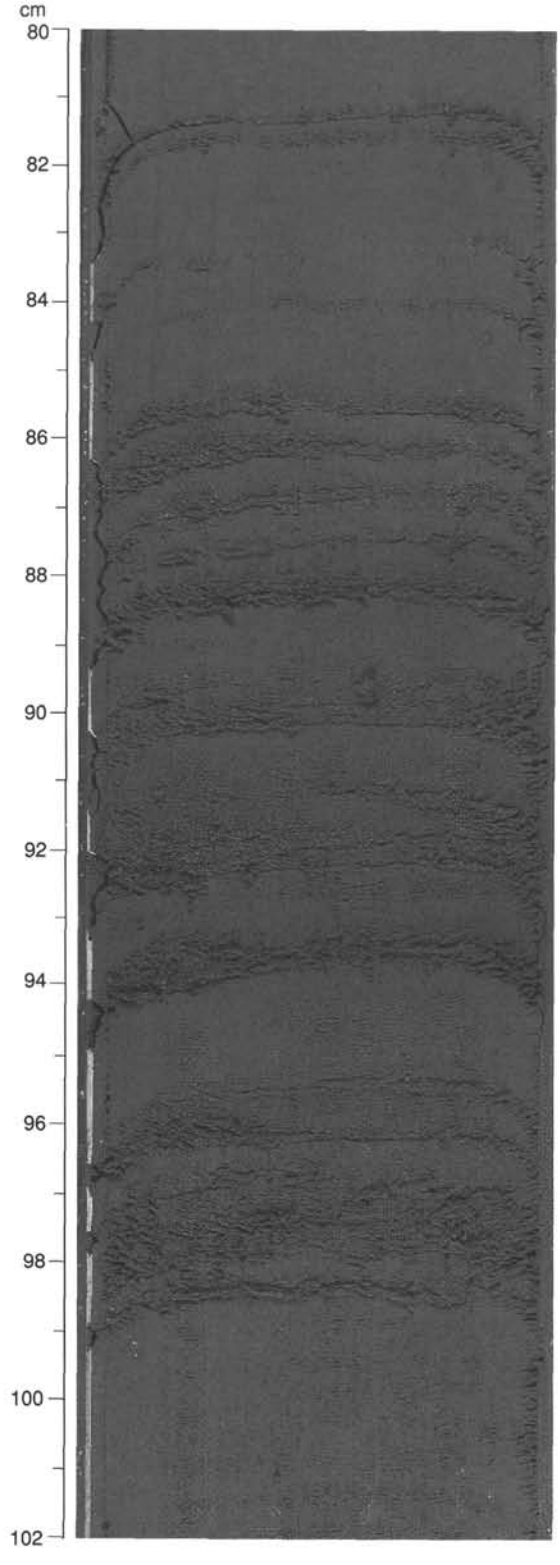

Figure 11. Photograph of interval 134-827A-5H-5, 80–102 cm, showing a zone of very closely spaced graded beds from Subunit IB.

cm, are rounded to angular, and are composed mainly of dark greenish gray (10Y 4/1) volcanic siltstone. Rare clasts of pelagic limestone, scleractinian coral, and volcanic rock occur. Clastic dikes of sand and sandy conglomerate penetrate siltstone in Section 134-827B-12R-3. Volcanogenic minerals consistently comprise less than 10% of Subunit IIIB (Fig. 8).

Subunit IIIC

Depth: 218–252.6 mbsf
Interval: Section 134-827B-12R-3, 90 cm, to Section 134-827B-16R-1, 0 cm
Thickness: 34 m
Age: late Pliocene or Pleistocene

Subunit IIIC consists of volcanic siltstone with thin ash layers and intervals rich in pelagic foraminifers and nannofossils. For example, Core 134-827B-13R predominantly consists of calcareous pelagic microfossils, and Section 134-827B-14-2, 62–65 cm, is a chalk bed. A highly sheared, variegated, greenish lustrous zone (chloritic?) occurs in Section 134-827B-13R-5, 95–125 cm (Fig. 12). In addition, this interval is rich in calcareous pelagic microfossils. Major sediment components are similar to the volcanogenic terrigenous grains dominating the overlying units.

Unit IV

Depth: 252.6–400.4 mbsf
Interval: Section 134-827B-16R-1, 0 cm, to Section 134-827B-31R-CC
Thickness: 147.8 m
Age: Indeterminate (barren)

The lithology of Unit IV is not well known because of poor core recovery. The material recovered is probably highly selective and its surface texture modified by the drilling process. Most of the cores contain 10–65 cm of dark gray (5Y 2.5/1–3/1) to dark greenish gray (10Y 3/1–5/1), very angular to rounded, pebble- to cobble-sized, lithified volcanic siltstone and sandstone pieces. (We suspect that many of the pieces were made round by the drilling process.) The only exceptions to the poor recovery are Cores 134-827B-22R and 134-827B-30R, each of which contained nearly 2 m of lithified volcanic siltstone and sandstone clasts, similar to the pieces of rock recovered in other cores from Unit IV. The clasts occur in a highly sheared and fractured matrix of partially lithified, very dark greenish gray (10Y 3/1), sandy silt, so we classify the rock as a partially lithified, matrix-supported sed-lithic conglomerate. We assume that the lithostratigraphy of Unit IV can be characterized by these sections although more than 95% of this interval was not recovered.

The only igneous rocks encountered at Site 827 occurred as clasts in pieces of breccia (or as clasts from which we believe that the matrix was removed by drilling) in Unit IV. The ig-lithic and igneous clasts were dispersed in an unconsolidated, volcaniclastic, gravel- to sand-sized matrix and were composed mainly of porphyritic andesite with abundant (27%) phenocrysts of plagioclase and rather rare clinopyroxene and opaque mineral grains in a fine-grained groundmass that consists primarily of plagioclase in association with secondary minerals, chlorite, carbonate, and clay. One clast has a slightly more evolved composition and is referred to as a dacitic sed-lithic breccia clast; it is more feldspathic than the andesitic sed-lithic breccia clasts and contains a small proportion of quartz (~1%). The majority of the clasts appear to be derived from lithified breccias or coarse sandstones containing a preponderance of igneous rock fragments and crystals.

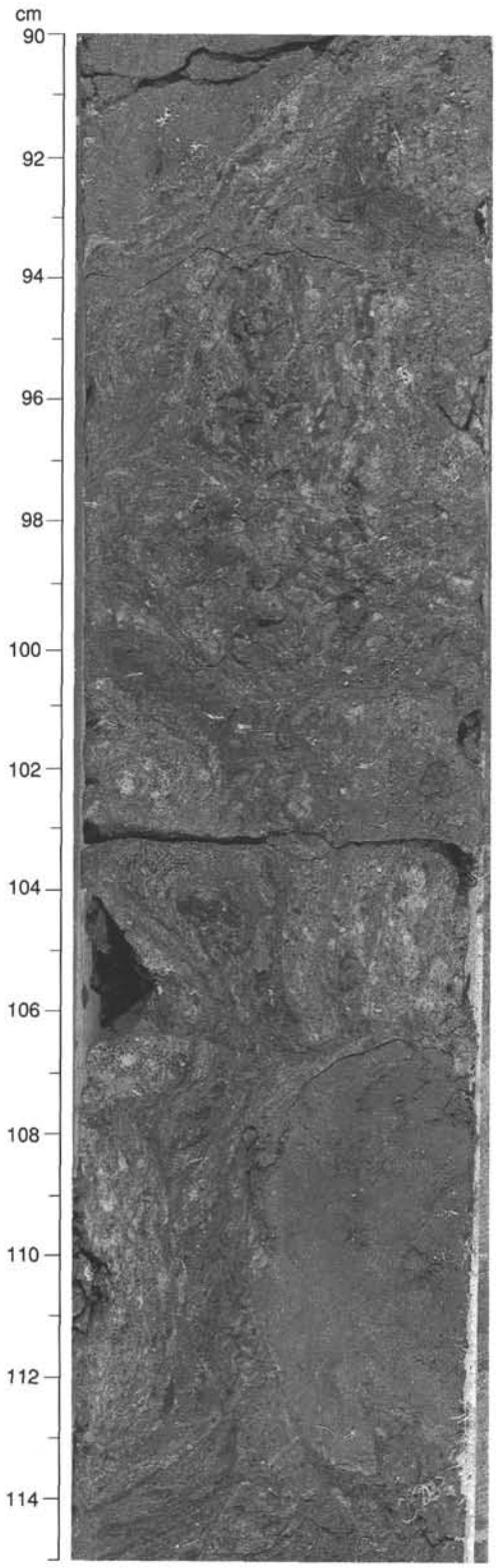

Figure 12. Photograph of interval 134-827B-13R-5, 90–115 cm, showing the extremely sheared, micaceous carbonate interval in Unit IIIC.

Depositional Environment and Processes

Drilling began at a depth of 2803 mbsl in a small flat-floored basin on a submarine slope that deepens westward from Wousi Bank, an area of shallow seafloor protruding westward from Espiritu Santo Island (Fig. 8). The summit of Wousi Bank nearly breaks the sea surface, but a channel about 200 m deep separates the bank from Espiritu Santo Island.

Detailed Seabeam bathymetry of Collot and Fisher (1991) shows that most sediment derived from Espiritu Santo Island inshore of Wousi Bank is likely to be intercepted by this channel and diverted into a series of submarine canyons that carry it north or south of Site 827 and to the base of the slope in the West Santo Basin or the d'Entrecasteaux Central Basin. Only fine-grained sediments carried in suspension reach Wousi Bank and its upper slopes. On Wousi Bank, such sediments can be mobilized as turbidity currents and transported downslope to Site 827.

The 7.6 m of rock recovered from Unit IV at 252–400.4 m downcore appear to be dominated by angular clasts of volcanic sandstone or siltstone (graywacke) with a few igneous clasts. Unfortunately, recovery in this interval was so poor that we are not certain of the composition, age, and paleodepths of deposition of the sediments. The sediment is extremely fractured and has a scaly texture indicating large amounts of shearing. The combination of strongly lithified clasts and a poorly lithified and sheared matrix probably explains the poor recovery.

Unit IV was most likely deposited in an environment similar to those at the mouths of submarine canyons at depths of about 5,000 m located farther north along the west coast of Espiritu Santo. Deposition by mass-wasting mechanisms proximal to a source is indicated by the poor sorting and angular to subangular shapes of the clasts. Possible mechanisms include debris flows accumulating at the base of a slope or in a submarine fan channels. However, questions remain as to the origin of the clasts and how they reached a location from which debris flows could transport them to Site 827. Some of the clasts evidently represent a first generation of breccia that accumulated after minimal erosion and transport close to an andesite/diorite source. Alternatively, the clasts may be a product of submarine erosion. Faulting or erosion on the inner trench slope could have brought tectonic breccia to the surface of the slope where debris flows would have carried it downslope.

Unit III is dominated by volcanic siltstones and sandstones and sed-lithic conglomerates. In addition, it has a higher proportion of carbonate than any other unit at Site 827 (Fig. 8), because of the abundance of calcareous microfossils. Occurrence of thin horizons with high concentrations of microfossils indicate periods without significant terrigenous sediment deposition. We propose that the matrix-supported sed-lithic conglomerates were deposited by debris flows either from slopes exposing coarse fault breccias (or previously deposited debris flow deposits) or from a nearshore source. However, Unit III may represent the waning phases of debris-flow deposition of the coarse-grained clastics observed in Unit IV. Paleontological data indicate lower bathyal paleodepths (2000–3000 m) for most of Unit III (Fig. 7).

Unit II marks a major change from Unit III in both the mechanism of sediment transport and the environment of sediment deposition. Sediments of Unit II document the change from debris flow and pelagic sedimentation mechanisms of Unit III to hemipelagic sedimentation of Unit II. Moreover, the complete absence of graded beds and of any other evidence of mass transport of sediments in Unit II suggests that there was not a continuous slope leading from a source of sediment.

We interpret Unit II to represent the isolation of Wousi Bank from Espiritu Santo Island as a source of coarse clastic sediments. The slope basin at Site 827 was created about this time and coarse sediments were diverted to the sides of the uplifting Wousi promontory rather than flowing more-or-less directly westward along the axis of the Wousi promontory to Site 827.

The sediments of Unit I consist almost entirely of graded beds of volcanic silt and sandy silt containing both Pleistocene and reworked Pliocene and Miocene microfossils. Sediments of Unit I are mineralogically similar but coarser-grained than those of Unit II. It is likely that some pelagic and hemipelagic sediments accumulated in the basin directly from the water column, but sedimentary beds of Unit I are mainly graded beds.

Sediments derived from Espiritu Santo Island would initially arrive at the shoreline as coarse and poorly sorted clastic and reworked carbonate sediments. Ultimately, these sediments are transported by turbidity currents to the basin where they were recovered at Site 827. The absence of coarse clastics in Unit I suggests that they were diverted to other areas as indicated by contemporary bathymetry (Collot and Fisher, 1991).

In summary, we suggest that sediment deposition at Site 827 began when western Espiritu Santo Island was uplifted as the Torres Massif began to be subducted. As the island emerged, debris flows delivered coarse sediment from the island via submarine canyons to the base of a steep slope at a depth of about 5000 m, similar to the setting west of northern Espiritu Santo Island (Collot and Fisher, 1991). By the early to middle Pleistocene the Northern d'Entrecasteaux Ridge was beginning to underthrust southern Espiritu Santo Island and deform the arc slope at Site 827. This deformation may have diverted debris flows to the north of Site 827 even as tectonic deformation was intensifying. The absence of debris flows and the relatively low relief of Espiritu Santo Island reduced the sedimentation rate at Site 827 so that pelagic oozes dominated the sediments during some periods. Depths indicated by microfossils were lower bathyal (2000–3000 m), shoaling to middle bathyal (800–2000 m) during the time of deposition of Subunit IIIA. This shallowing was most likely the result of the arrival of the North d'Entrecasteaux Ridge from the south and deformation of the arc slope.

In the middle(?) or late(?) Pleistocene, relatively slow hemipelagic sedimentation rates that were found in Unit II prevailed. The absence of even a single turbidite bed or other clear evidence of mass-transported sediment in Unit II suggests that Wousi Bank had been created, resulting in the isolation of Site 827 from a continuous slope or submarine canyon leading from Espiritu Santo Island. Only those sediments that moved in suspension to Wousi Bank were deposited at Site 827. Alternatively, some of these sediments may have moved down the slopes as turbidity currents.

The transition to the 86-m interval of turbiditic sediments in Unit I marks the transition to paleogeography and paleobathymetry similar to present. Magnetic polarity of the sediments in Unit I indicates that the entire unit is less than 700 Ka. Variations in frequency and thickness of turbidites between the Subunits IA, IB, and IC may represent the influence of glacio-eustatic sea-level fluctuations on sedimentation and variations in the rate of tectonic uplift (e.g., Jouannic et al., 1980; Taylor et al., 1985) and, perhaps, the frequency or magnitude of earthquakes.

BIOSTRATIGRAPHY

Calcareous Nannofossils

The calcareous nannofossil biostratigraphy in Holes 827A and 827B is typified by Pleistocene and upper Pliocene assemblages, often with considerable quantities (>50%) of reworked specimens ranging in age from early Pliocene to late Eocene. Abundance varies from rare to common depending on the degree of dilution from influxes of terrigenous and volcaniclastic materials. Preservation was good throughout the section.

Samples 134-827A-1H-CC through 134-827A-13H-CC fall within Zone CN15 (Fig. 13) and are characterized by the presence of *Emiliania huxleyi* with an accompanying assemblage containing *Gephyrocapsa oceanica, G. caribbeanica, Helicosphaera kamptneri, Rhabdosphaera claviger,* and *Calcidiscus leptoporus*. The Pliocene discoaster *D. brouweri* was documented in most of these samples but was considered reworked, as were Miocene discoasters *Discoaster berggrenii, D. variabilis,* and *D. quinqueramus*.

Samples 134-827A-14X-CC through 134-827B-7R-CC fall within Zone CN14 and are characterized by assemblages dominated by *Gephyrocapsa oceanica, G. caribbeanica,* small gephyrocapsids (<3 mm), and *Pseudoemiliania lacunosa*. This interval contains a moderate amount of reworked Pliocene and Miocene species including *Discoaster brouweri, D. berggrenii, D. deflandrei, Cyclicargolithus floridanus,* and *Sphenolithus neoabies*. Sample 134-827B-7R-CC also contains reworked Eocene nannofossils as indicated by the presence of *Discoaster barbadiensis*.

Samples 134-827B-8R-CC and 134-827B-9R-CC fall within Zone CN13 as indicated by assemblages that include *Pseudoemiliania lacunosa, Gephyrocapsa caribbeanica, Helicosphaera kamptneri,* and *Calcidiscus leptoporus*. *Discoaster berggrenii* and *D. brouweri* are common as reworked constituents from the Miocene and Pliocene, respectively.

Samples 134-827B-10R-CC through 134-827B-16R-CC contain assemblages typified by *Calcidiscus leptoporus, Pseudoemiliania lacunosa, Discoaster brouweri, Helicosphaera kamptneri,* and small gephyrocapsids. The presence of the Pliocene nannofossil *D. brouweri* coincident with the absence of *Gephyrocapsa caribbeanica* and other large gephyrocapsids leads to the conclusion that the presence of *D. brouweri* is no longer a product of reworking and thus a zonal determination of CN12d (latest Pliocene) is reached for these samples. Nannofossil abundances were recorded as rare and few for the interval from Sections 134-827B-13R-CC to 134-827B-16R-CC and, although a zonal determination of CN12d is indicated, the low abundances make this conclusion somewhat dubious (Fig. 13).

Both the quantity and source of reworked nannofossils from Sections 134-827B-10R-CC to 134-827B-16R-CC are varied: Samples 134-827B-10R-CC to 134-827B-12R-CC display no reworking and minor reworking respectively; Sample 134-827B-11R-CC contains clasts yielding a lower Eocene assemblage that include *Chiasmolithus grandis, Discoaster lodoensis,* and *D. barbadiensis* (CP12); Samples 134-827B-13R-CC through 134-827B-16R-CC contain Miocene discoasters.

Radiolarians

No radiolarians were found in any of the 27 samples examined from Hole 827A, with the exception of single, well-preserved specimens in Samples 134-827A-1H-2, 129–135 cm, 134-827A-4H-CC, and 134-827A-10H-3, 44–46 cm. Rare sponge spicules occur in practically all of the samples. Single fragments of diatom frustules were found in Samples 134-827A-8H-4, 65–66 cm, and 134-827A-12H-2, 8–10 cm.

Thirty-four samples from Hole 827B were examined for radiolarians, but the only four containing radiolarians are from middle Eocene clasts within the Pliocene silty matrix. Assemblages from two of these clasts indicate the *Phormocyrtis striata striata* Zone (Sample 134-827B-11R-1, 14–16 cm, and the bottom of Sample 134-827B-11-CC) and two indicate the

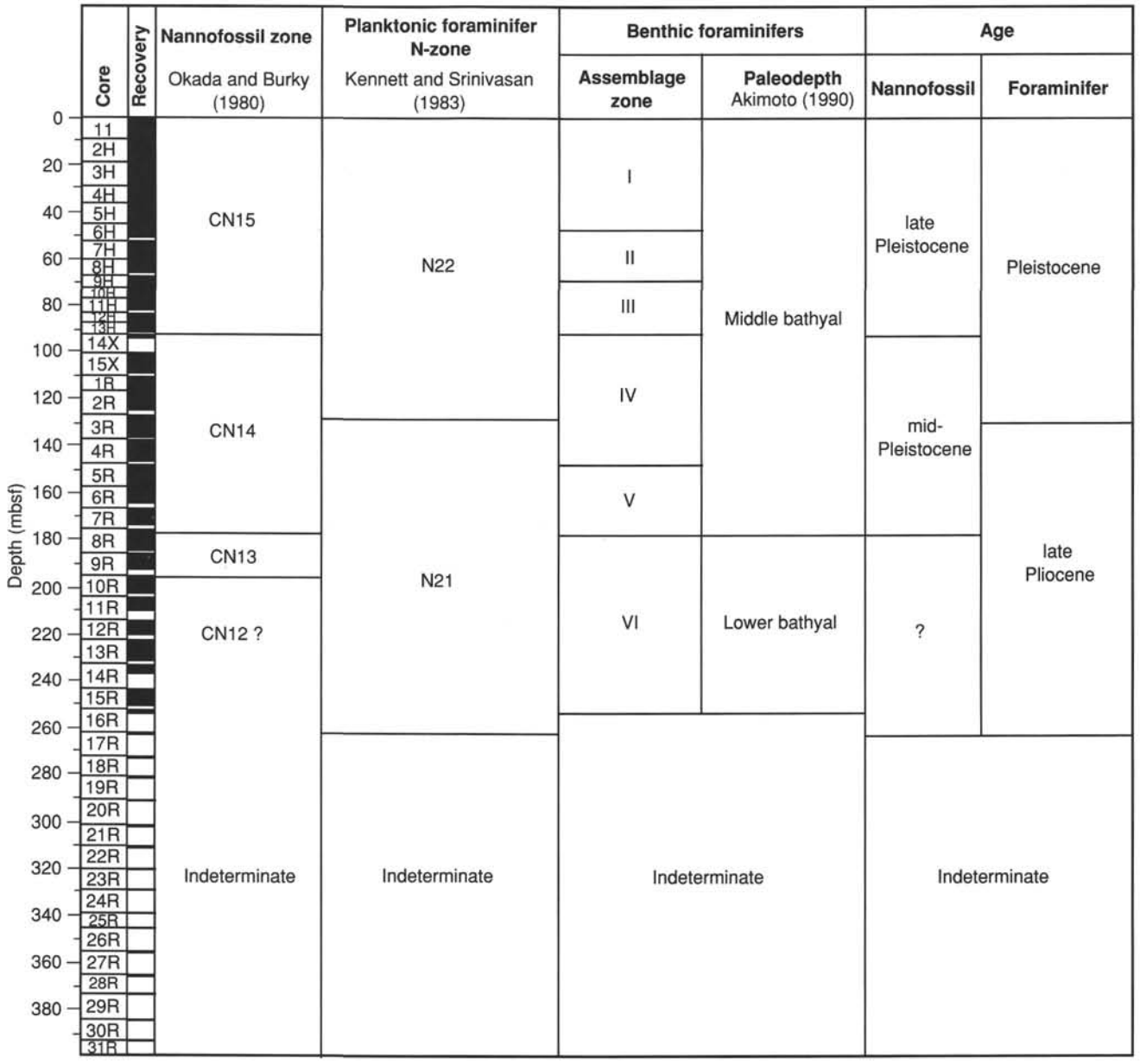

Figure 13. Biostratigraphic summary of Pleistocene to upper Pliocene sequence in Holes 827A and 827B.

Theocotyle cryptocephala Zone (Samples 134-827B-11R-1, 42–45 cm, and 134-827B-11-CC, 0–4 cm). These radiolarian zonal assignments support the age determination based on calcareous nannofossils, mentioned above.

Planktonic Foraminifers

The application of planktonic foraminiferal biostratigraphy to Holes 827A and 827B is constrained by the large amount of reworking encountered in many of the samples. Planktonic foraminifers were recovered from sediments apparently transported downslope as turbidites or other mass flows and deposited as graded units. The coarser sands contain sorted assemblages of large specimens, whereas the finer parts of the graded beds host mainly small juvenile forms, many of which are difficult to classify. Planktonic foraminiferal analysis was based mainly on core-catcher samples, which, depending on lithology, contain microfaunas of varying composition, abundance, and preservation.

Samples 134-827A-1H-CC through -15X-CC, 134-827B-1R-CC, and 134-827B-2R-CC contain *Globorotalia truncatulinoides,* which suggests that the upper 127.2 m of sediment is of Holocene and Pleistocene age (Fig. 13). The boundary between the Pleistocene and Pliocene is drawn at 127.2 m, based on the co-occurrence of *Globorotalia tosaensis* and *G. truncatulinoides*. Such a boundary, however, is approximate as the first appearance datum (FAD) of *G. truncatulinoides* is a diachronous event that ranges from 1.9 to 2.7 Ma according to latitude (Hills and Thierstein, 1989). The late Pliocene is represented in the interval between 127.2 and 252.6 mbsf (Samples 134-827B-3R-CC to -15R-CC). The boundary is defined by the presence of *G. tosaensis,* and absence of *G. truncatulinoides*. All the other samples were barren unless otherwise stated.

The Holocene to late Pliocene assemblages are characterized in general by the occurrence of *Orbulina universa, Globigerinita glutinata, Globigerinoides ruber, Globigerinoides conglobatus,*

Globigerina rubescens, Globigerinella calida, Globorotalia tumida, Globorotalia menardii, Globorotalia crassula, Globorotalia crassaformis, Globorotalia inflata, Neogloboquadrina dutertrei, and *Pulleniatina obliquiloculata.*

Evidence of reworking is apparent in most of the studied samples. Reworking is indicated in the Pleistocene Samples 134-827B-7R-CC to -14R-CC, which show few to common reworked specimens of Pliocene to late Miocene species *Sphaeroidinella paenedehiscens, Pulleniatina praecursor, Dentoglobigerina altispira altispira,* and *Sphaeroidinellopsis kochi.* Samples 134-827B-11R-CC and -14R-CC of late Pliocene age contain the middle Eocene species, *Acarinina bullbrooki, A. broedermani, Globigerinateka* spp., and *Truncorotaloides rohri.* Reworking is particularly evident in Sample 134-827B-11R-CC, which is composed of cream-white friable mudstone clasts in a grayish green mudstone. The sample yields abundant middle Eocene planktonic foraminifers, radiolarians, and sponge spicules.

A calcareous sandstone pebble in Section 134-827B-25R-1 contained the larger foraminiferal species *Lepidocyclina* sp., and the presence of *Miogypsina* sp. in Sample 134-827B-24-CC indicates reworking from early Miocene (larger foraminifer T-letter stage, Tf1). An abnormal condition in the water column is suggested to explain the unusual small-sized (juvenile forms) foraminiferal assemblage recorded in Samples 134-827A-8H-CC and 134-827A-9H-CC.

Benthic Foraminifers

Rare to common benthic foraminifers generally occur in core-catcher samples examined from Site 827, except for Section 134-827B-14R-CC and below Section 134-827B-16R-CC. The preservation of benthic foraminiferal tests is generally moderate to good. The characteristic species throughout the stratigraphic interval examined are *Bolivinita quadrilatera, Globobulimina pupoides, Melonis pacificus, Melonis sphaeroides, Rutherfordoides mexicanus, Bulimina marginata, Bulimina striata, Stilostomella lepidula, Uvigerina hispidocostata,* and *Valvulineria* sp.

Neogene strata at Site 827 may be divided biostratigraphically into six assemblage zones (Fig. 13) based on the occurrence of benthic foraminiferal species. Assemblage Zone I encompasses Samples 134-827A-1H-CC through 134-827A-5H-CC and is marked by the abundant occurrence of *Globobulimina pupoides* and *Bolivinita quadrilatera.* The abundances of *G. pupoides* and *B. quadrilatera* decrease in the lower part of this assemblage zone.

Assemblage Zone II is characterized by the co-occurrence of *B. marginata, B. striata,* and *R. mexicanus* in samples ranging from 134-827A-6H-CC to 134-827A-9H-CC. Assemblage Zone III covers the Samples 134-827A-10H-CC to 134-827A-13H-CC, characterized by the co-occurrence of *Globobulimina pupoides* and *Uvigerina hispidocostata.* Assemblage Zone IV is recognized in the interval between Samples 134-827A-14X-CC and 134-827B-4R-CC. The base of this zone is defined by a rapid increase in the abundance of *Valvulineria* sp. In this zone the deep-water species such as *Cibicides wuellerstorfi, Melonis barleeanus,* and *Oridorsalis tener* also occur.

Assemblage Zone V corresponds to an interval from the last occurrence of *Melonis sphaeroides* (Sample 134-827B-7R-CC) to the base of the rapid increase in abundance of *Valvulineria* sp. (Sample 134-827B-5R-CC). *Stilostomella lepidula* is also abundant in this zone.

Assemblage Zone VI is characterized by the occurrence of *Melonis pacificus* and *Melonis sphaeroides* in the interval between Samples 134-827B-8R-CC and 134-827B-15R-CC, although neither was observed in Sample 134-827B-14R-CC. Other deep-water (>2000 m) species such as *Glomospira goldialis* and *Nodosaria longiscata* are present. The paleobathymetric evaluation of the succession is as follows: (1) sediments from Cores 134-827A-1H to 134-827B-7R were deposited in the middle bathyal zone (500–2000 m), (2) the upper 44.9 mbsf of Hole 827A were deposited under conditions of low oxygen, and (3) sediments from Cores 134-827B-8R to -15R were deposited in the lower bathyal zone (2000–3000 m).

Akimoto et al. (1991) found that anomalous chemical conditions around and within *Calyptogena* colonies associated with cold seeps high in methane are detectable by the rich occurrences of both *Bulimina striata* and *Rutherfordoides* sp. A. They also found that the faunal change in benthic foraminifers, which is reflected by the occurrence of *Rutherfordoides* sp. A., is well correlated with the change in methane concentration. Thus, Akimoto et al. (1991) concluded that abnormal bottom-water conditions and related species composition of benthic foraminifers are formed as a result of methane seeping out of the seafloor. In Hole 827B both *Bulimina striata* and *Rutherfordoides mexicanus* were identified. *Bulimina striata* was found at a depth of 243 mbsf, near a reported thrust fault (see "Lithostratigraphy" section, this chapter), but no methane was reported at this depth. However, *Rutherfordoides mexicanus* was found between 53 and 74 mbsf, near the depth (~75 mbsf) where methane was detected ("Sediment and Fluid Geochemistry" section, this chapter). Therefore, we speculate that these benthic foraminifers may be indicating the presence of methane in the sediments at the time of deposition; however, more analyses need to be made to determine how rich these communities are and if they can, indeed, be used here as indicators of methane concentrations.

Summary

A summary of the biostratigraphic results for Holes 827A and 827B is presented in Figure 13. In Hole 827A, the core-catcher samples from Cores 134-827A-1H through -15X are Pleistocene. Core-catcher samples from Cores 134-827B-1R and -2R are Pleistocene, those from Cores 134-827B-3R through -16R are either Pleistocene or late Pliocene in age, and those from Cores 134-827B-17R through -31R are of indeterminate age.

Reworked early Pliocene and Miocene microfossils were encountered throughout the sequence. Reworking of middle Eocene microfossils is evident in Sample 827B-11R-CC of Pleistocene or late Pliocene age. The sediments in Cores 134-827A-1H to 134-827B-7R were deposited in the middle bathyal zone (500–2000 m) and the upper 44.9 mbsf of Hole 827A was deposited under conditions of low oxygen at the sediment-water interface. The sediments in Cores 134-827B-8R and -15R were deposited in the lower bathyal zone (2000–3000 m).

SEDIMENT AND FLUID GEOCHEMISTRY

The pore-fluid chemistry was measured (see "Explanatory Notes" section, this volume) in order to (1) estimate diagenetic sources for solutes and (2) observe the chemistry of fluids that may have originated from subduction-related processes. In convergent margin sediments, diagenesis directly alters the physical properties of the sediments and fluid circulation can lubricate faults, limiting deformation. During deformation at convergent margins, pore fluid flows from the sediments, and depending on its composition may be an important solute source in global geochemical cycles (e.g., Han and Suess, 1989; Martin et al., in press).

Table 3. Sediment contents: total carbon, carbonate, and inorganic and organic carbon, Site 827.

Core, section, interval (cm)	Depth (mbsf)	Total carbon (wt%)	Inorganic carbon (wt%)	Organic carbon (wt%)	$CaCO_3$ (wt%)
134-827A-					
1H-2, 37–40	1.9	1.9	1.38	0.48	11.5
1H-3, 37–40	3.4	1.3	0.77	0.48	6.4
1H-5, 37–40	6.4	1.4	0.95	0.42	7.9
2H-4, 48–50	14.8	1.6	1.23	0.41	10.2
2H-6, 135–138	18.7	1.8	1.33	0.45	11.1
3H-1, 37–40	19.7	1.5	1.02	0.48	8.5
3H-3, 37–40	22.7	1.6	1.19	0.40	9.9
3H-7, 37–40	28.7	1.8	1.31	0.50	10.9
4H-1, 37–40	29.2	2.1	1.57	0.50	13.1
4H-3, 37–40	32.2	1.6	1.14	0.47	9.5
4H-5, 37–40	35.2	1.9	1.33	0.54	11.1
5H-3, 37–40	39.9	1.7	1.20	0.52	10.0
5H-5, 37–40	42.9		1.15		9.6
5H-5, 37–40	42.9		1.37		11.4
6H-1, 37–40	45.3	0.8	0.53	0.28	4.4
6H-3, 37–40	48.3	1.4	1.02	0.40	8.5
6H-4, 127–130	50.7	1.2	0.88	0.34	7.3
6H-5, 37–40	51.3	1.6	1.16	0.45	9.7
7H-1, 37–40	53.2	1.7	1.15	0.53	9.6
7H-3, 37–40	56.2		1.01		8.4
7H-5, 36–40	59.2		1.07		8.9
7H-5, 120–123	60.0	1.4	0.89	0.47	7.4
8H-1, 37–40	61.4	1.7	1.10	0.57	9.2
8H-3, 37–40	64.4	1.8	1.21	0.61	10.1
9H-2, 37–40	68.9	1.5	1.15	0.31	9.6
9H-4, 37–40	71.9		1.06		8.8
10H-1, 130–133	73.8	1.7	1.25	0.48	10.4
10H-4, 40–43	77.4	1.1	0.89	0.25	7.4
11H-1, 75–78	78.4		1.1		9.2
11H-2, 73–76	79.8	1.8	1.16	0.64	9.7
11H-4, 41–44	82.5		0.99		8.2
12H-1, 43–46	83.6		0.94		7.8
12H-1, 125–127	84.5		1.5		12.5
12H-2, 30–33	85.0	1.6	1.17	0.46	9.7
13H-1, 40–44	88.2	1.8	1.16	0.59	9.7
13H-3, 41–44	91.2		1.16		9.7
14X-1, 77–81	92.3	1.8	1.34	0.49	11.2
15X-1, 67–70	101.7		1.45		12.1
15X-3, 67–70	104.7		2.15		17.9

The carbon data are given in Table 3. The carbonate content is plotted against depth in the "Lithostratigraphy" section of this chapter and the organic carbon is plotted vs. depth in Figure 14.

Methods and Sample Handling

A total of 10 whole-round fluid samples were collected from the first and third cores and then from every third core until igneous rocks were encountered. At Hole 827A, three samples were obtained from sediments drilled with the advanced piston core (APC) and two from sediments drilled with the extended core barrel (XCB). The remaining five samples were collected from sediments drilled with the rotary core barrel (RCB) at Hole 827B. The APC and XCB samples showed little drilling disturbance and thus were probably not contaminated by the drilling fluid (surface seawater). The RCB samples, however, were highly fractured and the fracture faces were covered with fluid that was assumed to be drilling fluid. This contaminant and several millimeters of sediment below the fracture face were scraped from the samples before squeezing.

Because of changes in lithology and consolidation of the sediment, the yield of water from each sample dropped rapidly with depth (Fig. 15) and thus the length of sample taken from the cores was increased as the samples became more consolidated. The lengths ranged from 5 cm for the shallow samples up to 35 cm in the deepest samples.

Table 3 (continued).

Core, section, interval (cm)	Depth (mbsf)	Total carbon (wt%)	Inorganic carbon (wt%)	Organic carbon (wt%)	$CaCO_3$ (wt%)
134-827B-					
1R-4, 47–50	115.6		1.47		12.2
2R-2, 35–38	119.5		1.97		16.4
2R-4, 130–133	123.4		2.32		19.3
2R-6, 20–25	125.3		2.08		17.3
3R-1, 10–14	127.3		2.02		16.8
3R-3, 135–138	131.6		1.92		16.0
3R-5, 135–137	134.6		1.86		15.5
3R-7, 20–22	136.4		1.95		16.2
4R-1, 97–100	137.9		2.83		23.6
4R-3, 97–100	140.9		2.82		23.5
4R-6, 97–100	145.4		2.83		23.6
5R-1, 145–148	148.0		2.42		20.2
5R-3, 80–83	150.3		4.2		35.0
5R-5, 27–30	152.8		2.88		24.0
6R-1, 140–143	157.6		1.62		13.5
6R-3, 140–143	160.6	0.8	0.68	0.16	5.7
6R-4, 132–135	162.0		2.33		19.4
7R-2, 140–143	168.7		0.15		1.2
7R-3, 137–140	170.2		2.93		24.4
7R-4, 137–140	171.7	3.0	2.61	0.39	21.7
8R-1, 142–145	176.8	4.2	3.64	0.55	30.3
8R-3, 62–65	179.0		2.6		21.7
8R-5, 65–65	182.0		2.61		21.7
9R-1, 37–40	185.5		2.98		24.8
9R-3, 37–40	188.5	3.5	3.00	0.54	25.0
9R-5, 37–40	191.5		2.53		21.1
10R-1, 37–40	195.1		2.97		24.7
10R-3, 37–40	198.1	2.4	1.95	0.48	16.2
10R-5, 37–40	201.1		3.76		31.3
11R-3, 38–41	207.8	4.2	3.71	0.50	30.9
12R-1, 64–66	214.6		3.66		30.5
12R-3, 39–42	217.4	2.7	2.31	0.40	19.2
13R-1, 45–47	224.2	5.6	5.09	0.46	42.4
13R-3, 45–47	227.2		4.28		35.7
13R-5, 41–44	230.1		5.23		43.6
13R-6, 105–107	232.3		1.8		15.0
14R-1, 19–22	233.5		0.06		0.5
14R-2, 89–92	235.7		0.2		1.7
14R-3, 11–12	236.4		1.34		11.2
15R-1, 15–18	244.2	1.3	1.09	0.21	9.1
15R-3, 11–14	246.1		5.36		44.6
15R-6, 6–6	250.6		1.32		11.0
16R-1, 10–12	252.7		4.79		39.9
16R-1, 37–41	253.0		0.84		7.0
17R-CC, 0–3	262.3	1.1	1.04	0.10	8.7
19R-CC, 22–25	281.9	0.3	0.10	0.15	0.8
22R-1, 37–40	311.0	1.5	1.31	0.18	10.9
30R-1, 37–40	384.6	4.0	3.46	0.54	28.8

Results

The shipboard measurements of pore-fluid solute concentrations are shown in Table 4. The concentrations are plotted against depth in Fig. 16.

Chlorinity and Salinity

Because chloride is usually conservative, its concentration in open-ocean drill sites rarely changes with depth. At Site 827, however, both chloride concentration and the salinity increase steeply with depth (Fig. 16). The maximum chloride concentration is ~14% greater than seawater at only ~175 mbsf. The cause of this high chloride concentration is unknown; other convergent margin pore fluids are usually characterized by chloride concentrations less than seawater values (Gieskes et al., 1990a; Kastner et al., 1990; Mottl et al., in press). At least two processes may increase chloride concentrations: (1) hydration of basement rocks and sedimentary minerals, particularly volcanic ash, and (2) ion exclusion as water flows through semipermeable clay

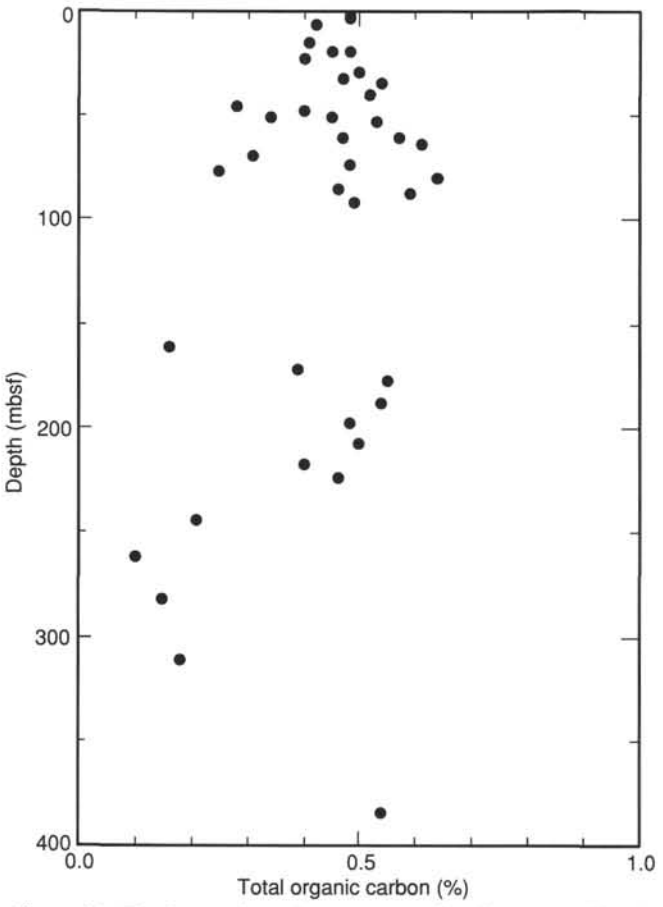

Figure 14. Total organic carbon content of sediments at Site 827 plotted vs. depth.

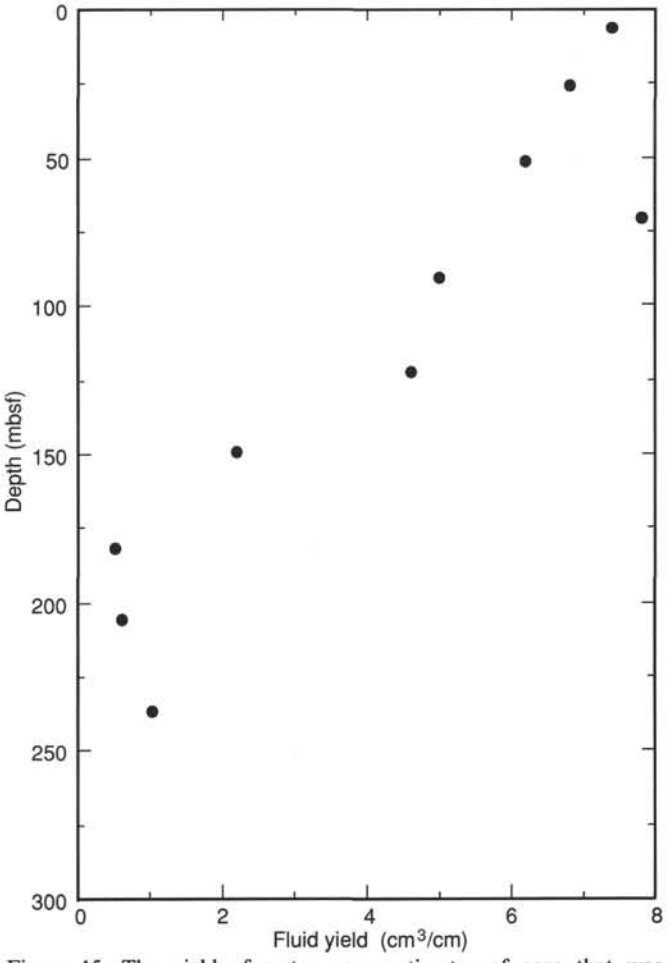

Figure 15. The yield of water per centimeter of core that was squeezed, Site 827. This value is only a qualitative measure of the water contained in the sediment because some variable amount of the sample was removed from each sample prior to squeezing.

membranes under extreme pressures (Hanshaw and Coplen, 1973; Kharaka and Berry, 1973; Graf, 1982). During this process of membrane filtration, solutes are selectively retained on the high-pressure side of the semipermeable clay membrane as water preferentially moves through the membrane. At Site 827, however, the other solute concentrations also reflect strong diagenesis and suggest that the first process may be dominant.

Sodium and Potassium

The sodium concentrations were measured using atomic emission spectroscopy and were also calculated based on a charge balance of the major solute concentrations. A plot of these two values (Fig. 17) shows good agreement of the results for these two techniques.

Both sodium and potassium concentrations exhibit shallow subsurface minima and deeper maxima (Fig. 16). Below the maxima, the concentrations of both elements decrease with depth, suggesting that the volcanic rocks in Unit III (see "Lithostratigraphy" section, this chapter) may be a sink for these constituents. The sodium maximum occurs at a depth of ~75 mbsf, but the potassium maximum occurs slightly deeper

Table 4. Pore-fluid chemistry, Site 827.

Core, section, interval (cm)	Depth (mbsf)	pH	Salinity (‰)	Sodium (mM)	Chloride (mM)	Potassium (mM)	Magnesium (mM)	Calcium (mM)	Sulfate (mM)	Alkalinity (mM)	Phosphate (μM)	Ammonia (μM)	Silica (μM)
134-827A-													
1H-4, 145–150	6.0	7.9	38.5	488	560.6	11.8	60.9	11.7	30.5	18.2	3.3	789	349
3H-4, 145–150	25.3	7.8	36.0	468	580.3	10.3	71.7	9.8	24.1	15.0	6.6	1441	298
6H-4, 145–150	50.9	8.0	35.0	455	598.1	11.4	66.0	7.0	0.0	23.6	18.2	1925	352
9H-2, 145–150	70.0	7.9	35.5	474	596.1	10.6	59.4	10.3	0.0	18.7	7.1	1839	543
13H-2, 135–140	90.8	8.1	35.0	475	600.1	13.2	41.0	21.4	1.0	2.3	1.9	1337	356
134-827B-													
2R-3, 145–150	122.1	8.0	38.5	434	604.0	12.9	36.7	49.6	5.7		1.3	1400	459
5R-2, 140–150	149.5	7.3	38.0	359	613.9	12.5	29.2	99.4	6.7	0.4	0.6	835	511
8R-4, 140–150	181.4		40.0	277	627.7	10.9	13.2	157.0	3.3			691	453
11R-1, 135–150	205.9	6.8	40.0	248	621.8	9.0	9.3	175.8	3.2	0.1		841	356
14R-2, 0–30	236.3	8.3	40.0	253	606.0	6.3	9.8	172.3	8.7	0.5	0.6	454	270

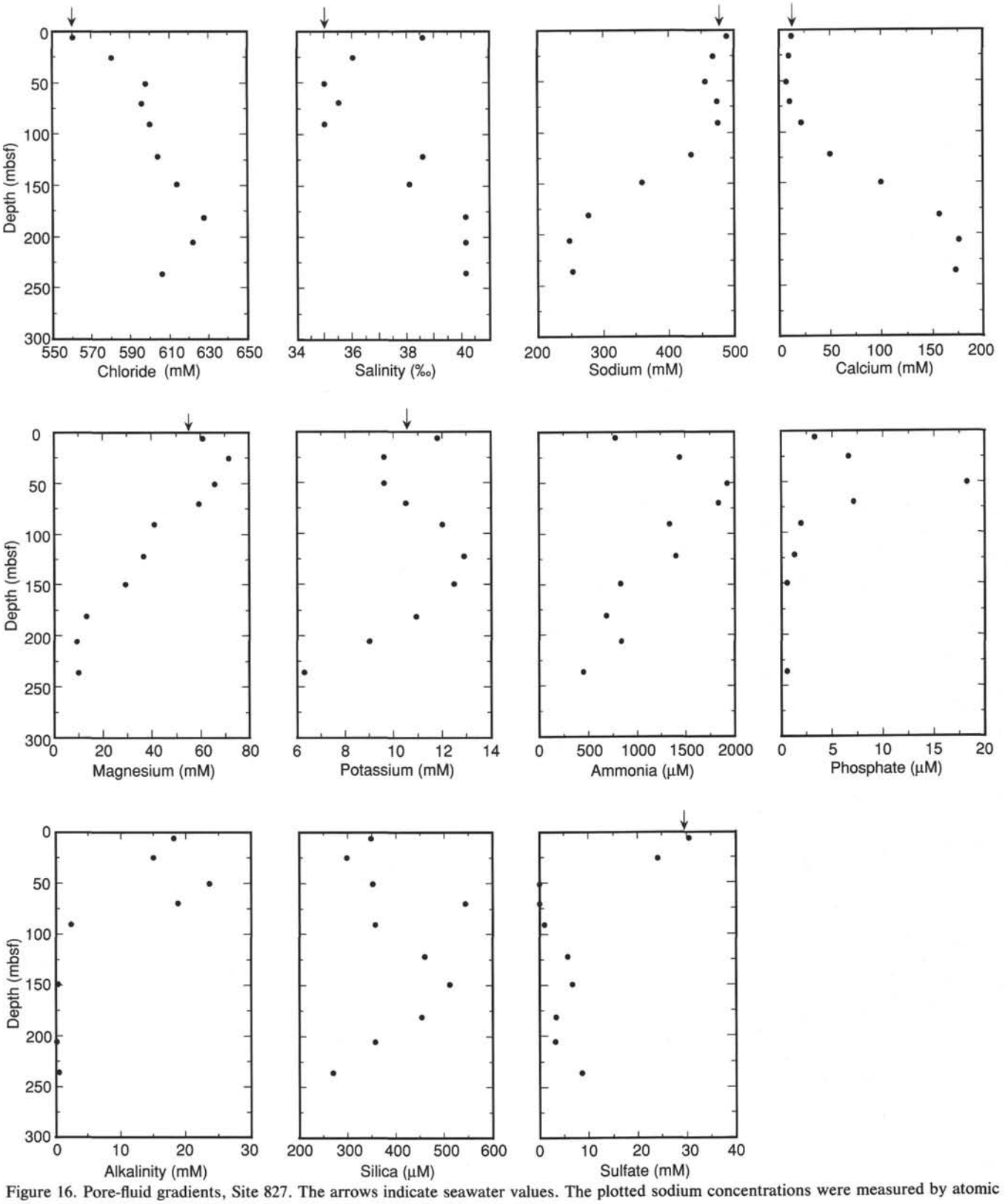

Figure 16. Pore-fluid gradients, Site 827. The arrows indicate seawater values. The plotted sodium concentrations were measured by atomic emission spectroscopy.

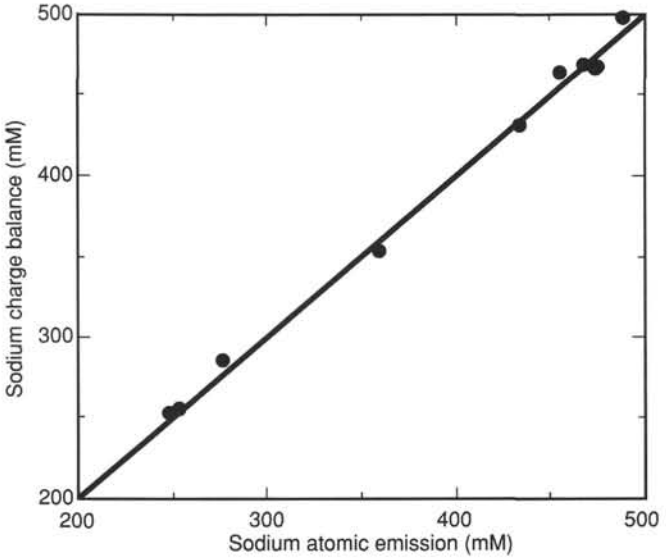

Figure 17. The concentration of sodium measured by atomic emission spectroscopy vs. an estimate of sodium concentrations from charge-balance calculations.

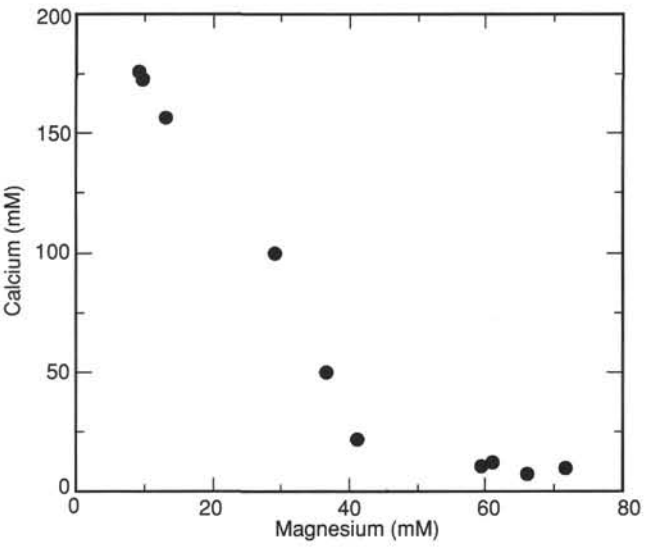

Figure 18. The calcium concentrations vs. the magnesium concentrations.

at a depth of ~125 mbsf. These maxima may reflect a local diagenetic source, however, the lithology throughout these depth intervals is homogeneous (see "Lithostratigraphy" section, this chapter). The maxima may thus reflect lateral flow of a sodium- and potassium-rich fluid, although the depth discrepancy prevents the identification of a particular zone of fluid flow.

Calcium and Magnesium

Both calcium and magnesium concentrations display steep depth gradients between ~50 and 175 mbsf, but their concentrations are constant at depths below ~175 mbsf (Fig. 16). The magnesium concentration reach values of 9.0 mM at 206 mbsf and the calcium concentrations reaches an extraordinarily high value of 175.8 mM (~17× seawater concentrations) by the same depth. These concentrations are strongly and inversely correlated in the deeper pore fluids (Fig. 18), suggesting that they are controlled by the same processes. Calcium-magnesium correlations also occur in pore fluid from the Barbados accretionary wedge (Gieskes et al., 1990b) and probably reflect alteration of volcanic rocks (McDuff and Gieskes, 1976; McDuff, 1981). The constant concentrations in the deepest samples may reflect the end-member composition of fluids that have undergone the maximum alteration of the fluid chemistry.

Ammonia, Phosphate, Alkalinity, Silica, Sulfate, and Methane

Ammonia, phosphate, and alkalinity display shallow maxima at ~50 mbsf, but the overall concentrations are low, reflecting the low organic carbon content in the sediments (Fig. 14). The silica concentrations display a minimum value at ~25 mbsf and a sharp, one-point maximum at ~75 mbsf. This maximum is probably not an artifact of measurement or sampling because repeated measurements of this sample yielded similar results, and the peak corresponds to anomalies in other solute concentrations.

Sulfate reduction is complete by 50 mbsf (Fig. 16). Below this depth, however, the pore fluids contain significant sulfate concentrations, up to ~7.5 mM in the deepest sample. This sulfate is probably not contamination from drill water because of the care taken in handling the samples and because of other solute concentrations do not appear contaminated. The presence of sulfate below the base of the sulfate reduction zone implies a deep, unknown source for the sulfate. Increases in sulfate concentrations occur in sediments of other subduction zones, particularly below the décollement at the Nankai Trough (Taira, Hill, Firth, et al., 1991) and in serpentinite diapirs in the Mariana forearc (Mottl, in press).

The headspace samples exhibit little methane except at ~75 mbsf, where the concentrations exhibit a sharp maximum of nearly 30,000 ppm (Fig. 19). High methane concentrations apparently characterize fluids in subduction zones; methane concentrations greater than the surrounding pore fluids occur in the décollement at Barbados (Gieskes et al., 1990b) and methane is present in the serpentinite diapirs in the Mariana forearc (Mottl, in press). At Site 827, the methane does not correspond to a change in lithology or to the maxima in phosphate, alkalinity, or ammonia, and the organic carbon content of the sediments increases only slightly (Fig. 14). The maximum does correspond to the base of sulfate reduction and may reflect the onset of methanogenesis.

Summary

1. The increase in chloride concentration with depth may result from hydration reactions with the igneous rocks at the base of this site. An alternative hypothesis is that the pore-fluid chemistry has been altered through ion exclusion processes as it flows through semipermeable clay membranes.

2. The strong depth gradients displayed by the sodium, potassium, calcium, and magnesium concentrations probably result from exchange reactions with the igneous rocks. These gradients may also be affected by alteration of ash within the sediments but the profiles suggest that diffusion from the Unit III volcanic rocks overwhelms localized sedimentary glass alteration.

3. The sediments are characterized by low organic carbon content, and organic matter diagenesis causes only minor increases in the alkalinity and ammonia and phosphate concentrations. Each of the solutes displays sharp subsurface maxima at ~50 mbsf. Regardless of the low organic carbon concentrations, sulfate reduction appears to be complete by

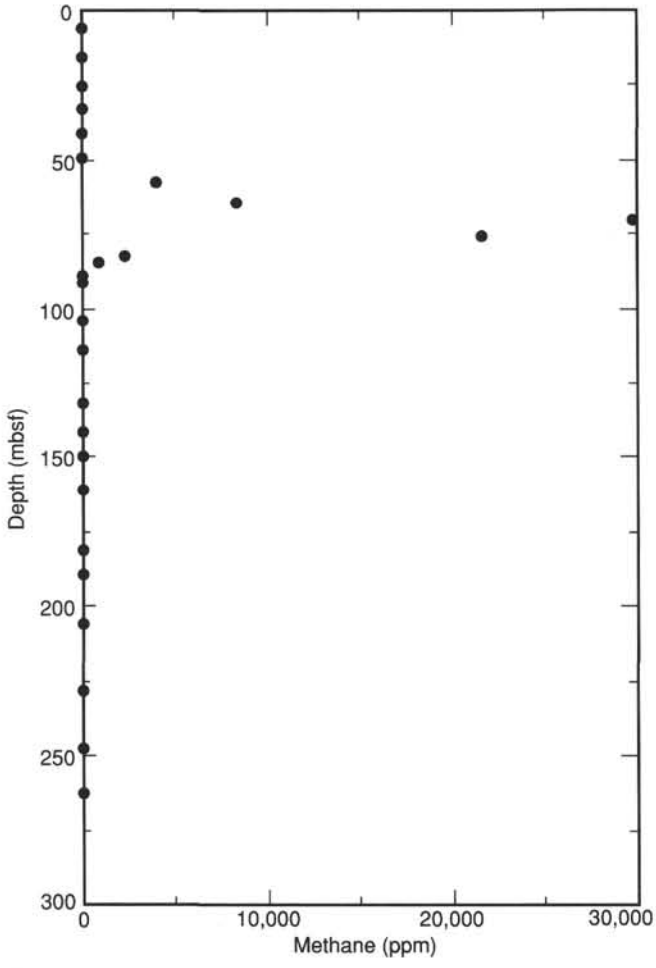

Figure 19. The concentration of methane in the headspace analyses plotted vs. depth.

50 mbsf. Sulfate is again present below 90 mbsf, indicating the presence of a deep source for sulfate.

4. The most surprising result is indicated in the chemistry observed at a depth of ~75 mbsf. The variations in chemistry at this depth are subtle but indicate that fluid is present with a composition similar to fluids from other forearc regions, in particular at Barbados (Gieskes et al., 1990b), Nankai (Taira, Hill, Firth, et al., 1991), and in serpentinite diapers in the Mariana forearc (Mottl, in press). These chemical signals include high methane concentration, low chloride concentration, high silica concentration, and an increase in sulfate concentration. These fluids possibly were altered at depth and flowed upwards through the sediments. No faulting or permeable layers were observed at this horizon, however, and thus the path of the fluids is not known.

STRUCTURAL STUDIES

Structural data observed in sediments cored from 0 to 253 mbsf at Site 827 are reported in Figure 20. Below 253 mbsf, the recovery was extremely poor.

Attitudes of bedding planes downhole are poorly constrained except in Hole 827A, where a Pleistocene turbiditic sequence was drilled from 0 to 90 mbsf. Bedding attitudes in this turbiditic sequence are horizontal to subhorizontal. Bedding surfaces are only visible in a few places in Hole 827B (Fig. 20). Lithostratigraphic Units II and III (see "Lithostratigraphy" section, this chapter) consist of structureless volcanic silt and sed-lithic matrix-supported conglomerate. Slump structures were observed and are best exposed in Section 134-827A-9H-3, 25–85 cm, and in Section 134-827B-12R-1, 20–90 cm.

The first appearance of tectonic deformation occurs in Section 134-827A-15X-4 at 107 mbsf and more obviously in Section 134-827B-2R-1 at 118 mbsf, the latter with small-scale faults dipping about 30°–35°. Paleomagnetic orientation of the structures was not possible because of drilling disturbance. The amount of deformation increases downhole below 140 mbsf (Fig. 20). Three zones of major deformation with scaly cleavage fabrics and intense mesoscopic faulting were encountered in Hole 827B (labeled I, II, and III in Fig. 20). The uppermost zone of scaly cleavage fabric occurs at Section 134-827B-6R-3, 0–50 cm (159 mbsf) with a total thickness of 50 cm. The second zone, between 180 and 200 mbsf, is much thicker and comprises several distinct horizons of scaly fabrics. The largest horizon is about 1 m thick and occurs at 195 mbsf in Core 134-827B-10R. Material between the scaly fabric horizons displays intense brittle deformation. Wherever the sense of motion could be identified, the faults have reverse displacements. The third zone of tectonic disturbance, located between 230 and 250 mbsf, is interpreted as the major shear zone of Hole 827B because it displays the most intense deformation. This zone is composed of several 1-m-thick horizons of scaly silt. Figure 21 illustrates the best exposure of scaly cleavage fabric that occurs at 243 mbsf. The dominant attitude of the scaly foliation observed in these three zones is at a high angle to the core axis; dips range generally from 60° to 80°. We observed that levels of partially lithified conglomerates in lithostratigraphic Unit III are affected primarily by brittle deformation (Fig. 22).

From 252 msbf to the base of Hole 827B at 400.4 mbsf, the recovery was generally insufficient to determine tectonic elements. However, small isolated clasts of strongly indurated volcanic siltstone and sandstone recovered in the cores exhibit numerous microfaults filled with calcite. In Section 134-827B-30R-1 at 385 mbsf a 0.5-m-thick horizon of scaly cleavage fabric was encountered. All these features suggest that the rocks of the lower part of Hole 827B have been subjected to tectonic deformation.

The three major zones of deformation in Hole 827B between 150 and 250 mbsf are tentatively interpreted as reverse or thrust fault zones on the basis of observed structures (Fig. 20). However, the hypothesis that these are thrusts is not documented by preliminary paleontological results, which do not indicate inversion in age downhole. If the paleontological ages are correct, these thrusts could be intraformational.

PALEOMAGNETISM

All archives halves from APC and XCB cores from Hole 827A were measured with the cryogenic magnetometer. Archive halves of RCB cores from Hole 827B (Cores 134-827B-16R through -31R) were also measured, although we noticed that the rotary drilling process had clearly disturbed the soft sediments. Natural remanent magnetization (NRM) was measured at 10-cm intervals and the remanence remaining after alternating field (AF) demagnetization was measured at 5-cm intervals. The peak field intensities of AF demagnetization ranged from 5 to 15 mT. Sixty-three discrete samples were measured by the spinner magnetometer and stepwise AF demagnetizations were performed by the Schonstedt demagnetizer until a stable component of the remanence was isolated in order to check the reliability of the measurements from the archive halves.

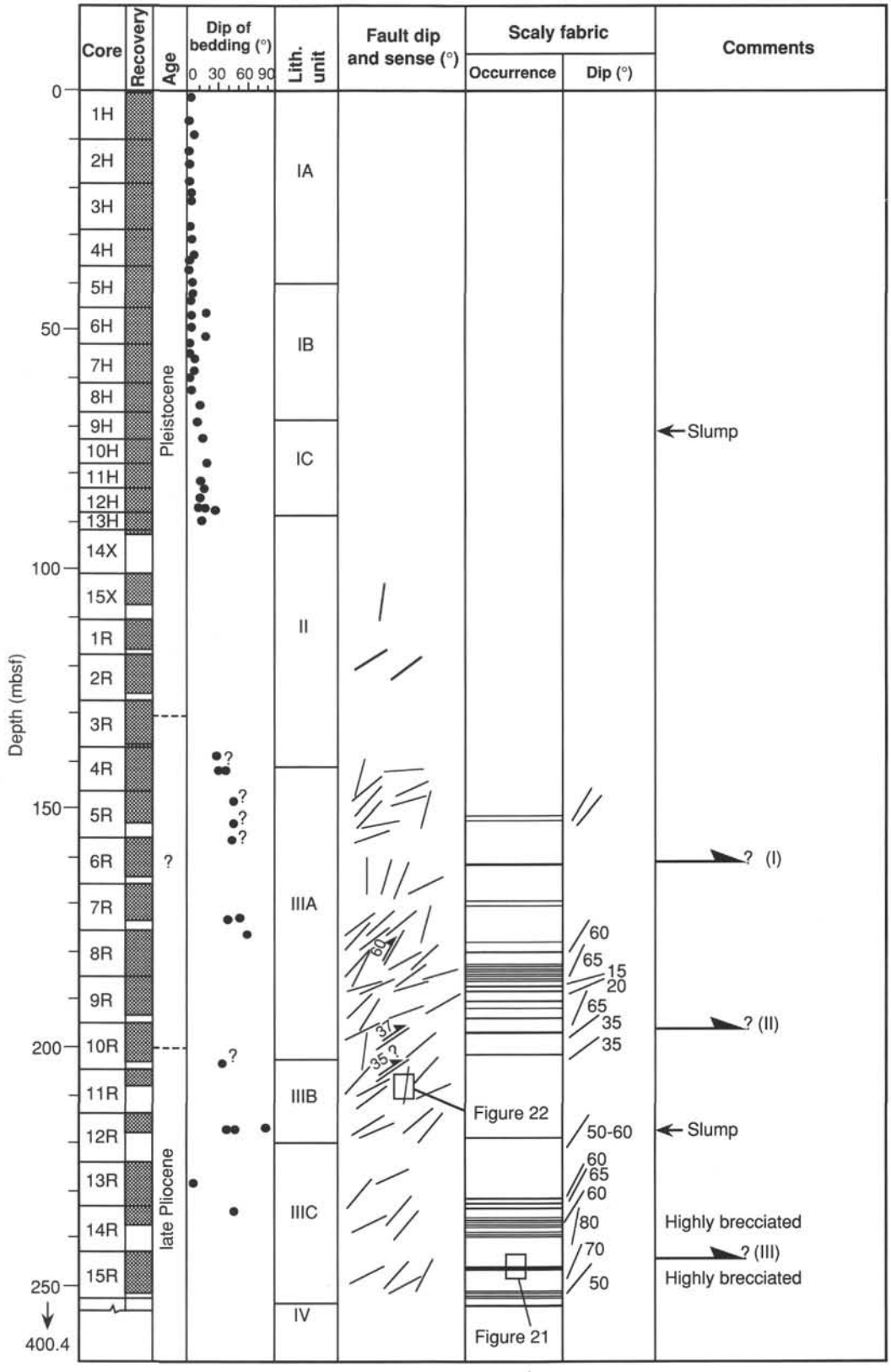

Figure 20. Summary of structural features from Holes 827A and 827B. The lower part of the Hole 827B is not shown because of poor recovery. Dips of bedding and faults, and distribution of zones of scaly fabrics, are shown. Faults are indicated by short lines. Numbers near the lines or angle of the lines with the horizontal indicate dip of faults. Arrows indicate sense of displacement. An increase in the amount of faulting is reflected by an increase in the number of short lines in the illustration. Assumed thrust planes are marked by a bold half-arrow.

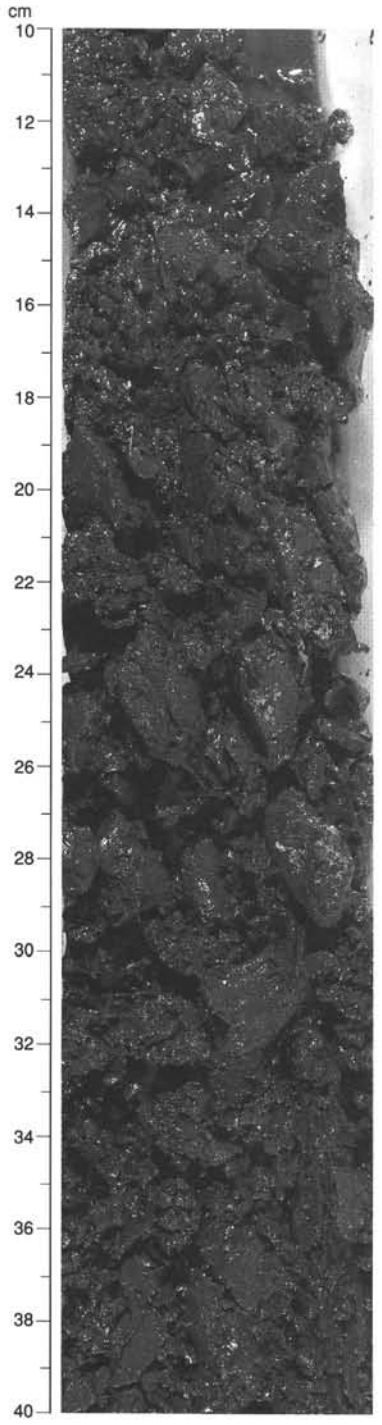

Figure 21. Steeply dipping scaly fabrics in Section 134-827B-15R-1. Location is shown in Figure 20.

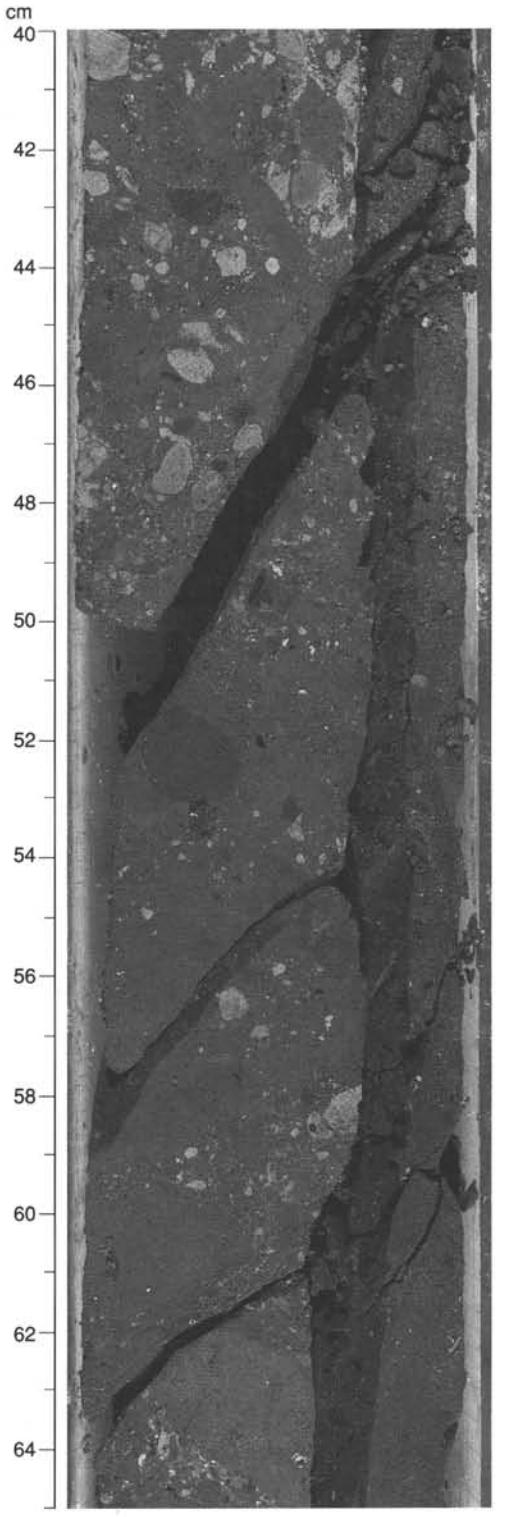

Figure 22. Brittle deformation in the conglomeratic rock level (Subunit IIIB) of lithostratigraphic Unit III, Section 134-827B-11R-2. Location is shown in Figure 20.

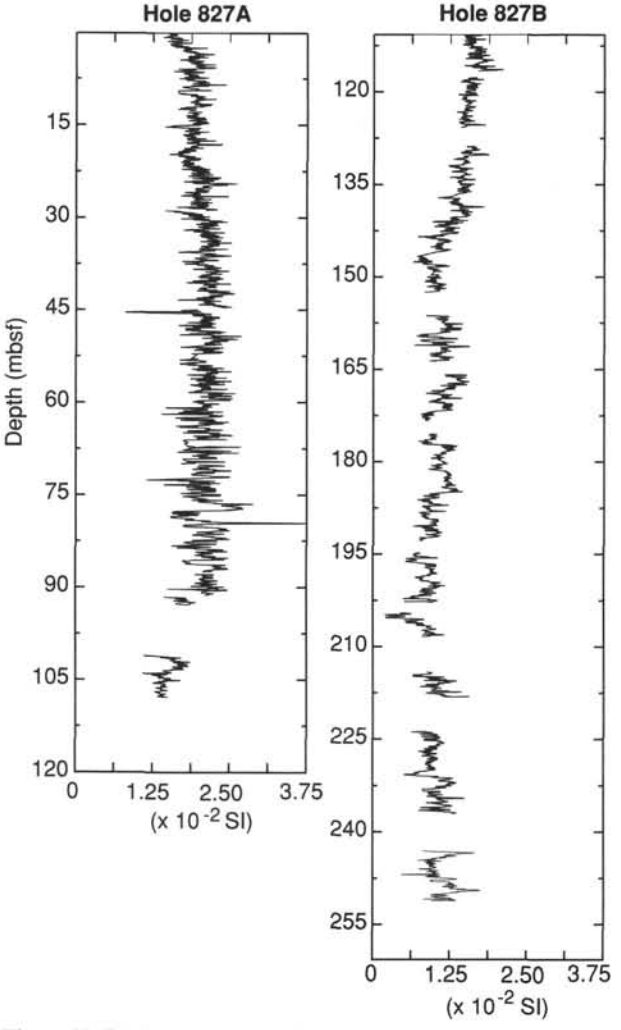

Figure 23. Variation of magnetic susceptibility as a function of depth in Holes 827A and 827B.

Magnetic Properties

Hole 827A contains a sequence of turbiditic siltstone rich in volcanic particles; magnetic susceptibility of the siltstone is quite high (about 2.0×10^{-2} SI units) (Fig. 23). The magnetic susceptibility decreases downhole in Hole 827B to about 1.0×10^{-2} SI. However, these data are from material recovered by rotary coring; no correction for the exact volume of each section was made.

The NRM intensity from the archive halves was too strong for measurement with the cryogenic magnetometer; values greater than 1 A/m are not considered accurate (Fig. 24). The NRM directions have very steep negative inclinations, although the inclination shallowed toward that expected at this site (–29°) during AF demagnetization (Fig. 24). The intensity of magnetization after demagnetization to 10 mT is about 10% of the NRM value, which reflects consistent, strong drilling-induced overprint (see "Explanatory Notes" chapter, this volume). Discrete samples taken from the center of the working half were less overprinted and provided more accurate results (Fig. 25), although the coercivities of most samples were low, as evidenced by low median destructive fields (MDF) (Fig. 26). The mean inclination (–33°) of 29 samples after AF demagnetization to 20 mT is consistent with the inclination expected at this site.

Magnetostratigraphy

The characteristic magnetization observed in Hole 827A is of normal polarity. The excursions previously reported in the Brunhes Chron (see Champion et al., 1988, for an updated review) were not observed at this site.

The inclination in Hole 827B is dominantly negative (normal polarity); the only evidence for a possible reversed chron or subchron occurred at the bottom of Core 134-827B-9R (Fig. 27) and at the top of Core 134-827B-10R (188.5–197.0 mbsf). The rocks are sheared and were broken apart by drilling. Thus, the declination is not stable, but there is evidence for positive inclination down Core 134-827B-9R that was confirmed by progressive demagnetization of discrete specimens (Fig. 28). Because we have very poor control of the bedding attitude in these cores, it is difficult to produce a clear magnetic polarity stratigraphy for Hole 827B.

In conclusion, paleomagnetic studies at Site 827 indicate that the sediments contain a large amount of magnetic material and that most sediments from Hole 827A were deposited rapidly during the Brunhes Chron. The low stability of the magnetization may result from the redeposition of large grains of magnetite after erosion of the nearby New Hebrides Island Arc. Because of the low magnetic stability, a strong overprint was imparted to the cores during drilling.

SEDIMENT ACCUMULATION RATES

Sedimentation rates for Site 827 are estimated from calcareous nannofossil datums, which are used to construct an age-vs.-depth curve as shown in Figure 29. Error bars indicate the degree of uncertainty as to the precise location of the age datums within a particular core.

The highest sedimentation rates, 344 m/m.y., have been recorded from within graded sediments of lithostratigraphic Unit I (see "Lithostratigraphy" section, this chapter), representing the time interval from the latest Pleistocene (0.28 Ma) to the Holocene. Sediment-accumulation rates decrease downcore with an estimated rate of 65 m/m.y. over the time interval from the late Pleistocene (0.28 Ma) to the latest middle Pleistocene (1.57 Ma). Sediment accumulation rates once again increase to 214 m/m.y. in the time interval 1.57 Ma to 1.66 Ma. Because the interval of time represented is small relative to the length of the error bar, the estimated sediment accumulation rate is uncertain.

PHYSICAL PROPERTIES

Measurements of index properties and Hamilton Frame sonic velocities were completed on sediments and rocks at Site 827. Full APC and XCB cores from Hole 827A were measured using the gamma-ray attenuation porosity evaluator (GRAPE) and compressional wave (*P*-wave) logger on the multisensor track. Undrained shear-strength measurements were completed on the APC cores of Hole 827A (0–91.2 mbsf). All measurements at Site 827 were made according to the procedures described in the "Explanatory Notes" chapter, (this volume).

Index Properties

Values of porosity (wet and dry), water content (wet and dry), and bulk density (wet-, dry-, and grain) for Site 827 are listed in Table 5. Figure 30 illustrates the variation of porosity and bulk density as a function of sub-bottom depth. In Figure 31, bulk density trends often mirror those of porosity and water content; therefore, bulk density and porosity are plotted against depth, along with the lithostratigraphic units.

At Site 827, porosity ranges from 15.6% to 65.3%, water content ranges from 5.7% to 59.8%, and bulk density ranges

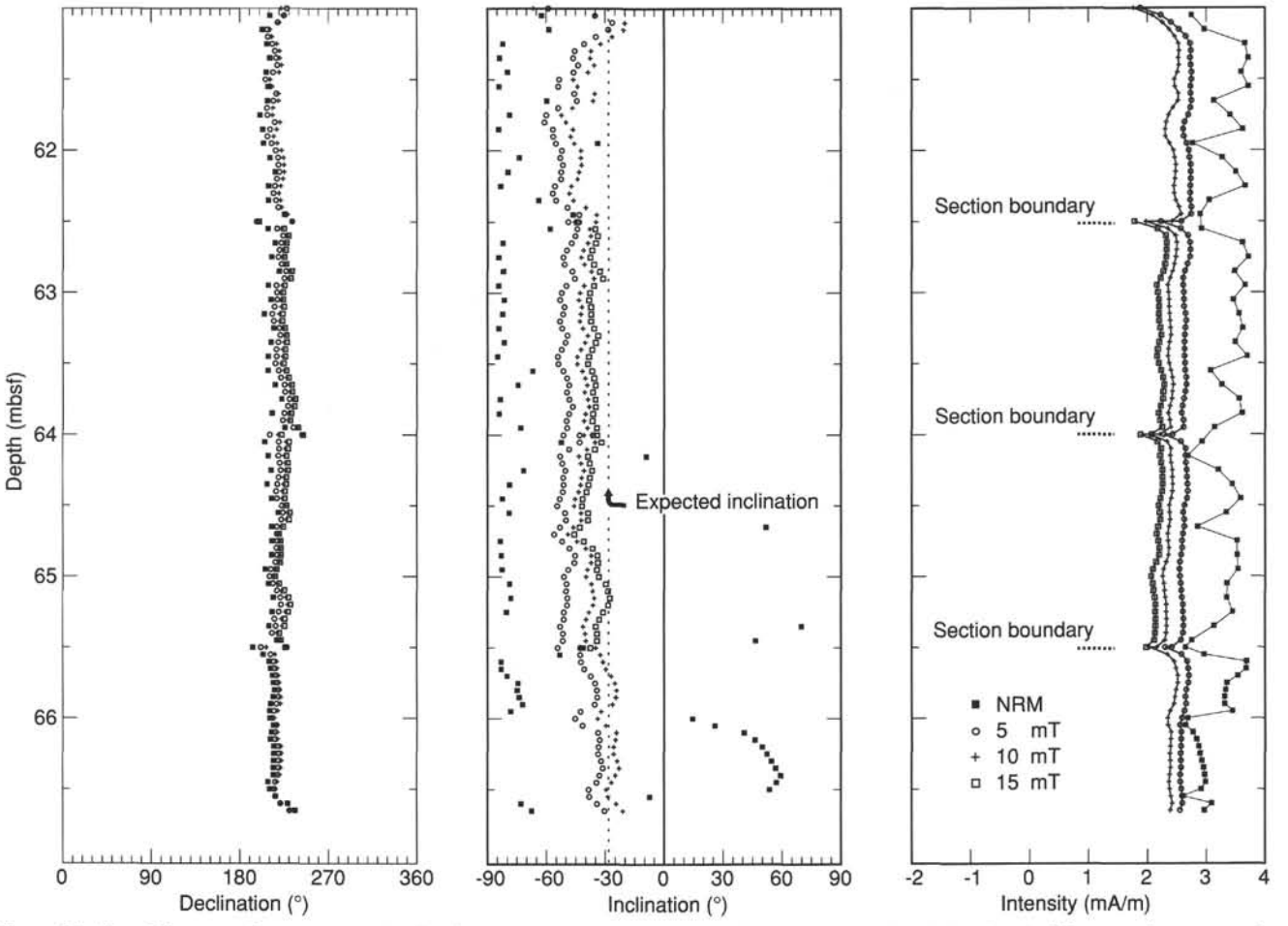

Figure 24. Plot of the natural remanent magnetization (NRM) vs. depth (mbsf) for Core 134-827A-8H. NRM data (solid squares) correspond to strong intensities and steep upward directions. The NRM intensity varies greatly because it exceeds the limits of measurement in the cryogenic magnetometer. Upon demagnetization at 5 (circles), 10 (crosses), and 15 mT (open squares), the inclination shallows toward the value expected at this latitude (–29°).

from 1.67 to 2.96 Mg/m^3. Index properties correlate well with the four lithostratigraphic units described at Site 827 (see "Lithostratigraphy" section, this chapter, for detailed descriptions of the units). Therefore, the discussion of index properties is organized by lithostratigraphic unit.

Lithostratigraphic Unit I (0–86 mbsf) consists of dark green volcanic siltstone; three subunits are identified based on the frequency of occurrence of sandy graded beds, interpreted as turbidites. Subunit IA (0–40 mbsf) contains occasional graded beds, Subunit IB is a continuous sequence of graded interbeds 1–10 cm thick, and Subunit IC contains fewer graded beds than either of the overlying subunits. The porosity and water content decrease from values of 63% and 59%, respectively, a few meters below the seafloor to a porosity of 53% and a water content of less than 40% at 40 mbsf. Porosity and water content increase slightly (to 60% and 50%) in Subunit IB (40–67 mbsf), but decrease again in Subunit IC (67–86 mbsf) to 51% and 35% at the contact with lithostratigraphic Unit II (Figs. 30 and 31). The variations in these index properties probably reflect the relative amounts of graded beds in each subunit because they are sandy and porous. Bulk density increases fairly steadily throughout Unit I, from 1.75 Mg/m^3 at the seafloor to more than 2.00 Mg/m^3 at 86 mbsf (Figs. 30 and 31).

Lithostratigraphic Unit II (86–141 mbsf) consists of partially lithified volcanic siltstone cut by a few small faults. Unit II is slightly denser, drier, and less porous than Unit I: porosity is always less than 55%, water content is less than 40%, and bulk density remains constant at about 2.0 Mg/m^3 (Figs. 30 and 31).

Lithostratigraphic Unit III (141–252 mbsf) is divided into three subunits. Subunit IIIA (141–200 mbsf) contains calcareous volcanic siltstone with some conglomerate and breccia. Bulk density decreases sharply in this subunit to the values observed at the top of the hole (1.75 Mg/m^3). Water content increases steadily from around 40% at 141 mbsf to 60% at 198 mbsf, with the highest water content measured at Site 827.

The first appearance of tectonic deformation is indicated by small faults observed at 107 mbsf and the amount of deformation increases downhole below 140 mbsf. Two zones of major tectonic deformation occur between 180–200 mbsf and 230–250 mbsf (see "Structural Studies" section, this chapter). Porosity and water content show distinct increases in scaly fabric located at all these depths. Subunit IIIB (200–218 mbsf) comprises conglomerate and breccia with clasts of volcanic siltstone and rare pelagic limestone, and is located between the tectonic deformation zones. Water content in the subunit decreases sharply to 34% and bulk density rises to 2.09 Mg/m^3. The trends reverse in the siltstone and interbedded ash and ooze of Subunit IIIC (218–252.5 mbsf). Bulk density drops below 2.00 Mg/m^3 and water content rises above 40%. Between 232 and 250 mbsf, the second interval identified as a

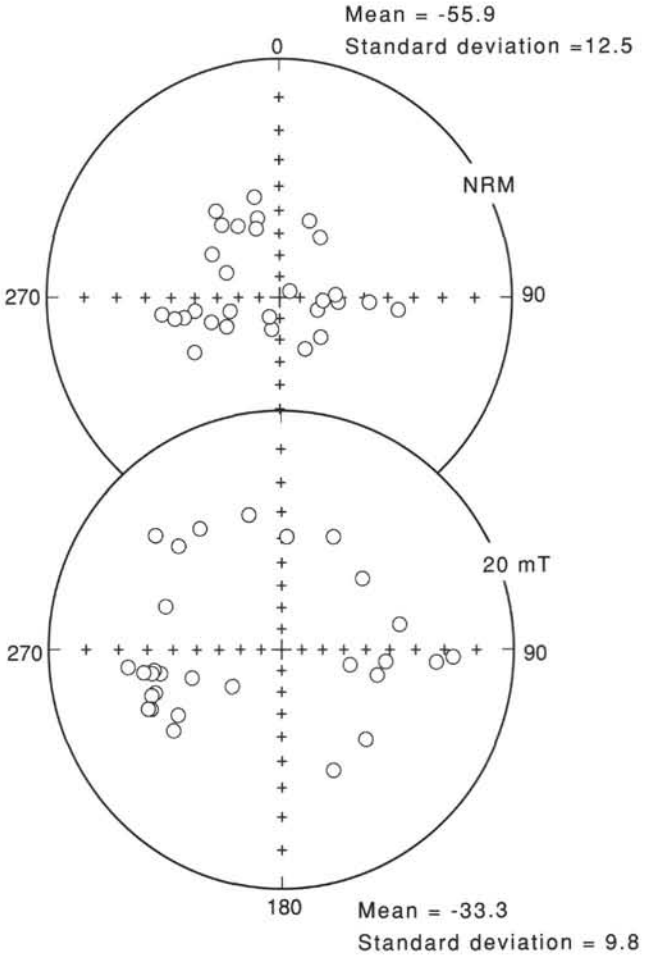

Figure 25. Stereographic projections of the NRM and 20-mT data for 29 discrete specimens from Hole 827A. Whereas NRM inclination is steeper than the predicted inclination, the mean inclination at 20 mT (–33.3°) is close to the expected inclination (–29°).

major shear zone, water content reaches 56% and bulk density is 1.77 Mg/m^3 (Figs. 30 and 31). Porosity in the sheared zone exceeds 64%, a higher value than at the seafloor.

Few measurements could be made in lithostratigraphic Unit IV (252.5–400 mbsf), which consists of intensely deformed sed-lithic conglomerate. The unit exhibits high bulk density values (2.3 Mg/m^3 or more), low porosity, and very low water content (less than 25%) (Figs. 30 and 31).

Sonic Velocity

Sonic velocities from Hole 827A measured in the *P*-wave logger and the Hamilton Frame velocimeter generally agree well (Table 6 and Fig. 30). Only Hamilton Frame measurements were obtained for Hole 827B. Because Hamilton Frame data exist for both holes, only these data are discussed here.

The velocity data at Site 827 correspond well with the lithostratigraphic units. Vertical velocities range from 1511–4744 m/s; horizontal velocities range from 1569–4986 m/s; therefore, velocities may be considered isotropic.

In lithostratigraphic Unit I (0–86 mbsf), sonic velocity averages about 1600 m/s. Below 80 mbsf, velocities increase to 1700 m/s or more. The higher velocity correlates with the partially lithified volcanic siltstone of Unit II (86–141 mbsf), which is generally a denser, drier, and less porous unit than Unit I. In the carbonate-enriched volcanic siltstone of Unit III

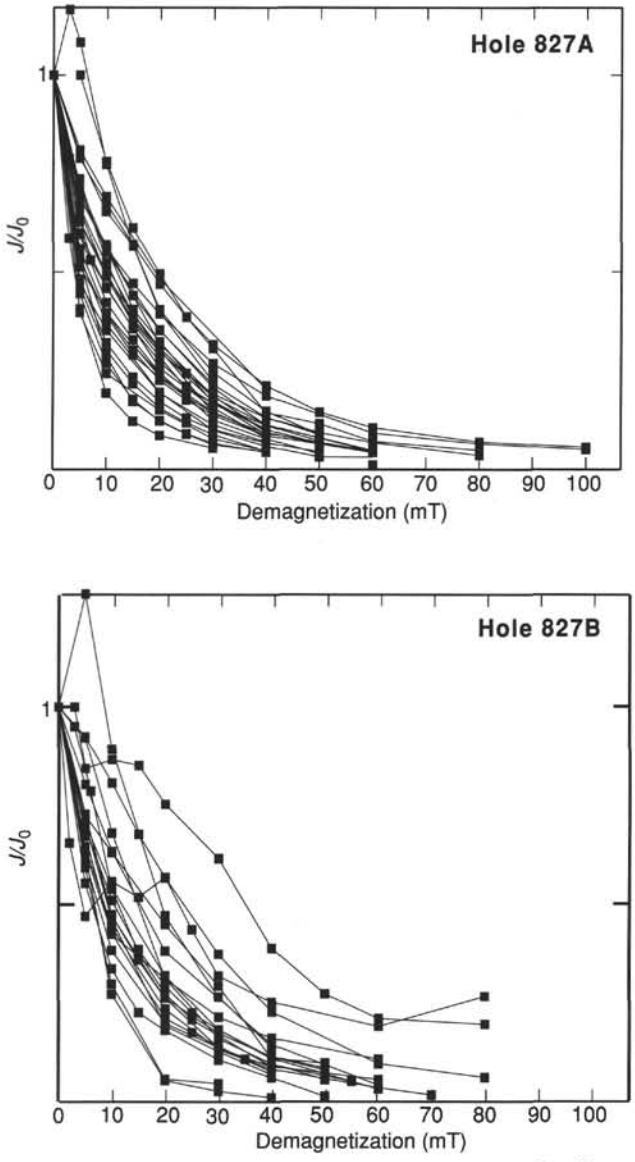

Figure 26. NRM intensities vs. AF demagnetization step for discrete samples from Holes 827A and 827B. J/J_0 is the ratio of magnetic intensity (J) after demagnetization at a particular step to the NRM intensity (J_0) The strong concave-up curvature of the demagnetization curves indicates very low stability of the NRM.

(141–252 mbsf), sonic velocities increase with depth from 1700 m/s to 2100 m/s. In Subunits IIIA and IIIC, velocity averages 1800 m/s, and in Subunit IIB, average velocity is 1900 m/s. This correlates with the higher bulk densities and lower water content values in Subunit IIIB relative to Subunits IIIA and IIIC. In the sed-lithic conglomerate of Unit IV (252–400 mbsf), velocities were generally much higher, sometimes exceeding 4000 m/s (Fig. 30). The wide variation in the velocities probably results from the mud matrix of the breccias.

Shear Strength

Undrained shear-strength tests were performed only on the APC and XCB cores of Hole 827A (0–110.6 mbsf); all other cores were too stiff and lithified to measure. Sediment shear strength shows a strong, generally linear increase with depth, although the measurements vary (Table 7 and Fig. 32). The

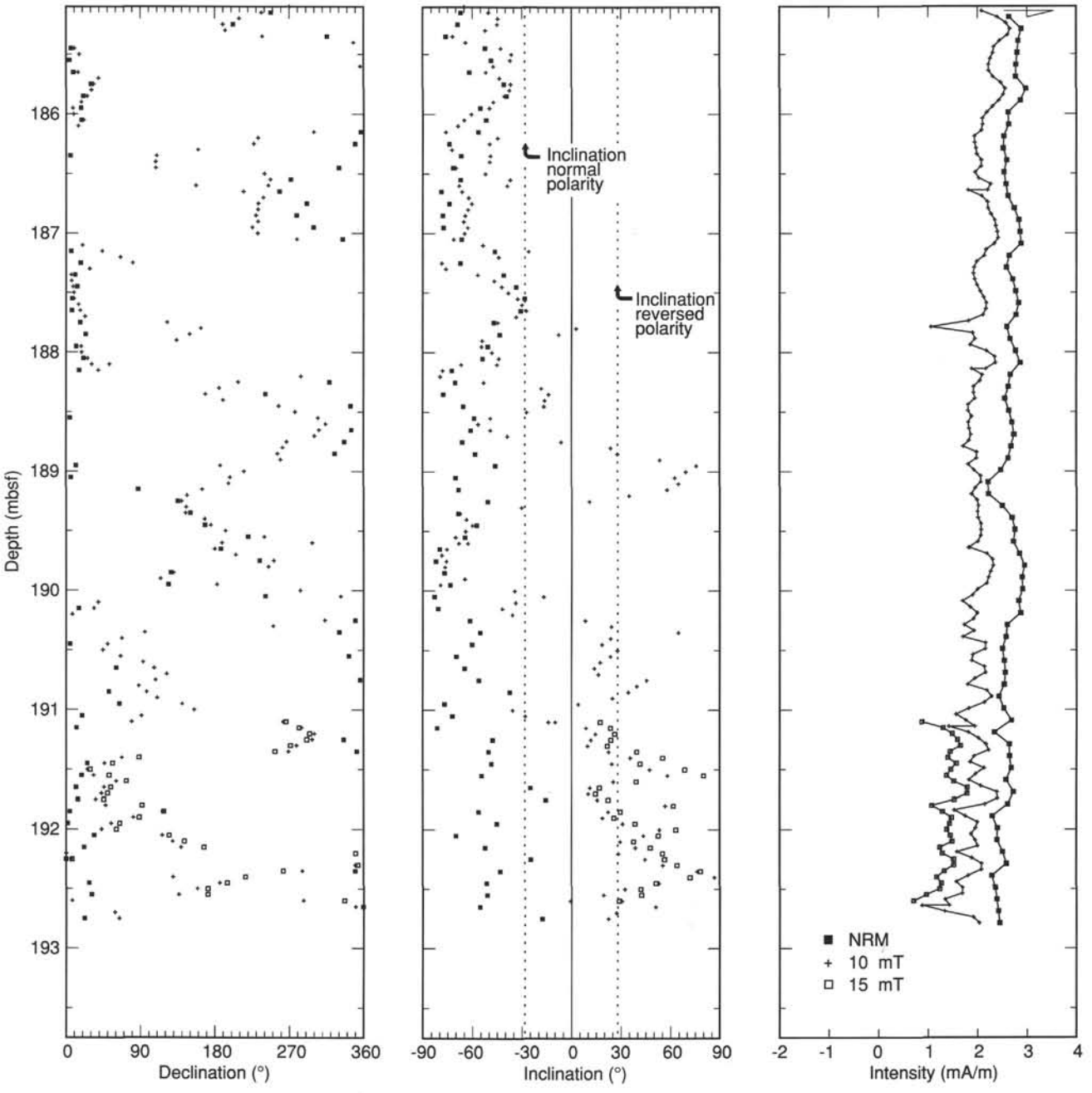

Figure 27. Paleomagnetic data from Core 134-827B-9R. Symbols are the same as in Figure 24.

variation may result from changes in silt content in the turbidite horizons, as siltier zones tend to have greater shear strength. Between 50–70 mbsf, variations in shear strength reflect the graded interbeds of the numerous silty turbidites in Subunit IB (see "Lithostratigraphy" section, this chapter, Fig. 33). This interval also corresponds to maxima in ammonia, phosphate, and alkalinity (see "Sediment and Fluid Geochemistry" section, this chapter). Shear strength increases sharply from 80–90 mbsf, the location of the boundary (86 mbsf) between Unit I and the partially lithified volcanic siltstones of Unit II.

Thermal Conductivity

Thermal conductivity values range from 0.8 to nearly 1.5 W/(m · K) (Table 8) and follow a pattern that is nearly the inverse of the plots for water content and porosity (Fig. 33). The inverse relationship between water content and thermal conductivity has been long established and is discussed by Lovell (1985) for both deep-sea clays and clean sands.

Thermal conductivity increases steadily from less than 1 at the seafloor to 1.2 W/(m · k) in the partially lithified volcanic siltstone of Unit II (86–141 mbsf), shadowing the decrease in water content in the same interval. Both maximum (1.5 W/[m · K]) and minimum (0.8 W/[m · K]) thermal conductivity values occur in Unit III. This variation reflects not only changes in porosity and water content but also correlates with changes in calcium carbonate content in the calcareous volcanic siltstone, conglomerate, and breccia of Unit III (141–252.6 mbsf) (see "Lithostratigraphy" section, this chapter). Calcium carbonate ranges from 0%–40% in Unit III and the increases in

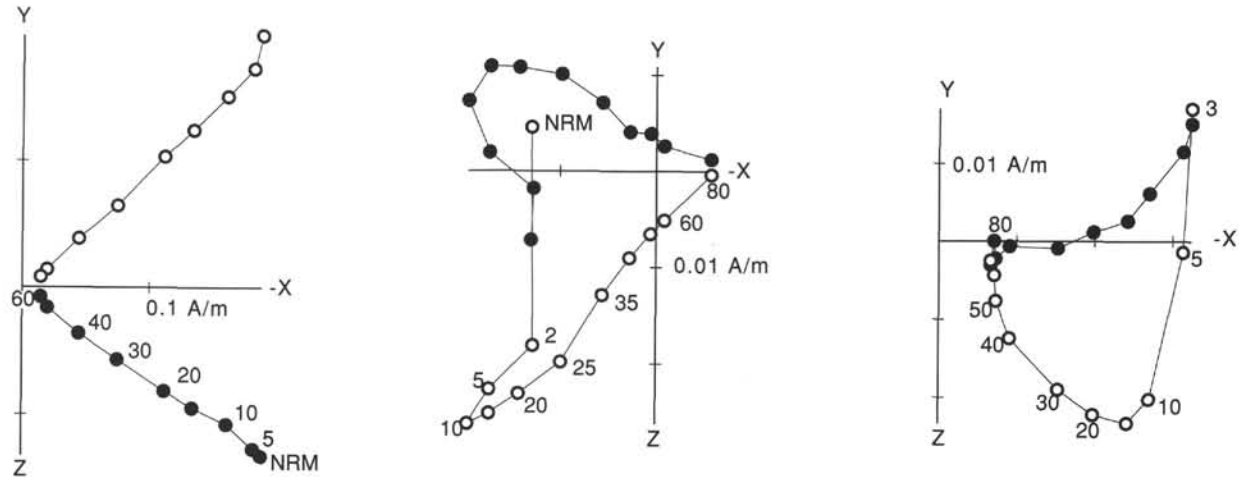

Figure 28. Orthogonal plots of demagnetization data from three samples of Hole 827B. Note the evidence for stable positive inclination which suggests a possible reversed polarity, if we assume that bedding is nearly horizontal. Open circles correspond to projections onto the vertical plane and filled circles correspond to projections onto the horizontal plane.

carbonate correspond to decreases in water content and thermal conductivity. The highest thermal conductivity value (1.49 W/[m · K]) occurs at 230 mbsf, a point where water content is a low 32%, and $CaCO_3$ is at a near-high value of 44% for Site 827 (see "Lithostratigraphy" section, this chapter; Fig. 8).

Summary

Physical properties of sediments and rocks from Site 827 display an inverse correlation in the relationship between water content and porosity versus calcium carbonate and thermal conductivity. Subunits IIIA (141–200 mbsf) and IIIC (218–252 mbsf), which are zones of major tectonic deformation (see "Structural Studies" section, this chapter), have notably higher porosity and water content and relatively lower bulk density, sonic velocity, and thermal conductivity values (Figs. 30 and 33). Unit III has a high but variable calcium carbonate content, ranging from 0% to 45% but averaging about 30% (see "Lithostratigraphy" section, this chapter; Fig. 8). Water content and porosity are high in tectonically deformed zones and in horizons where carbonate content and thermal conductivity are low. The tectonically deformed shear zones may be serving as dewatering conduits for fluids at Site 827.

DOWNHOLE MEASUREMENTS

Downhole temperature measurements at Site 827 consisted of five successful runs of the water sampler temperature probe (WSTP) temperature tool. The temperature measurement portion of this tool is based on the Uyeda Deep Sea Drilling Project (DSDP) temperature tool (Yokota et al., 1980).

The temperature measurements were extrapolated to equilibrium sediment temperature values using the 1/time approximation technique. This is valid after the first 2 min following insertion of the probe into the sediment. The temperature measurements were then combined with the shipboard needle-probe thermal conductivity measurements (see "Physical Properties" section, this chapter; Table 8 and Fig. 33) to determine the heat flow value. This was done by plotting the temperature values vs. the depth integral of the thermal resistivity (the inverse of the conductivity). The slope of this linear regression is the conductive heat flow.

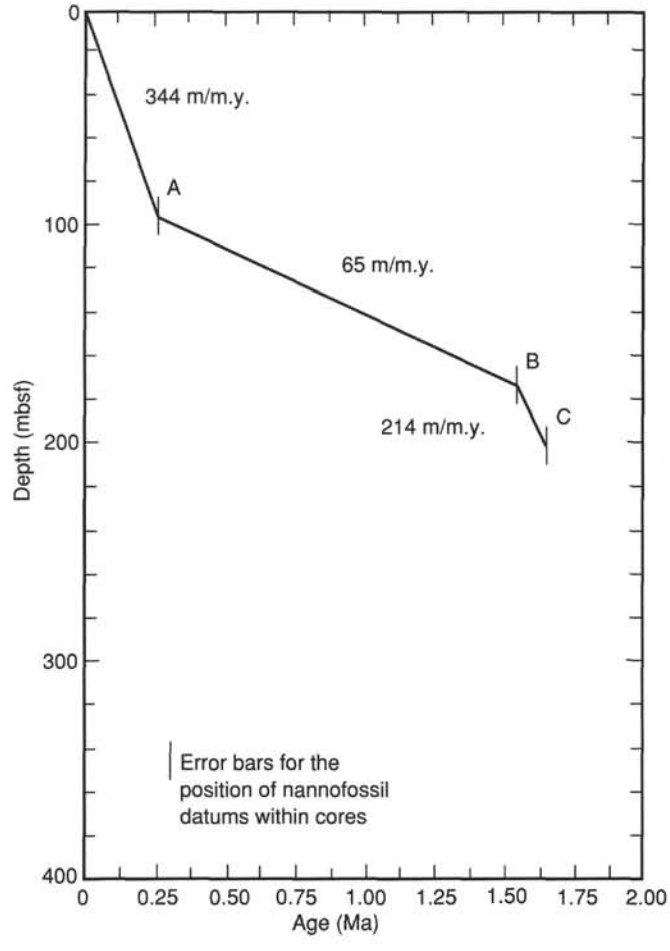

Figure 29. Age vs. depth plot for Site 827 using calcareous nannofossil datums. **A.** First occurrence of *Emiliania huxleyi* (0.28 Ma). **B.** First occurrence of *Gephyrocapsa oceanica* (1.57 Ma). **C.** First occurrence of *Gephyrocapsa caribbeanica* (1.66 Ma).

The individual temperature measurements are discussed below:

Run 4H in Hole 827A (Fig. 34) was done at a depth of 28.8 mbsf. The run had a good mudline reference temperature before the penetration and no disturbances during the measurement up to about 78 min in the run. The data after that were disturbed by motion of the probe in the bottom. The reduction to equilibrium temperature is plotted in Figure 35.

Run 8H in Hole 827A (Fig. 36) was done at a depth of 61.0 mbsf. This run had a good mudline reference temperature before and after the penetration and no disturbances during the measurement. The reduction to equilibrium temperature is plotted in Figure 37.

Run 11H in Hole 827A (Fig. 38) was done at a depth of 77.6 mbsf. This run also had good mudline reference temperatures before and after the penetration and no disturbances during the measurement. The reduction to equilibrium temperature is plotted in Figure 39.

Run 1R in Hole 827B (Fig. 40) was done at a depth of 110.0 mbsf. This run had a good mudline reference temperature before the penetration but only a brief hold at the mudline after pullout from the bottom. The reduction to equilibrium temperature is plotted in Figure 41.

Run 10R in Hole 827B (Fig. 42) was done at a depth of 194.7 mbsf. This run had good mudline reference temperatures before and after the penetration and no disturbance while it was in the bottom. The reduction to equilibrium temperature is plotted in Figure 43.

The five equilibrium temperatures are plotted against integrated thermal resistivity in Figure 44. The temperatures are plotted as delta temperatures relative to the mudline temperatures. This results in a slight increase in accuracy because it reduces errors caused by inaccuracies in absolute temperature calibration between different WSTP instruments. The measurements agree with the least-squares linear regression fit to within 0.1–0.2 Kelvin, which is adequate but not outstanding. The slope of the plotted linear regression indicates that the heat flow is 23.8 mW/m^2. This is a low value but not atypical for a forearc environment. There are no existing heat flow values in the vicinity to compare to this one.

SUMMARY AND CONCLUSIONS

Site 827 is located on the lower part of the forearc slope where the North d'Entrecasteaux Ridge (NDR) collides with the central New Hebrides Island Arc. The purpose of drilling at Site 827 was to investigate arc-ridge collision processes and to determine tectonic accretion of ridge fragments, timing of deformation, and uplift of the arc slope. Studies of the physical properties of arc-slope material and analyses of fluids were undertaken to assist in the definition of deformation processes.

Site 827 is located at 15°17.75′S, 166°21.11′E, at a depth of 2803.4 mbsl, on a flat terrace-like feature along the northern flank of Wousi Bank, an anomalously shallow arc-slope feature that is aligned with the NDR. The site is 4 km east of the trace of the subduction zone and about 35 km west of the western shore of Espiritu Santo Island. Hole 827A was continuously cored by APC to a depth of 91.5 mbsf and by XCB to a depth of 110.6 mbsf. Hole 827B was rotary-cored from 110.6 mbsf to a total depth of 400.4 mbsf. Drilling both holes took 4 days, 14 hr, and 15 min. The average recovery rate of Hole 827A was 91%, whereas that of Hole 827B was only 41% with the last 16 cores having a recovery rate as low as 5%. Conditions in Hole 827B started to deteriorate near depths of 339 and 388 mbsf. As a result of hole collapse, we were forced to abandon Hole 827B before reaching our objectives. No logging was performed.

We recovered over 200 m of upper Pliocene(?) to Pleistocene strata from which the sedimentologic and tectonic history of the Wousi Bank can be tentatively interpreted. Here, we summarize and discuss the lithostratigraphy, biostratigraphy, tectonic structures, paleomagnetism, physical properties, and fluid geochemistry at Site 827 and present preliminary interpretations of the data.

Four main lithostratigraphic units (Units I–IV) were identified in Holes 827A and 827B. These units were defined by variations in texture and sedimentary and tectonic structures.

Lithostratigraphic Unit I (0–86 mbsf) consists of dark gray volcanic silt interbedded with normally graded volcanic silty sand. A Pleistocene age is assigned to the unit based on microfossils and paleomagnetic data showing deposition within the Brunhes magnetic epoch (<0.7 Ma; Fig. 45). Reworked microfossils of Pliocene and Miocene age are also common in Unit I. Three subunits were defined based on the frequency of graded beds. The number of graded beds per cored section (1.5 m) increases from 20 in Subunit IA, to about 50 in Subunit IB, and then decreases to less than 20 in Subunit IC (Fig. 10; see "Lithostratigraphy" section, this chapter). Unit I shows no apparent tectonic deformation.

The abundance of graded beds throughout Unit I suggests that the sediments are primarily turbidite deposits. Nannofossil ages suggest rapid deposition of the turbiditic sediments at a rate of 344 m/m.y. (see Fig. 29; "Sediment Accumulation Rates" section, this chapter). Rapid sedimentation is consistent with low total carbonate values (~10%) throughout the unit, which reflects a low abundance of pelagic foraminifers in the volcanic sediments (see Fig. 8; see "Lithostratigraphy" section, this chapter). Data from benthic foraminifers suggest deposition of lithostratigraphic Unit I in the middle bathyal zone, at depths greater than 500 m, and the upper 44.9 m of sediment in Hole 827A in a low-oxygen environment.

Lithostratigraphic Unit II (86–141 mbsf) consists primarily of volcanic silt that contains variable proportions of clay to sand; the silt becomes partially lithified near the base of the unit. Lithostratigraphic Unit II is differentiated from lithostratigraphic Unit I by the absence of graded beds. Lithostratigraphic Unit II contains a few faults (Fig. 45) indicative of minor tectonic deformation. Total carbonate content increases from about 10% at the top of Unit II to 15%–20% at its base (Fig. 8; "Lithostratigraphy" section, this chapter); a corresponding decrease in volcanic components is suggested by a decrease in magnetic susceptibility throughout the unit (Fig. 24; "Paleomagnetism" section, this chapter).

Foraminifer data indicate a late Pliocene age for lithostratigraphic Unit II, although nannofossil data suggest an age of middle Pleistocene. Paleomagnetic data show that at least the upper few meters of the unit are within the Brunhes magnetic epoch (<0.7 Ma; Fig. 45). The estimated sediment accumulation rate for Unit II based on nannofossil ages is 65 m/m.y. (Fig. 29; see "Sediment Accumulation Rates" section, this chapter). Benthic foraminifer data suggest deposition at depths greater than 500 m, in a middle bathyal environment. The ungraded, fine-grained sediments in Unit II are interpreted as hemipelagic deposits (see "Lithostratigraphy" section, this chapter).

Lithostratigraphic Unit III (141–252.6 mbsf) consists mainly of highly bioturbated, partially lithified, dark greenish gray, calcareous volcanic siltstone with intervals of sed-lithic conglomerate and breccia. The age of lithostratigraphic Unit III is uncertain and is either late Pliocene, based on foraminifers, or middle Pleistocene, based on nannofossils (Fig. 45). Highly tectonized zones within lithostratigraphic Unit III are interpreted as possible thrust faults (see "Structural Studies" section, this chapter), which may complicate stratigraphic

Table 5. Index properties data, Site 827.

Sample (cm)	Depth (mbsf)	Unit	Wet-bulk density (Mg/m^3)	Dry-bulk density (Mg/m^3)	Grain density (Mg/m^3)	Porosity		Water content	
						Wet (%)	Dry (%)	Wet (%)	Dry (%)
134-827A-									
1H-1, 40	0.40	IA	1.75	1.10	2.73	63.1	61.2	37.0	58.7
1H-3, 37	3.37	IA	1.86	1.25	2.73	59.1	56.6	32.6	48.4
1H-5, 37	6.37	IA	1.67	1.16	2.76	49.5	54.3	30.4	43.7
2H-2, 33	11.63	IA	1.89	1.29	2.75	58.6	55.9	31.8	46.7
2H-4, 44	14.74	IA	1.93	1.33	2.72	58.8	54.9	31.2	45.4
2H-6, 135	18.65	IA	1.93	1.37	2.71	54.7	52.3	29.1	41.0
3H-1, 37	19.67	IA	1.90	1.32	2.74	56.6	54.3	30.5	44.0
3H-3, 37	22.67	IA	1.96	1.40	2.74	54.6	51.8	28.5	39.8
3H-5, 37	25.67	IA	1.92	1.37	2.73	53.9	52.0	28.7	40.3
3H-7, 37	28.67	IA	1.97	1.43	2.72	52.4	50.1	27.2	37.4
4H-1, 37	29.17	IA	1.90	1.33	2.67	56.1	53.3	30.2	43.3
4H-3, 37	32.17	IA	1.96	1.35	2.77	58.8	54.9	30.8	44.6
4H-5, 37	35.17	IA	2.00	1.43	2.80	55.5	52.2	28.4	39.6
5H-1, 37	36.87	IA	1.94	1.39	2.77	53.6	51.8	28.3	39.4
5H-3, 37	39.87	IA	1.94	1.39	2.80	53.5	52.1	28.3	39.5
5H-5, 37	42.87	IB	2.00	1.43	2.75	55.0	51.6	28.2	39.3
6H-1, 37	45.27	IB	1.83	1.25	2.65	56.9	55.0	31.8	46.7
6H-3, 37	48.27	IB	1.99	1.41	2.73	56.9	52.7	29.2	41.3
6H-4, 127	50.67	IB	1.91	1.38	2.71	51.6	50.6	27.7	38.3
6H-5, 37	51.27	IB	1.75	1.18	2.23	55.5	51.6	32.6	48.4
7H-1, 37	53.17	IB	1.97	1.38	2.75	57.4	53.6	29.9	42.6
7H-3, 37	56.17	IB	2.02	1.45	2.71	56.4	51.6	28.5	39.9
7H-5, 37	59.17	IB	2.02	1.44	2.77	56.2	52.2	28.6	40.0
7H-5, 120	60.00	IB	2.11	1.51	2.72	58.0	51.3	28.2	39.2
8H-1, 37	61.37	IB	1.97	1.41	2.73	54.7	51.7	28.5	39.8
8H-3, 37	64.37	IB	1.87	1.25	2.73	59.7	56.9	32.8	48.8
9H-2, 37	68.87	IC	1.97	1.44	2.76	52.3	50.3	27.1	37.2
9H-4, 37	71.87	IC	1.95	1.44	2.74	50.2	49.1	26.3	35.8
10H-1, 130	73.80	IC	1.97	1.42	2.74	54.1	51.3	28.1	39.1
10H-2, 131	75.31	IC	2.00	1.44	2.66	54.3	50.3	27.8	38.5
10H-4, 40	77.40	IC	1.82	1.29	2.75	51.9	52.8	29.2	41.2
11H-1, 75	78.35	IC	2.02	1.42	2.67	58.3	52.5	29.5	41.9
11H-2, 73	79.83	IC	1.98	1.42	2.72	54.3	51.2	28.1	39.2
11H-4, 41	82.51	IC	2.05	1.50	2.71	53.3	49.3	26.7	36.4
12H-1, 43	83.63	IC	1.94	1.37	2.75	56.3	53.4	29.7	42.2
12H-1, 125	84.45	IC	2.03	1.44	2.71	56.7	51.8	28.7	40.2
12H-2, 30	85.00	IC	2.00	1.47	2.74	51.1	49.0	26.2	35.5
13H-1, 40	88.20	II	1.97	1.44	2.71	50.9	49.1	26.5	36.1
13H-3, 41	91.21	II	1.98	1.45	2.70	52.0	49.6	26.9	36.9
14X-1, 77	92.27	II	1.94	1.39	2.72	53.5	51.4	28.3	39.4
15X-1, 67	101.67	II	1.93	1.37	2.67	54.5	51.7	28.9	40.6
15X-3, 67	104.67	II	1.93	1.37	2.70	54.6	52.1	29.0	40.8
15X-5, 67	107.67	II	1.96	1.34	2.70	59.8	54.8	31.3	45.6
134-827B-									
1R-2, 37	112.47	II	2.00	1.47	2.70	51.4	48.8	26.4	35.8
2R-2, 35	119.45	II	1.95	1.40	2.69	54.3	51.3	28.5	39.8
2R-4, 130	123.40	II	1.95	1.41	2.72	52.8	50.8	27.8	38.5
2R-6, 20	125.30	II	2.00	1.47	2.73	52.2	49.5	26.7	36.4
3R-1, 110	128.30	II	1.95	1.40	2.77	53.7	51.8	28.2	39.3
3R-3, 135	131.55	II	1.96	1.41	2.74	53.7	51.3	28.1	39.1

relationships within the unit. An apparent absence of biostratigraphic inversion, as shown by preliminary paleontological data (see "Biostratigraphy" section, this chapter), may be evidence that the possible thrust zones are intraformational.

Lithostratigraphic Unit III is divided into three subunits based on the abundance of sed-lithic conglomerate. Lithostratigraphic Subunit IIIA consists of 59 m of calcareous volcanic siltstone with three intervals of sed-lithic conglomerate 10–30 cm thick (Fig. 45). The conglomerate contains centimeter-sized clasts of volcanic siltstone, sandstone, and chalk. The subunit is highly fractured and sheared, with several high-angle faults showing evidence of reverse motion (see "Structural Studies" section, this chapter). Two major zones (up to 1 m thick) and several minor horizons of scaly fabric occur within the siltstone between 160 and 200 mbsf (Fig. 45).

Sediment accumulation rates based on nannofossil ages and paleodepths based on benthic foraminifers show apparent changes during the deposition of Subunit IIIA. The upper part of the subunit is characterized by a sedimentation rate of 65 m/m.y., whereas the rate in the lower part of the subunit is 214 m/m.y. (Fig. 29; "Sediment Accumulation Rates" section, this chapter). Correspondingly, benthic foraminifers suggest that the upper part of the subunit was deposited in the middle bathyal zone at depths >500 m and that the lower part of the subunit in the lower bathyal zone at depths >2000 m. These apparent changes in accumulation rates and paleodepths may be invalid, however, if thrusts have displaced the sediments and thickened the subunit.

Lithostratigraphic Subunit IIIB consists of 18 m of sed-lithic conglomerate and breccia with a few intervals of calcareous siltstone. Conglomerate clasts are rounded to angular,

Table 5 (continued).

Sample (cm)	Depth (mbsf)	Unit	Wet-bulk density (Mg/m^3)	Dry-bulk density (Mg/m^3)	Grain density (Mg/m^3)	Porosity Wet (%)	Porosity Dry (%)	Water content Wet (%)	Water content Dry (%)
3R-5, 135	134.55	II	1.90	1.32	2.71	56.3	53.9	30.4	43.6
3R-7, 20	136.40	II	1.96	1.40	2.67	54.7	51.4	28.6	40.1
4R-1, 97	137.87	II	1.97	1.42	2.73	53.3	50.8	27.8	38.5
4R-3, 97	140.87	II	1.93	1.38	2.76	53.3	51.7	28.3	39.4
4R-6, 97	145.37	IIIA	1.85	1.26	2.72	58.1	56.0	32.1	47.4
5R-1, 145	147.95	IIIA	1.81	1.20	2.71	60.1	57.9	33.9	51.4
5R-3, 80	150.30	IIIA	1.90	1.33	2.76	56.4	54.2	30.3	43.6
5R-5, 27	152.77	IIIA	1.88	1.30	2.66	56.7	54.0	30.9	44.7
6R-1, 140	157.60	IIIA	1.91	1.33	2.72	56.4	53.8	30.3	43.4
6R-2, 145	159.15	IIIA	1.80	1.15	2.78	63.0	60.6	35.9	56.1
6R-3, 140	160.60	IIIA	1.93	1.36	2.77	56.4	53.8	29.9	42.6
6R-4, 132	162.02	IIIA	1.81	1.18	2.73	61.2	58.9	34.7	53.1
7R-2, 140	168.70	IIIA	1.77	1.13	2.72	62.0	60.1	36.0	56.2
7R-3, 137	170.17	IIIA	1.88	1.30	2.71	56.7	54.5	30.9	44.7
7R-4, 137	171.67	IIIA	1.94	1.38	2.76	54.6	52.4	28.8	40.4
8R-1, 142	176.82	IIIA	1.89	1.34	2.68	53.2	51.7	28.8	40.5
8R-3, 62	179.02	IIIA	1.79	1.17	2.70	60.5	58.6	34.7	53.2
8R-5, 62	182.02	IIIA	1.85	1.25	2.71	58.2	56.0	32.3	47.7
9R-1, 37	185.47	IIIA	1.75	1.12	2.71	61.6	60.1	36.0	56.3
9R-3, 37	188.47	IIIA	1.84	1.22	2.69	60.4	57.3	33.6	50.6
9R-5, 37	191.47	IIIA	1.83	1.22	2.72	58.7	56.9	33.0	49.2
10R-1, 37	195.07	IIIA	1.82	1.21	2.75	60.3	58.1	33.8	51.1
10R-3, 37	198.07	IIIA	1.73	1.08	2.70	63.3	61.5	37.4	59.8
10R-5, 37	201.07	IIIB	2.09	1.56	2.76	52.0	48.1	25.4	34.1
11R-1, 37	204.77	IIIB	1.79	1.20	2.63	57.2	55.9	32.8	48.8
11R-3, 37	207.77	IIIB	1.67	1.14	2.47	51.0	52.7	31.3	45.6
12R-1, 65	214.65	IIIB	1.97	1.43	2.73	52.5	50.2	27.3	37.5
12R-3, 37	217.37	IIIB	2.02	1.52	2.74	49.6	47.5	25.1	33.5
13R-1, 44	224.14	IIIC	1.99	1.47	2.72	50.1	48.3	25.8	34.8
13R-3, 45	227.15	IIIC	1.96	1.41	2.76	53.7	51.5	28.1	39.1
13R-5, 40	230.10	IIIC	2.03	1.53	2.76	48.0	46.5	24.3	32.0
13R-6, 105	232.25	IIIC	1.95	1.32	2.73	61.3	56.1	32.2	47.6
14R-1, 20	233.50	IIIC	1.77	1.14	2.69	61.4	59.4	35.6	55.2
14R-2, 89	235.69	IIIC	1.84	1.18	2.82	64.4	60.8	35.8	55.7
14R-3, 12	236.42	IIIC	1.88	1.29	2.73	57.2	55.0	31.2	45.4
15R-1, 124	244.24	IIIC	1.79	1.14	2.74	62.6	60.3	35.9	56.1
15R-3, 12	246.12	IIIC	2.08	1.57	2.75	49.9	46.9	24.6	32.6
15R-5, 10	249.10	IIIC	2.03	1.51	2.73	50.5	47.9	25.5	34.2
15R-6, 65	251.15	IIIC	1.92	1.32	2.70	58.5	54.6	31.1	45.2
16R-1, 10	252.70	IV	2.08	1.62	2.70	44.7	42.9	22.0	28.3
16R-1, 39	252.99	IV	2.17	1.77	2.60	39.5	36.9	18.6	22.9
17R-CC, 0	262.30	IV	2.67	2.49	2.72	17.4	16.1	6.7	7.2
19R-CC, 23	281.93	IV	2.39	2.17	2.52	21.4	2.0	9.2	10.1
20R-1, 20	291.50	IV	2.77	2.56	2.57	20.2	17.0	7.5	8.1
22R-1, 37	310.97	IV	2.17	1.77	2.65	39.3	37.3	18.6	22.8
23R-CC, 0	320.30	IV	2.96	2.80	2.81	15.6	13.6	5.4	5.7
26R-1, 6	345.76	IV	2.63	1.96	2.19	65.3	42.5	25.4	34.1
27R-1, 6	355.36	IV	2.46	2.22	2.60	23.7	21.9	9.9	10.9
29R-1, 10	374.60	IV	2.57	2.39	2.60	17.1	15.8	6.8	7.3
30R-1, 37	384.57	IV	2.09	1.61	2.74	46.5	44.3	22.8	29.5

1–3 cm in size, and composed mainly of gray sandstone with less common chalk, coral fragments, and igneous rocks; chalk clasts that were dated gave middle or late Eocene ages. High-angle faults, some indicating reverse motion, are present throughout lithostratigraphic Subunit IIIB.

Lithostratigraphic Subunit IIIC consists of 34 m of calcareous volcanic siltstone with a few-centimeter-thick ash layers and foraminiferal-nannofossil chalk; conglomerate is absent in this subunit. The occurrence of ash layers suggests that nearby volcanoes of the Central Chain of the New Hebrides Island Arc may have been active during this time. A major shear zone occurs within Subunit IIIC at about 243 mbsf in Hole 827B (Fig. 45). Several 1-m-thick horizons of scaly silt with high-angle foliation occur in this shear zone, which is interpreted as a possible thrust fault (see "Structural Studies" section, this chapter).

Lithologies within lithostratigraphic Unit III suggest that periods of debris flow or mass wasting alternated with hemipelagic and minor pelagic deposition. The poorly sorted conglomerates and breccias are interpreted to have been derived either from exposed rocks on submarine slopes or from nearby islands. The thin, ungraded calcareous siltstones are interpreted as hemipelagic deposits; the minor chalk intervals may represent periods of pelagic deposition or could be clasts within the conglomerate larger than the diameter of the drill bit (see "Lithostratigraphy" section, this chapter).

Lithostratigraphic Unit IV (252.6–400.4 mbsf), which is the deepest unit drilled at Site 827, is poorly understood because of low recovery. The unit is comprised mainly of sed-lithic conglomerate containing very angular to rounded, highly indurated and fractured, pebble-sized clasts of volcanic breccia, siltstone, and sandstone as well as rare andesite. The clasts of volcanic breccia are composed of fragments of andesite or, less commonly, dacite. In some intervals, clasts occur in a matrix of highly sheared, partially lithified dark gray volcanic silt; in other intervals, matrix is lacking, probably as

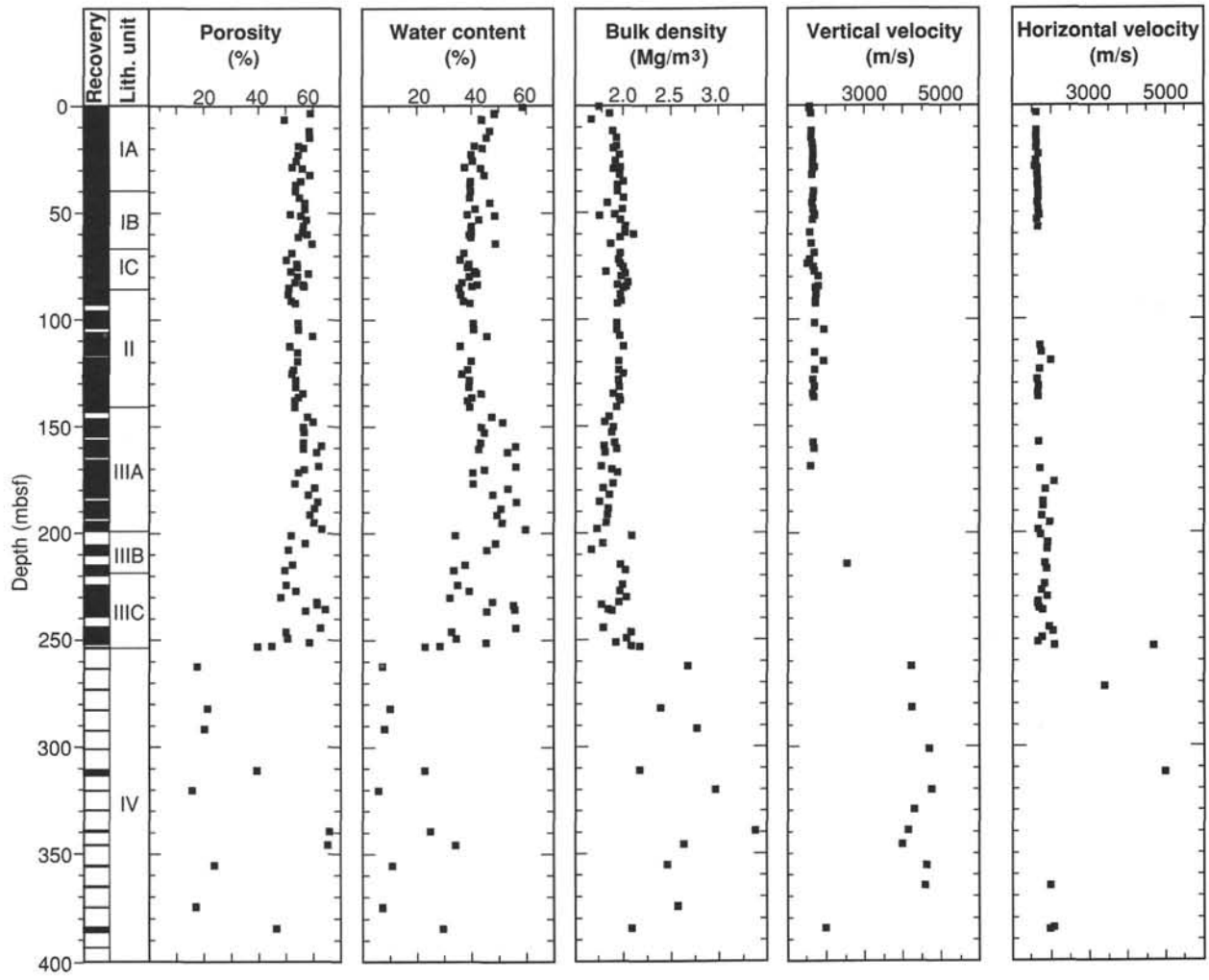

Figure 30. Porosity, water content, bulk density, and vertical and horizontal velocities vs. depth, Site 827.

a result of drilling. Single-channel seismic reflection data collected near Site 827 by the *JOIDES Resolution* suggest that the base of Unit IV is ~80 m below total depth of Hole 827B (see "Seismic Stratigraphy" section, this chapter). The upper contact of Unit IV is marked by a shear zone, which may be a thrust fault, at the base of Subunit IIIC (see "Structural Studies" section, this chapter).

The age and paleodepth of Unit IV is unknown because samples were barren. The poor sorting and large grain size of the clasts in Unit IV suggest a proximal source and deposition by mass wasting or debris flow mechanisms. Clasts in the conglomerate could be derived from Espiritu Santo Island or could have been scraped off from the North d'Entrecasteaux Ridge; additional work is needed to define source areas more specifically.

Physical properties correlate well with lithologic units and tectonic features. Particularly good correlations are evident within Subunits IIIA and IIIC. Both these subunits, which are highly deformed with reverse faults and major zones of scaly fabric, are characterized by high porosity (64%) and water content (50%–60%) and relatively low bulk density (about 1.75 Mg/m^3) compared to the other units. The high water content of these units suggests that the fractured rocks may be paths of fluid flow.

Geochemical analysis of pore fluids at Site 827 reveal anomalous concentrations of chloride, sodium, potassium, magnesium, calcium, sulfate, and methane. These anomalies suggest alteration of pore-fluid chemistry by diagenesis of volcanic rocks and upward migration of fluids from the subduction zone, as discussed below.

Concentrations of chloride, sodium, potassium, calcium, and magnesium at Site 827 show strong correlations with depth that could result from exchange reactions with igneous rocks or altered volcanic ash. In particular, chloride concentrations increase steeply with depth, reaching maximum concentrations of 14% higher than seawater at about 175 mbsf, between two major inferred thrust zones (Fig. 45). Such high concentrations of chloride (630 mM) are unusual; in other forearcs chloride concentrations decrease below seawater values (Gieskes et al., 1990a; Kastner et al., 1990). In addition, sodium and potassium concentrations decrease rapidly below depths of 75 and 125 mbsf, suggesting that igneous rocks at the base of the site are a sink for these elements. Finally, calcium and magnesium concentrations are inversely correlated at Site 827, similar to the pore fluids examined in the Barbados accretionary wedge (Gieskes et al., 1990b) where pore-fluid chemistry is interpreted to reflect alteration of basement rocks (McDuff and Gieskes, 1976).

Upward migration of fluids that were altered at depth is suggested by sulfate and methane concentrations at Site 827. A deep sulfate source is indicated by sulfate concentrations of up to 7.5 mM in sediments below the zone of complete sulfate

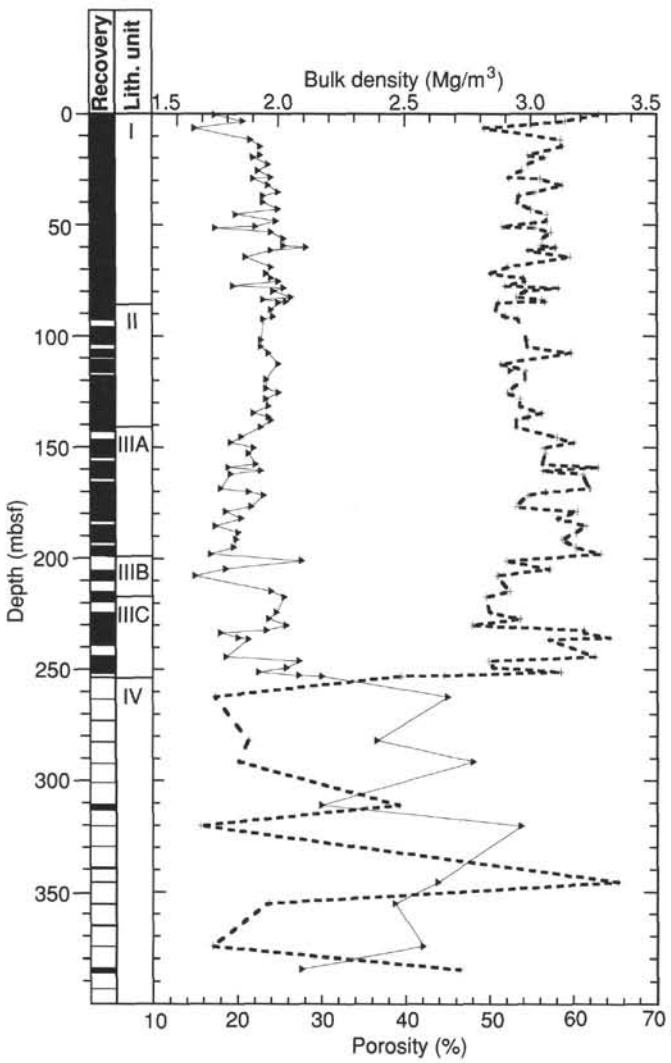

Figure 31. Porosity (crosses) and bulk density (triangles) vs. depth, Site 827.

reduction (about 50 mbsf). Increases in sulfate below the décollement in the Nankai accretionary wedge (Taira, Hill, Firth, et al., 1991) suggest that sulfate production may be related to subduction processes. In addition, fluids at depths of about 75 mbsf have anomalously high methane concentrations (30,000 ppm), as well as high silica and increased sulfate (Fig. 45), that are characteristic of fluids in the subduction zone at Barbados (Gieskes et al., 1990b) and in the Mariana forearc (Mottl, in press). The methane-rich interval at Site 827 occurs within a zone of numerous turbidite beds, suggesting that the turbiditic sands may act as pathways for methane-rich fluids carried upward from the décollement along thrust faults.

Drilling at Site 827 has shown that the 400 m of sediments and sedimentary rocks recovered on the western flank of the Wousi Bank are primarily volcanic in origin and were probably derived from the New Hebrides Island Arc rather than from the subducting NDR. The andesitic composition of clasts in the sed-lithic conglomerate of Unit IV suggest they were derived from an arc, rather than from the NDR, which is thought to be mid-ocean ridge basalt (Maillet et al., 1983). A likely source for the arc-derived clasts and the other volcanic sediments at Site 827 is the nearby Espiritu Santo Island, which has been emergent for at least 0.5 m.y. (Taylor et al., 1980, 1985, 1987) and possibly since the middle Pliocene (Mallick and Greenbaum, 1977; Carney and Macfarlane, 1982). The only lithology encountered at Site 827 that does not show arc affinities are chalk clasts (some are Eocene in age) in the sed-lithic conglomerates of Unit III. The absence of known deposits of Eocene chalk within the New Hebrides Island Arc suggests that these clasts could be derived from chalk deposits on the subducting NDR as suggested by the results of Site 828 (see "Site 828" chapter, this volume).

Further evidence supporting the interpretation that sediments at Site 827 are primarily derived from the New Hebrides Island Arc comes from seismic reflection investigations (Fisher et al., 1986, 1991) and results of *Nautile* dives (Collot et al., 1989) on the arc slope in the NDR collision zone. Seismic reflection data show that arc-slope rocks dip toward the trench and terminate at the décollement. This attitude suggests that rocks on the arc slope were derived from Espiritu Santo Island. In addition, the *Nautile* dives sampled basalt and andesitic lavas that were interbedded with coarse volcaniclastic sediment on the south flank of Wousi Bank and sampled volcanic breccia, volcanic sandstone, and tuffs on the arc slope north of Site 827. The lithologic similarity of rocks collected on the dives to lower Miocene volcanic rocks on Espiritu Santo Island again suggests that much of the material on the arc slope is derived from the island.

The upper 150 m of the sequence recovered at Site 827 is relatively undeformed, whereas the lower half is highly tectonized. Initially sediments could have been deposited on the arc slope and subsequently deformed, or they could have been deposited in the central New Hebrides Trench and then accreted to the arc slope as imbricated thrust sheets.

The ages of depositional events at Site 827 are not well defined. Biostratigraphic data indicate that the upper 125 m of the section was deposited in Pleistocene time. However, foraminiferal and nannofossil data disagree as to whether the interval from 125–252 mbsf is late Pliocene in age, as suggested by foraminifers, or middle Pleistocene, as suggested by nannofossils. In addition, the age of the interval from 252–400 mbsf is unknown because these sediments were barren. To add to these uncertainties, structural data suggest that the stratigraphic sequence in the interval from 150–400 mbsf is complicated by thrust faulting.

Possible thrust faults at Site 827 are indicated by zones of scaly fabric ranging in thickness from a few centimeters to 1 m in the interval 140–250 mbsf (Unit III). In addition, despite poor core recovery below 250 mbsf (Unit IV), the presence of highly deformed clasts and one 50-cm-thick horizon of scaly fabric are evidence that this part of the section also experienced strong deformation. The zones of scaly fabric are interpreted to result from severe fracturing, shearing, and granulation of rocks during the collision between the NDR and the arc slope.

The possibility that thrust faults may occur within Units III and IV at Site 827, as indicated by structural data, suggests that there may be age reversals within these units. Unfortunately, Unit IV is barren and nannofossils in Unit III are poorly preserved. In addition, the lack of foraminiferal stages in the late Pliocene prevents the detection of age reversals during this time.

Despite uncertainties regarding timing of deposition at Site 827 and the possible complications introduced by thrust faults, some preliminary interpretations can be made. The stratigraphic sequence at Site 827 may contain a record of the uplift of Wousi Bank. The morphology of Wousi Bank and its alignment with the NDR suggest that the bank was uplifted as a result of collision between the NDR and the arc. Water depths on the bank are considerably less than those of the arc slope north and south of the bank. For example, water depth at Site 827 on the flank of Wousi Bank is 3000 mbsl, whereas water depths on the arc slope north of the site at equivalent

Table 6. Vertical and horizontal velocity data, Site 827.

Sample (cm)	Depth (mbsf)	Unit	Vertical velocity (m/s)	Wave type[a]	Horizontal velocity (m/s)	Wave type[a]
134-827A-						
1H-1, 37	0.37	IA	1572	C		
1H-3, 37	3.37	IA	1598	C	1611	C
2H-2, 34	11.64	IA	1613	C	1610	C
2H-4, 45	14.75	IA	1609	C	1604	C
2H-6, 34	17.64	IA	1633	C	1624	C
3H-1, 37	19.67	IA	1653	C	1609	C
3H-3, 37	22.67	IA	1656	C	1671	C
3H-5, 37	25.67	IA	1641	C	1594	C
3H-7, 37	28.67	IA	1685	C	1569	C
4H-1, 37	29.17	IA	1640	C	1633	C
4H-3, 37	32.17	IA	1624	C	1634	C
4H-5, 37	35.17	IA			1650	C
5H-1, 37	36.87	IA			1644	C
5H-3, 37	39.87	IA	1665	C	1657	C
5H-5, 37	42.87	IB	1653	C	1659	C
6H-1, 37	45.27	IB	1619	C	1631	C
6H-3, 37	48.27	IB	1649	C	1658	C
6H-4, 127	50.67	IB	1680	C	1669	C
6H-5, 37	51.27	IB	1692	C	1678	C
7H-1, 37	53.17	IB	1630	C	1623	C
7H-3, 120	57.00	IB			1654	C
7H-5, 37	59.17	IB	1584	C		
8H-3, 37	64.37	IB	1612	S		
9H-2, 37	68.87	IC	1683	S		
9H-4, 37	71.87	IC	1574	S		
10H-1, 130	73.80	IC	1511	C		
10H-2, 131	75.31	IC	1668	S		
10H-4, 40	77.40	IC	1683	S		
11H-2, 73	79.83	IC	1797	S		
12H-1, 125	84.45	IC	1795	S		
12H-2, 30	85.00	IC	1726	C		
13H-1, 40	88.20	II	1730	S		
13H-3, 41	91.21	II	1719	C		
14X-1, 77	92.27	II	1724	S		
15X-1, 67	101.67	II	1693	S		
15X-3, 67	104.67	II	1942	S		
134-827B-						
1R-2, 37	112.47	II			1713	C
1R-4, 37	115.47	II	1695	C	1742	C
2R-2, 35	119.45	II	1922	S	1984	S
2R-4, 130	123.40	II	1693	C	1694	C
3R-1, 110	128.30	II	1658	C	1644	C
3R-3, 135	131.55	II	1692	C	1681	C
3R-5, 135	134.55	II	1651	C	1649	C

Table 6 (continued).

Sample (cm)	Depth (mbsf)	Unit	Vertical velocity (m/s)	Wave type[a]	Horizontal velocity (m/s)	Wave type[a]
3R-7, 20	136.40	II	1676	S	1671	C
6R-1, 140	157.60	IIIA	1663	S	1678	S
6R-3, 140	160.60	IIIA	1676	S		
7R-2, 140	168.70	IIIA	1592	S		
7R-3, 137	170.17	IIIA			1710	S
8R-1, 83	176.23	IIIA			2073	S
8R-4, 10	180.00	IIIA			1846	S
9R-1, 43	185.53	IIIA			1785	C
9R-2, 112	187.72	IIIA			1782	C
9R-5, 128	192.38	IIIA			1750	C
10R-1, 76	195.46	IIIA			1962	C
10R-3, 113	198.83	IIIA			1672	C
10R-5, 39	201.09	IIIB			1727	C
11R-1, 37	204.77	IIIB			1913	C
11R-3, 37	207.77	IIIB			1898	C
12R-1, 37	214.37	IIIB			1837	C
12H-1, 43	214.43	IIIB	2539	S		
12R-3, 34	217.34	IIIB			1881	C
13R-1, 44	224.14	IIIC			1831	C
13R-3, 36	227.06	IIIC			1744	C
13R-5, 40	230.10	IIIC			1901	C
13R-6, 104	232.24	IIIC			1657	C
14R-1, 20	233.50	IIIC			1637	C
14R-2, 59	235.39	IIIC			1680	C
14R-3, 12	236.42	IIIC			1777	C
15R-1, 129	244.29	IIIC			1954	C
15R-3, 17	246.17	IIIC			2049	C
15R-5, 25	249.25	IIIC			1763	C
15R-6, 65	251.15	IIIC			1653	C
16R-1, 10	252.70	IV			2080	C
16R-1, 39	252.99	IV			4678	C
17R-CC, 14	262.44	IV	4220	C		
18R-CC, 11	272.11	IV			3409	C
19R-CC, 10	281.80	IV	4233	S		
21R-1, 10	301.10	IV	4697	S		
22R-CC, 15	312.35	IV			4986	C
23R-CC, 0	320.30	IV	4744	S		
24R-CC, 3	329.53	IV	4298	C		
25R-1, 20	339.20	IV	4150	C		
26R-1, 6	345.76	IV	3984	S		
27R-1, 32	355.62	IV	4619	C		
28R-1, 0	365.00	IV	4587	S		
28R-1, 20	365.20	IV			1985	C
30R-1, 32	384.52	IV	1990	C	2072	C
30R-1, 110	385.30	IV			1965	C

[a]C = compressional (*P*-wave) and S = shear (*S*-wave).

distance from the shore is 4000–4500 mbsl. The uplift of Wousi Bank may be reflected in lithologic changes at Site 827, from the sed-lithic conglomerate in Units III and IV to the volcanic silt in Unit II and the fine-grained volcanic turbidites in Unit I, as discussed below.

Today Wousi Bank is separated from Espiritu Santo Island by a channel 200 m deep. This channel intercepts and diverts coarse sediment derived from the island away from the bank. Clasts of volcanic breccia and igneous rocks derived from Espiritu Santo Island in sed-lithic conglomerates of Units III and IV suggest, therefore, that Wousi Bank did not exist in its present configuration when the conglomerates were deposited. Deposition of these conglomerates could have occurred either in basins on the arc slope or in the trench below Site 827 with later accretion to the slope. In either case, conglomerate deposition suggests that there was an uninterrupted slope between Site 827 and Espiritu Santo Island and implies that uplift of Wousi Bank had not yet started at the time of conglomerate deposition.

The timing of the uplift of Wousi Bank, which may be related to collision of the NDR, is poorly constrained by data from Site 827 because of uncertainties in ages of the conglomerates in Units III and IV and because of possible thrust faults within these units. In addition, the stratigraphic relationship of Units III and IV with Units I and II is uncertain because of a possible thrust fault near the top of Subunit IIIA. Nevertheless, the absence of conglomerate in Units I and II suggests that the source of coarse sediment from Espiritu Santo Island may have been cut off by the uplift of Wousi Bank in late Pliocene or middle Pleistocene time. Uplift of Wousi Bank during this time is also suggested by benthic foraminifers, which show a change from lower to mid-bathyal assemblages during the deposition of Subunit IIIA.

The silt in Unit II at Site 827 is interpreted as fine-grained hemipelagic sediment. A change from hemipelagic sedimentation to the deposition of turbidites in Unit I suggests that a basin formed on the flank of Wousi Bank and trapped sediment transported downslope. This basin corresponds to the flat terrace on which Site 827 is located. Paleomagnetic data indicate that the turbidites in the basin are younger than 0.7 Ma, and a nannofossil datum near the base of Unit I suggests that the basin could be as young as 0.25–0.30 Ma (Fig. 29; "Sediment Accumulation Rates" section, this chapter).

Anomalously high concentrations of sulfate and methane in pore fluids suggest that thrust faults in the collision zone may

Table 7. Shear-strength data, Site 827.

Sample (cm)	Depth (mbsf)	Unit	Method[a]	Undrained shear strength (kPa)
134-827A-				
1H-1, 42	0.42	IA	SP	13.5
1H-3, 42	3.42	IA	SP	27.6
1H-5, 42	6.42	IA	SP	39.8
2H-2, 131	12.61	IA	SP	45.8
2H-4, 135	15.65	IA	SP	52.1
2H-6, 134	18.64	IA	SP	59.9
3H-1, 43	19.73	IA	SP	50.1
3H-3, 42	22.72	IA	SP	49.2
3H-5, 42	25.72	IA	SP	65.8
3H-7, 41	28.71	IA	SP	50.3
4H-1, 41	29.21	IA	SP	42.1
4H-3, 35	32.15	IA	SP	57.7
4H-5, 42	35.22	IA	SP	58.4
5H-1, 35	36.85	IA	SP	40.4
5H-3, 34	39.84	IA	SP	57.7
5H-5, 42	42.92	IB	SP	62.9
6H-1, 42	45.32	IB	TD	35.9
6H-3, 45	48.35	IB	TD	110.9
6H-4, 117	50.57	IB	TD	94.1
6H-5, 43	51.33	IB	TD	112
7H-1, 32	53.12	IB	TD	62.7
7H-3, 43	56.23	IB	TD	66.1
7H-5, 44	59.24	IC	TD	117.6
8H-1, 43	61.43	IC	TD	98.6
8H-3, 33	64.33	IC	TD	107.6
9H-1, 8	67.08	IC	SP	50.6
9H-2, 32	68.82	IC	SP	95.3
9H-4, 32	71.82	IC	SP	123.2
10H-1, 137	73.87	IC	SP	84.3
10H-2, 126	75.26	IC	SP	118
11H-1, 71	78.31	IC	SP	75.5
11H-2, 69	79.79	IC	SP	115.8
12H-1, 33	83.53	IC	SP	61.6
12H-2, 37	85.07	IC	SP	135.6
13H-1, 37	88.17	II	SP	126.1
13H-3, 36	91.16	II	SP	153.2

[a] SP = Wykeham-Farrance spring vane-shear apparatus; TD = ODP motorized miniature vane shear (torvane device).

be connected at depth to the décollement. Although the anomalous values occur in undeformed turbiditic sands, they are characteristic of fluids in subduction zones and may indicate upward migration of exotic fluids from the décollement, possibly along thrust faults.

REFERENCES

Akimoto, K., 1990. Distribution of Recent benthic foraminiferal faunas in the Pacific off Southwest Japan and around Hachijojima Island. *Sci. Rep. Tohuku Univ., Ser. 2,* 60:139–223.

Akimoto, K., Tanaka, T., Hattori, M., and Hotta, H., 1991. Recent foraminiferal assemblages around *Calyptogena* colony off Hatsushima Island, Sagami Bay, central Japan. *Tech. Rep. Symp. Deep-Sea Res. Using Submersible Shinka 2000 System.* Jpn. Mar. Sci. Tech. Center.

Carney, J. N., and Macfarlane, A., 1982. Geological evidence bearing on the Miocene to Recent structural evolution of the New Hebrides Arc. *Tectonophysics,* 87:147–175.

Champion, D. E., Lamphere M. A., and Kuntz, M. A., 1988. Evidence for a new geomagnetic reversal from lava flows in Idaho: discussion of short polarity reversals in the Brunhes and Late Matuyama Polarity Chrons. *J. Geophys. Res.,* 93:11667–11681.

Collot, J.-Y., and Fisher, M. A., 1991. The collision zone between the north d'Entrecasteaux ridge and the New Hebrides island arc. Part 1: Seabeam morphology and shallow structure. *J. Geophys. Res.,* 96:4457–4478.

Collot, J.-Y., Pelletier, B., Boulin, J., Daniel, J., Eissen, J.-P., Fisher, M. A., Greene, H. G., Lallemand, S., and Monzier, M., 1989. Premiers résultats des plongées de la campagne SUBPSO1 dans la zone de collision des rides d'Entrecasteaux et de l'arc des Nouvelles Hébrides. *C. R. Acad. Sci. Ser. 2,* 309:1947–1954.

Fisher, M. A., Collot, J.-Y., and Geist, E. L., 1991. The collision zone between the North d'Entrecasteaux Ridge and the New Hebrides Island Arc. Part 2: structure from multichannel seismic data. *J. Geophys. Res.,* 96:4479–4495.

Fisher, M. A., Collot, J.-Y., and Smith, G. L., 1986. Possible causes for structural variation where the New Hebrides island arc and the D'Entrecasteaux zone collide. *Geology,* 14:951–954.

Gieskes, J. M., Blanc, G., Vrolijk, P., Elderfield, H., and Barnes, R., 1990a. Interstitial water chemistry—major constituents. *In* Moore, J. C., Mascle, A., et al., *Proc. ODP, Sci. Results,* 110: College Station, TX (Ocean Drilling Program), 155–178.

Gieskes, J. M., Vrolijk, P., and Blanc, G., 1990b. Hydrogeochemistry of the Northern Barbados Accretionary Complex Transect: ODP Leg 110. *J. Geophys. Res.,* 95:8809–8818.

Graf, D. L., 1982. Chemical osmosis, reverse chemical osmosis, and the origin of subsurface brines. *Geochim. Cosmochim. Acta,* 46:1431–1448.

Han, M. W., and Suess, E., 1989. Subduction induced pore fluid venting and the formation of authigenic carbonates along the Cascadia continental margin: implications for the global Ca-cycle. *Palaeogeogr., Palaeoclimatol., Palaeoecol.,* 71:97–118.

Hanshaw, B. B., and Coplen, T. B., 1973. Ultrafiltration by a compacted clay membrane. II: sodium ion exclusion at various ionic strengths. *Geochim. Cosmochim. Acta,* 37:2311–2327.

Hills, S. J., and Thierstein, H. R., 1989. Plio-Pleistocene calcareous plankton biochronology. *Mar. Micropaleontol.,* 14:67–96.

Jouannic, C., Taylor, F. W., Bloom, A. L., and Bernat, M., 1980. Late Quaternary uplift history from emerged reef terraces on Santo and Malekula Islands, central New Hebrides island arc. *Tech. Bull.—U. N. Econ. Soc. Comm. Asia Pac., Comm. Co-ord. Jt. Prospect Miner. Resour. South Pac. Offshore Areas,* 3:91–108.

Kastner, M., Elderfield, H., Martin, J. B., Suess, E., Kvenvolden, K. A., and Garrison, R. E., 1990. Diagenesis and interstitial-water chemistry at the Peruvian continental margin—major constituents and strontium isotopes. *In* Suess, E., von Huene, R., et al., *Proc. ODP, Sci. Results,* 112: College Station, TX (Ocean Drilling Program), 413–440.

Kennett, J. P., and Srinivasan, M. S., 1983. *Neogene Planktonic Foraminifera: A Phylogenetic Atlas:* Stroudsburg, PA (Hutchinson Ross).

Kharaka, Y. K., and Berry, F. A., 1973. Simultaneous flow of water and solute through geological membranes. I: experimental investigations. *Geochim. Cosmochim. Acta,* 37:2577–2603.

Lovell, M. A., 1985. Thermal conductivity and permeability assessment by measurement in marine sediments. *Geophysics,* 36:266–284.

Maillet, P. M., Monzier, M., Selo, M., and Storzer, D., 1983. The d'Entrecasteaux zone (southwest Pacific): a petrological and geochronological reappraisal. *Mar. Geol.,* 53:179–197.

Mallick, D.I.J., and Greenbaum, D., 1977. *Geology of Southern Santo.* Regional Rept.—New Hebrides Geol. Surv.

Martin, J. B., Kastner, M., and Elderfield, H., in press. Lithium: sources in pore fluids of Peru slope sediments and implications for oceanic fluxes. *Mar. Geol.*

McDuff, R. E., 1981. Major cation gradients in DSDP interstitial waters: the role of diffusive exchange between seawater and upper ocean crust. *Geochim. Cosmochim. Acta,* 45:1705–1713.

McDuff, R. E., and Gieskes, J. M., 1976. Calcium and magnesium profiles in DSDP interstitial waters: diffusion or reaction? *Earth Planet. Sci. Lett.,* 33:1–10.

Mottl, M. J., in press. Pore waters from serpentinite seamounts in the Mariana and Izu-Bonin forearcs, ODP Leg 125: evidence for volatiles from the subducting slab. *In* Fryer, P., Pearce, J. A., et al., *Proc. ODP, Sci. Results,* 125: College Station, TX (Ocean Drilling Program).

Okada, H., and Bukry, D., 1980. Supplementary modification and introduction of code numbers to the low-latitude coccolith biostratigraphic zonation (Bukry, 1973; 1975). *Mar. Micropaleontol.,* 5:321–325.

Ritger, S., Carson, B., and Suess, E., 1987. Methane-derived authigenic carbonates formed by subduction-induced pore water expul-

sion along the Oregon/Washington margin. *Geol. Soc. Am. Bull.*, 48:147–156.

Taira, A., Hill, I., Firth, J. V., et al., 1991. *Proc. ODP, Init. Repts.*, 131: College Station, TX (Ocean Drilling Program).

Taylor, F. W., Isacks, B. L., Jouannic, C., Bloom, A. L., and Dubois, J., 1980. Coseismic and Quaternary vertical tectonic movements, Santo and Malekula Islands, New Hebrides island arc. *J. Geophys. Res.*, 85:5367–5381.

Taylor, F. W., Jouannic, C., and Bloom, A. L., 1985. Quaternary uplift of the Torres Islands, northern New Hebrides frontal arc: comparison with Santo and Malekula Islands, central New Hebrides frontal arc. *J. Geol.*, 93:419–438.

Taylor, F. W., Frohich, C., Lecolle, J., and Strecker, M., 1987. Analysis of partially emerged corals and reef terraces in the central Vanuatu arc: comparison of contemporary coseismic and nonseismic with Quaternary vertical movements. *J. Geophys. Res.*, 92:4905–4933.

Yokota, T., Kinoshita, H., and Uyeda, S., 1980. New DSDP (Deep Sea Drilling Project) downhole temperature probe utilizing IC RAM (Memory) elements. *Tokyo Daigaku Jishin Kenkyusho Iho*, 55:75–88.

Ms 134A-107

NOTE: All core description forms ("barrel sheets") and core photographs have been printed on coated paper and bound as Section 4, near the back of this volume, beginning on page 581.

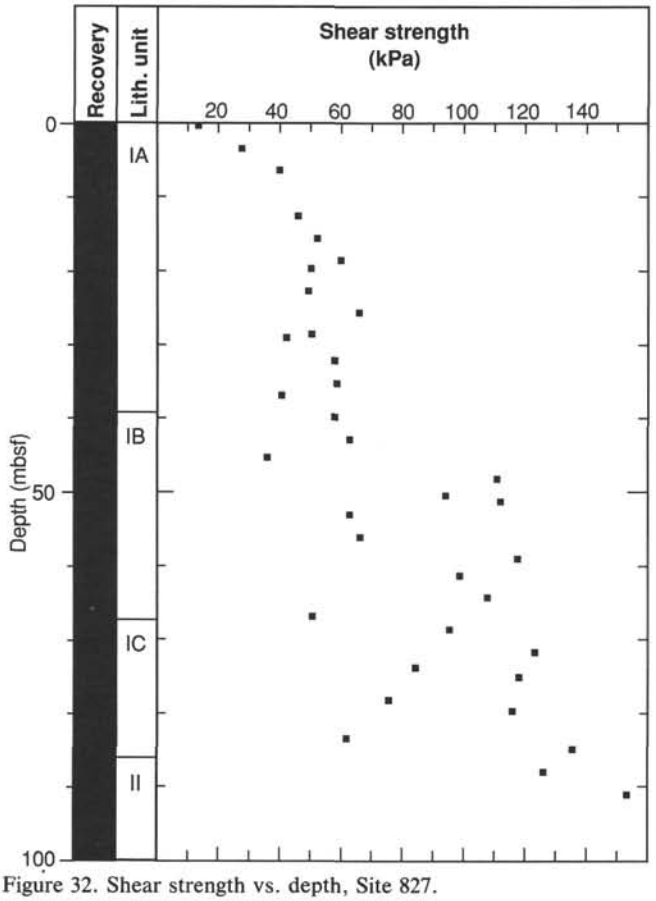

Figure 32. Shear strength vs. depth, Site 827.

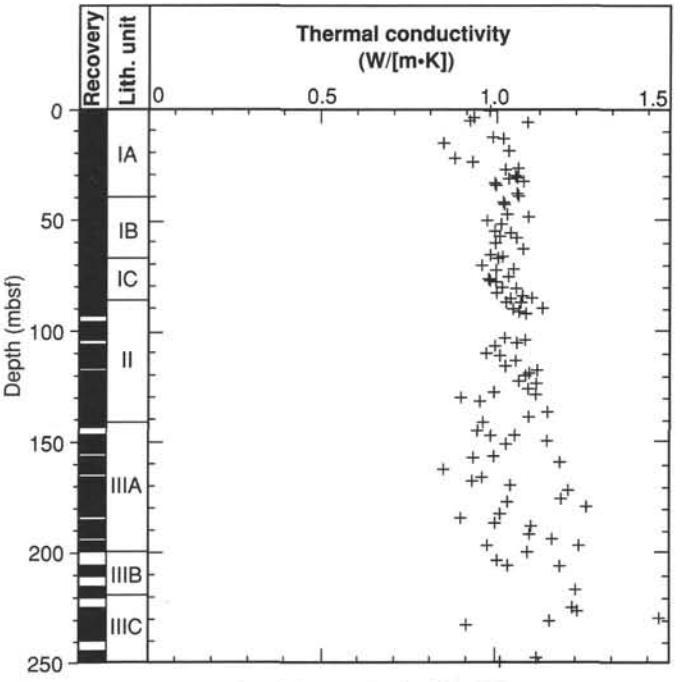

Figure 33. Thermal conductivity vs. depth, Site 827.

Table 8. Thermal conductivity data, Site 827.

Sample (cm)	Depth (mbsf)	Unit	Value (W[m · K])
134-827A-			
1H-1, 75	0.75	IA	0.9868
1H-2, 75	2.25	IA	0.9402
1H-3, 75	3.75	IA	0.9262
1H-4, 75	5.25	IA	1.0937
2H-2, 75	12.05	IA	0.9936
2H-3, 75	13.55	IA	1.0298
2H-4, 75	15.05	IA	0.8537
2H-6, 75	18.05	IA	1.0425
3H-2, 75	21.55	IA	0.8845
3H-3, 75	23.05	IA	0.9387
3H-5, 75	26.05	IA	1.0698
3H-6, 75	27.55	IA	1.0340
4H-2, 75	31.05	IA	1.0584
4H-3, 75	32.55	IA	1.0616
4H-2, 75	31.05	IA	1.0437
4H-3, 75	32.55	IA	1.0788
4H-4, 75	34.05	IA	0.9993
4H-5, 75	35.55	IA	1.0064
5H-2, 75	38.75	IA	1.0656
5H-3, 75	40.25	IB	1.0680
5H-4, 75	41.75	IB	1.0301
5H-4, 75	41.75	IB	1.0301
5H-5, 75	43.25	IB	1.0285
6H-2, 75	47.15	IB	1.0378
6H-3, 75	48.65	IB	1.0969
6H-4, 75	50.15	IB	0.9786
6H-5, 75	51.65	IB	1.0246
7H-2, 75	55.05	IB	1.0017
7H-3, 75	56.55	IB	1.0490
7H-4, 75	58.05	IB	1.0148
7H-5, 75	59.55	IB	1.0679
8H-1, 75	61.75	IB	1.0031
8H-2, 75	63.25	IB	1.0807
8H-3, 75	64.75	IB	1.0038
8H-4, 75	66.25	IB	0.9851
9H-1, 75	67.75	IC	1.0231
9H-2, 75	69.25	IC	1.0130
9H-3, 75	70.75	IC	0.9642
9H-4, 30	71.80	IC	1.0578
10H-1, 75	73.25	IC	1.0120
10H-2, 75	74.75	IC	1.0433
10H-3, 75	76.25	IC	0.9834
10H-4, 30	77.30	IC	0.9851
11H-1, 75	78.35	IC	1.0166
11H-2, 75	79.85	IC	1.0675
11H-3, 75	81.35	IC	1.0414
11H-4, 50	82.60	IC	1.0094
12H-1, 71	83.91	IC	1.0849
12H-2, 71	85.41	IC	1.1086
12H-3, 71	86.91	II	1.0462
12H-CC, 22	87.71	II	1.0322
13H-1, 75	88.55	II	1.0788
13H-2, 75	90.05	II	1.1432
13H-3, 20	91.00	II	1.0643
13H-CC, 10	91.38	II	1.0787
14X-1, 50	92.00	II	1.0898
15X-2, 73	103.23	II	1.0292

Table 8 (continued).

Sample (cm)	Depth (mbsf)	Unit	Value (W[m · K])
15X-3, 82	104.82	II	1.0845
15X-4, 72	106.22	II	1.0653
15X-5, 51	107.51	II	1.0052
134-827B-			
1R-1, 75	111.35	II	0.9770
1R-1, 75	111.35	II	1.0049
1R-2, 75	112.85	II	1.0157
1R-3, 75	114.35	II	1.0617
1R-4, 75	115.85	II	1.0355
2R-1, 75	118.35	II	1.1232
2R-2, 75	119.85	II	1.0978
2R-3, 75	121.35	II	1.0909
2R-4, 75	122.85	II	1.0709
2R-5, 75	124.35	II	1.1211
2R-6, 33	125.43	II	1.0960
3R-1, 80	128.00	II	0.9912
3R-2, 80	129.50	II	1.1209
3R-3, 80	131.00	II	0.9012
3R-4, 80	132.50	II	0.9573
4R-1, 75	137.65	II	1.1550
4R-2, 75	139.15	II	1.0994
4R-4, 75	142.15	IIIA	0.9638
4R-6, 75	145.15	IIIA	0.9508
5R-1, 70	147.20	IIIA	1.0589
5R-2, 70	148.70	IIIA	0.9907
5R-3, 75	150.25	IIIA	1.1570
5R-4, 75	151.75	IIIA	1.0369
6R-1, 75	156.95	IIIA	0.9956
6R-2, 75	158.45	IIIA	0.9384
6R-3, 75	159.95	IIIA	1.1922
6R-5, 75	162.95	IIIA	0.8527
7R-1, 85	166.65	IIIA	0.9615
7R-2, 81	168.11	IIIA	0.9366
7R-3, 79	169.59	IIIA	1.0458
7R-5, 77	172.57	IIIA	1.2140
8R-1, 73	176.13	IIIA	1.1959
8R-2, 63	177.53	IIIA	1.0386
8R-4, 63	180.53	IIIA	1.2651
8R-6, 63	183.53	IIIA	1.0143
9R-1, 77	185.87	IIIA	0.9023
9R-2, 81	187.41	IIIA	1.0001
9R-3, 87	188.97	IIIA	1.10798
9R-5, 77	191.87	IIIA	1.1052
10R-1, 75	195.45	IIIA	1.1688
10R-2, 75	196.95	IIIA	0.9790
10R-3, 75	198.45	IIIA	1.2483
10R-5, 75	201.45	IIIB	1.0958
11R-1, 60	205.00	IIIB	1.0025
11R-2, 71	206.61	IIIB	1.0421
11R-3, 44	207.84	IIIB	1.1916
13R-2, 75	225.95	IIIC	1.2290
13R-3, 78	227.48	IIIC	1.2390
13R-5, 70	230.40	IIIC	1.4773
13R-6, 84	232.04	IIIC	1.1614
12R-3, 75	217.75	IIIC	1.2366
14R-1, 37	233.67	IIIC	0.9175
15R-4, 70	248.20	IIIC	1.1216
15R-5, 75	249.75	IIIC	1.0183

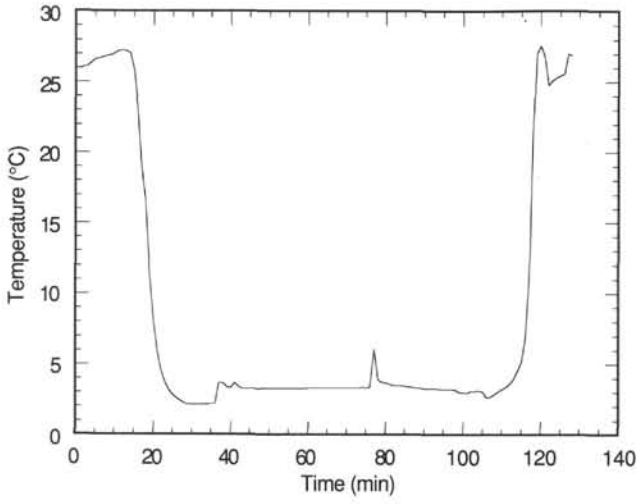

Figure 34. Temperature vs. time for water sampler temperature probe (WSTP) run 4H in Hole 827A at a depth of 28.8 mbsf.

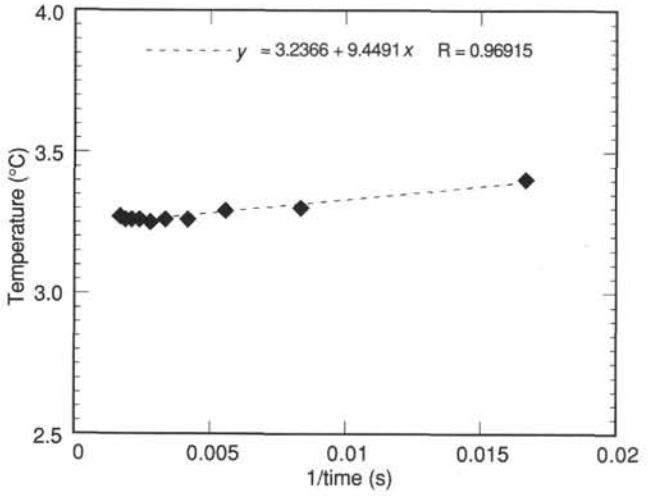

Figure 35. Reduction to equilibrium temperature for water sampler temperature probe (WSTP) run 4H in Hole 827A. The temperature value at 1/time = 0 is the equilibrium value.

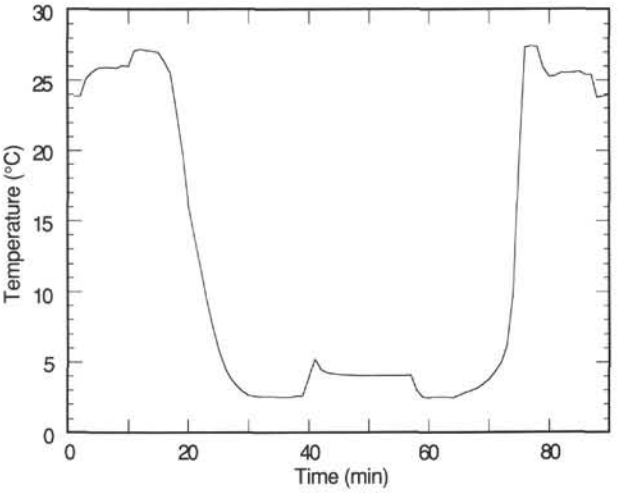

Figure 36. Temperature vs. time for WSTP run 8H in Hole 827A at a depth of 61.0 mbsf.

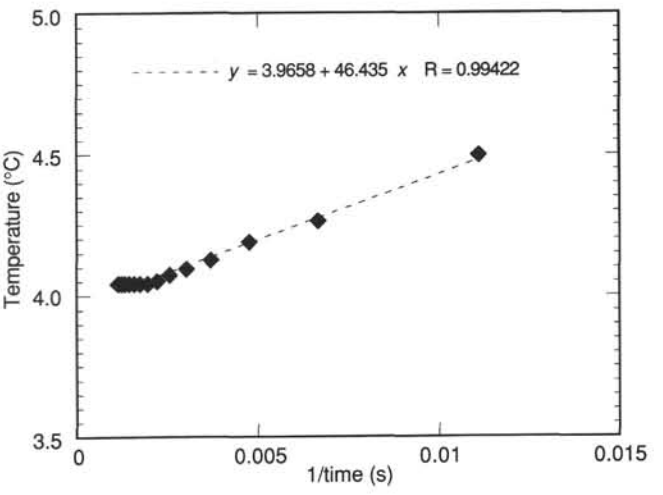

Figure 37. Reduction to equilibrium temperature for WSTP run 8H in Hole 827A.

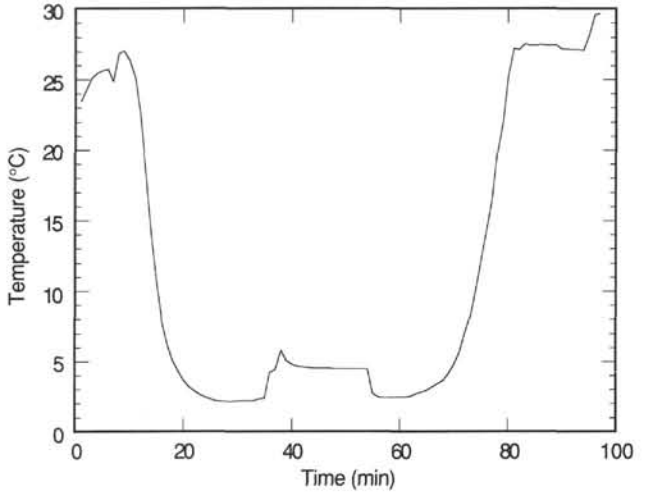

Figure 38. Temperature vs. time for WSTP run 11H in Hole 827A at a depth of 77.6 mbsf.

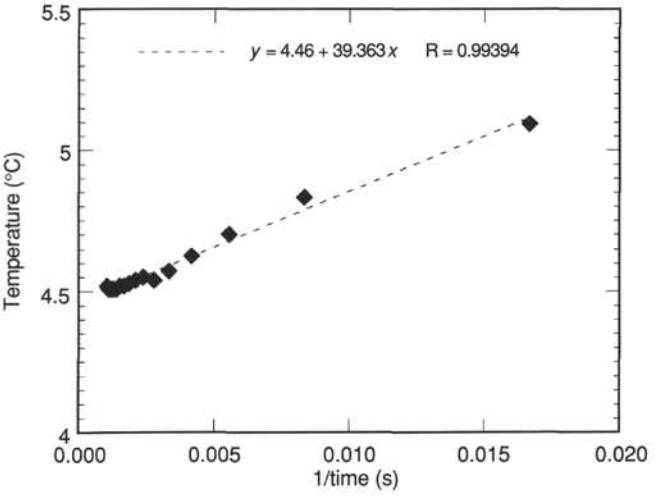

Figure 39. Reduction to equilibrium temperature for WSTP run 11H in Hole 827A.

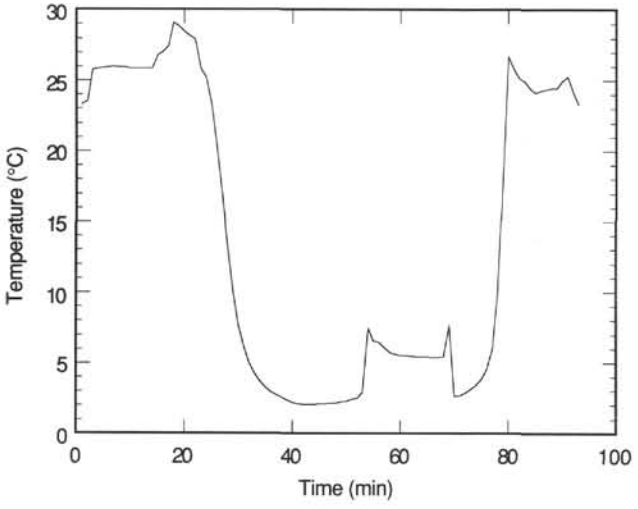

Figure 40. Temperature vs. time for WSTP run 1R in Hole 827B at a depth of 110.0 mbsf.

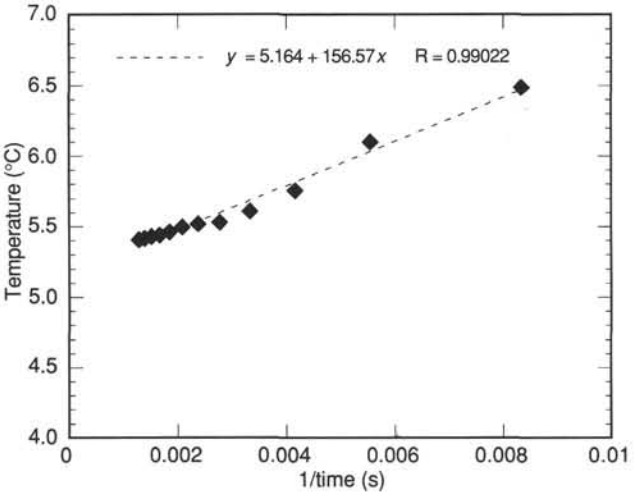

Figure 41. Reduction to equilibrium temperature for WSTP run 1R in Hole 827B.

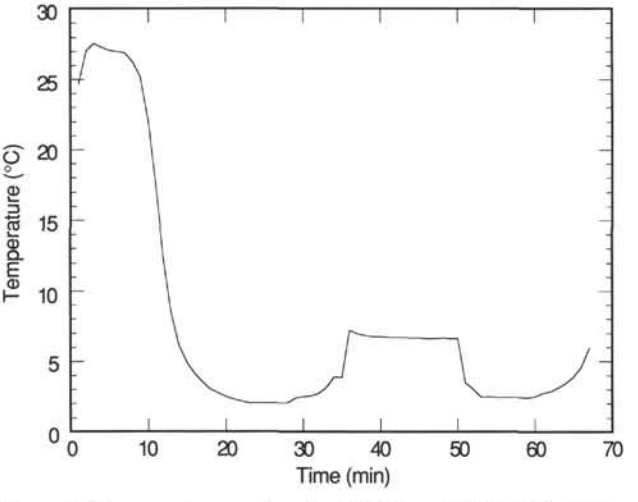

Figure 42. Temperature vs. time for WSTP run 10R in Hole 827B at a depth of 194.7 mbsf.

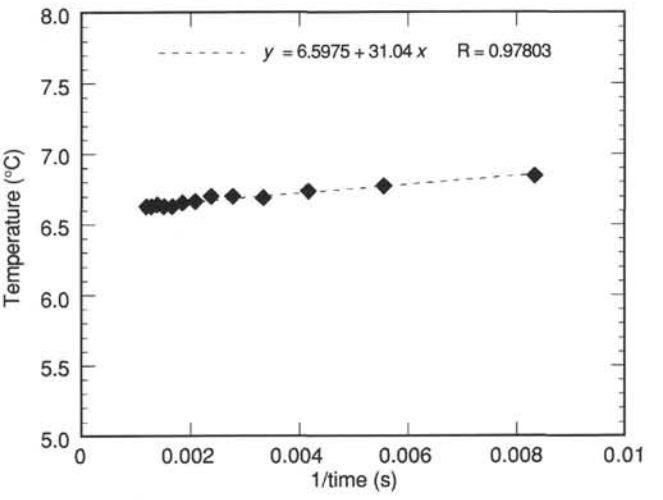

Figure 43. Reduction to equilibrium temperature for WSTP run 10R in Hole 827B.

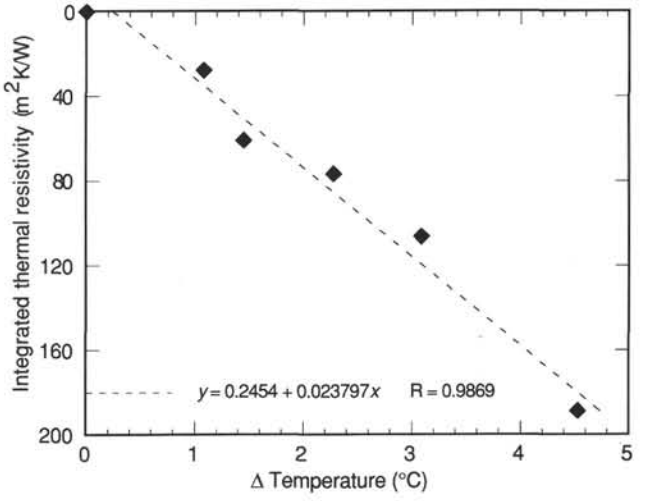

Figure 44. Delta temperature (relative to mud-line values) vs. the depth integral of thermal resistivity for Site 827. The slope of the linear regression line is the conductive heat flow.

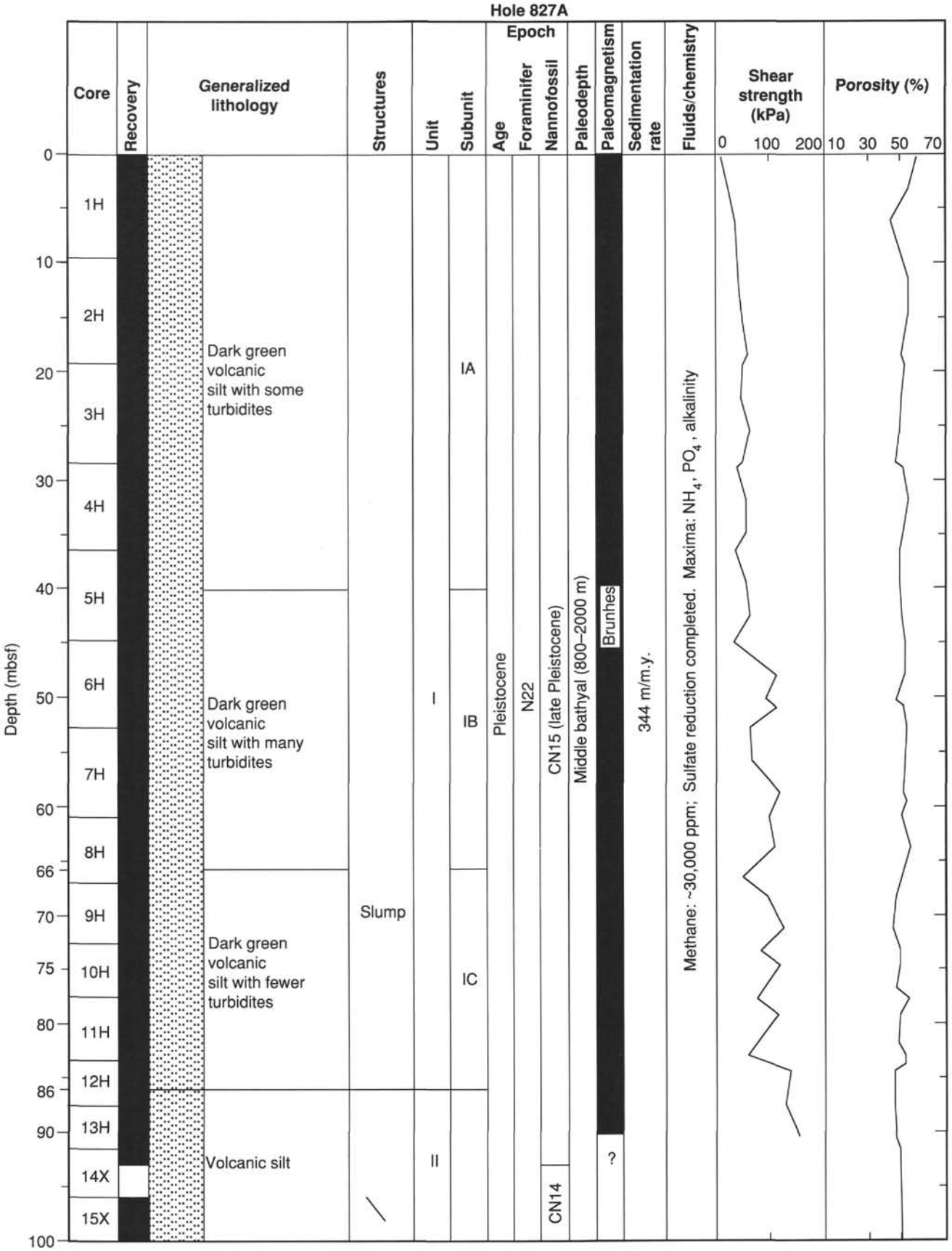

Figure 45. Generalized summary of Holes 827A and 827B. If no data or annotations appear in a particular column, refer to the appropriate section of this chapter for details.

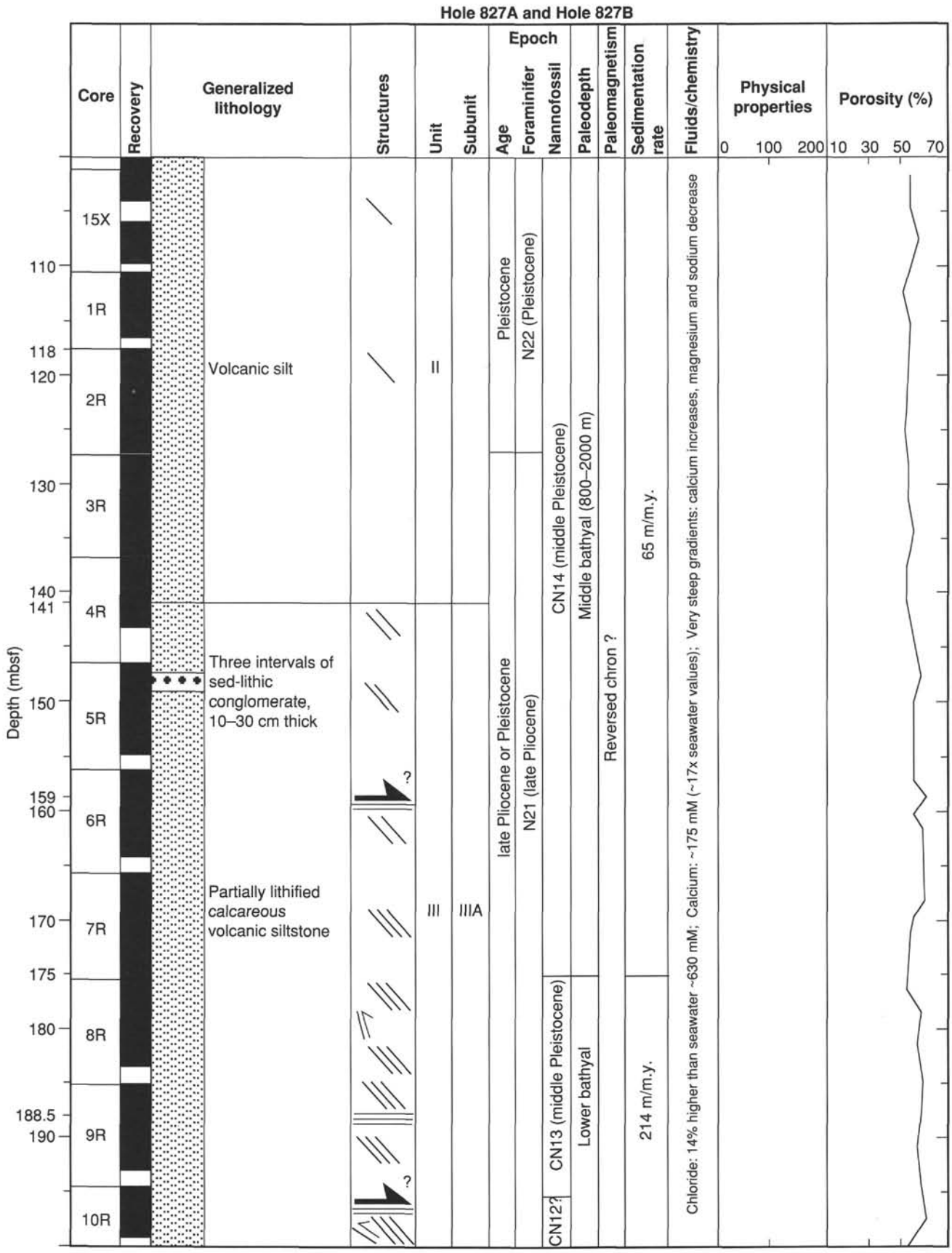

Figure 45 (continued).

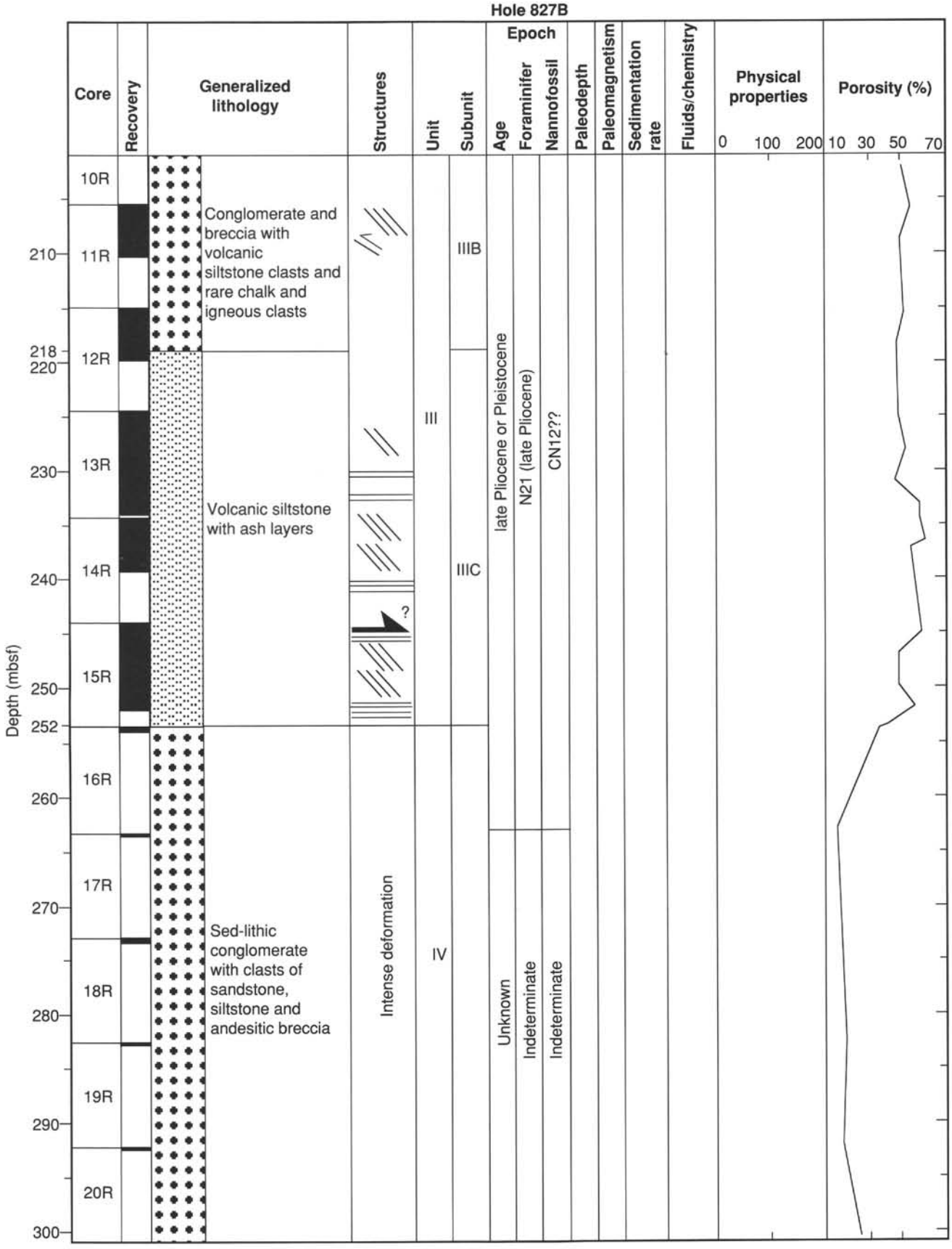

Figure 45 (continued).

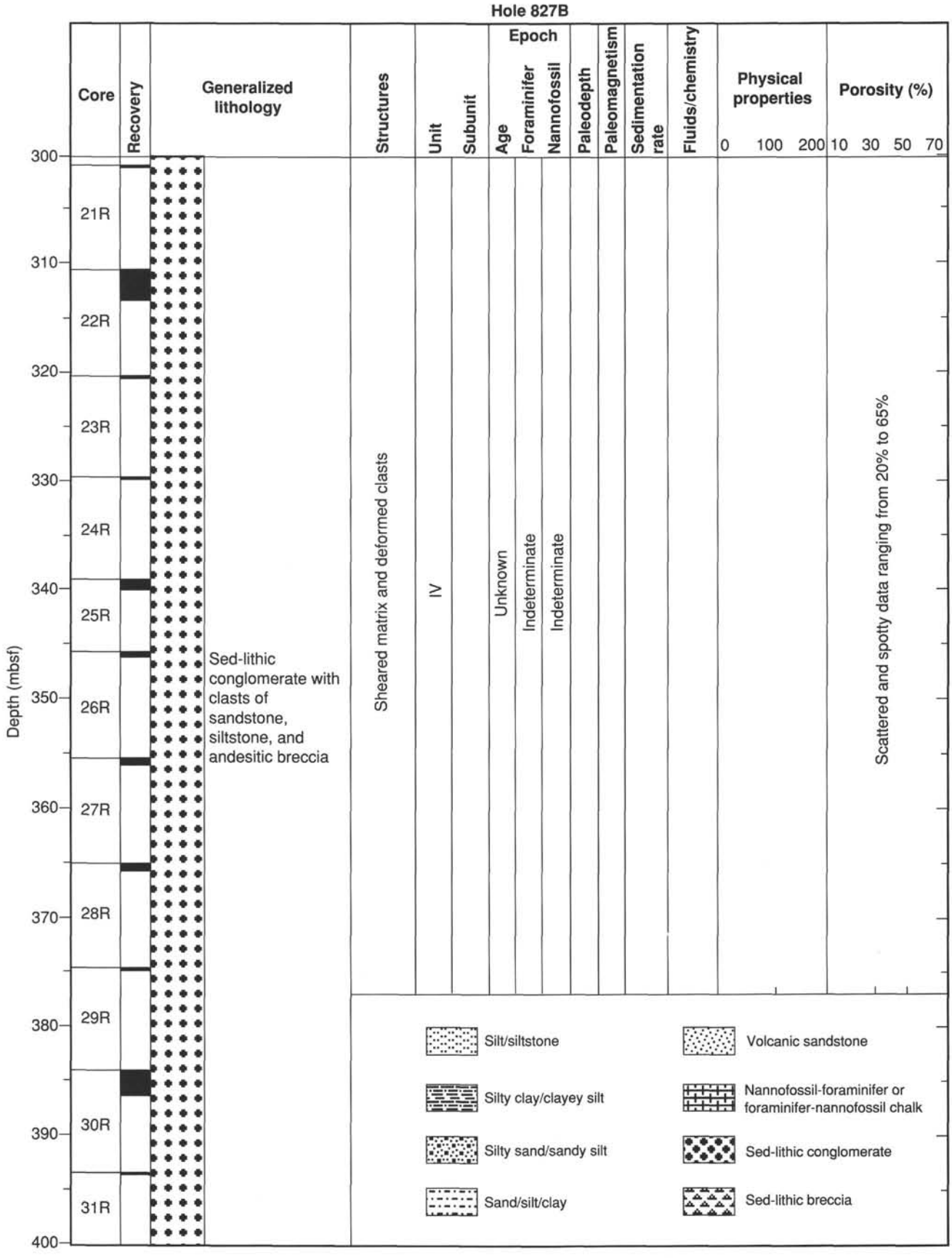

Figure 45 (continued).